

University of Alberta

Functionalization and Characterization of Metal Oxide Coatings of Stainless Steel and Silica Nanoparticles

by

Anne Margaret Slaney

A thesis submitted to the Faculty of Graduate Studies and Research
in partial fulfillment of the requirements for the degree of

Doctor of Philosophy

Department of Chemistry

©Anne Margaret Slaney

Spring 2013

Edmonton, Alberta

Permission is hereby granted to the University of Alberta Libraries to reproduce single copies of this thesis and to lend or sell such copies for private, scholarly or scientific research purposes only. Where the thesis is converted to, or otherwise made available in digital form, the University of Alberta will advise potential users of the thesis of these terms.

The author reserves all other publication and other rights in association with the copyright in the thesis and, except as herein before provided, neither the thesis nor any substantial portion thereof may be printed or otherwise reproduced in any material form whatsoever without the author's prior written permission.

ABSTRACT

The development of tolerogens, fabricated devices eliciting tolerance toward incompatible donor ABO antigens in implant patients, is the ultimate goal of this project. This would permit ABO incompatible organ transplants, increase the donor pool for patients, increase efficiency in the use of available organs, reduce waitlist times and reduce mortality rates of patients. Stainless steel stents and silica nanoparticles were chosen as platforms for the stationary and circulating tolerogens.

Stainless steel was coated with silica by solgel dip-coating, electrodeposition, and atomic layer deposition (ALD). The coatings were evaluated by CV, EIS, SEM, AFM, VASE, FTIR, XPS, and AES. Of the silica films, those deposited by ALD provided superior insulating, conformal, and thin coatings. These silica ALD films outperformed even titania ALD films upon stressing. Silica ALD films were subsequently functionalized with mixtures of silane derivatives of poly(ethylene glycol) (PEG), to prevent nonspecific protein binding, and monosaccharides (MS) or trisaccharide and tetrasaccharide (TS) antigens. Functionalizations were characterized by FTIR, XPS and UV-Vis following enzyme-linked lectin assays (ELLAs) or enzyme-linked immunosorbent assays (ELISAs). Effective functionalization allowing biological availability and activity even after incubation in blood plasma was confirmed. Microarray microscope slides were

similarly developed with all ABO antigen subtypes, characterized by ToF-SIMS and ELISA, and proved useful in detecting antibodies in human blood samples.

Silica nanoparticles, including fluorescent and magnetic varieties, in a range of sizes were prepared by sol-gel synthesis. The nanoparticles were evaluated by SEM, DLS, zeta potential measurements, fluorescence imaging, flow cytometry, two-photon excitation fluorescence correlation spectroscopy and TEM. Different dye incorporation methods were used for effective detection of NPs, and additional silica layers improved fluorophore characteristics. Functionalization of the nanoparticles with PEG and MS or TS were determined successful using three different methods as characterized by FTIR, XPS and ELLA or ELISA and UV-Vis or flow cytometry. The most cost-effective method involved functionalizing nanoparticles with amine, which was optimized using an assay. The amine-terminated nanoparticles were used to tether a PEG linker molecule for covalent binding of PnP derivatives of MSs and TSs.

ACKNOWLEDGEMENTS

It now is unbelievable to me that I have come to this point, a point that would have been impossible had it not been for the amazing people in my life. Many thanks need be expressed to the following people:

To Dr. Jillian Buriak, you have been everything in a supervisor that I could ask for, and more. From inspiration to understanding, you seem to know just what I need before I realize it. You continue to amaze me from your knowledge of literature to the names of the constellations. You've been a role model, a mentor, a teacher, and an ally.

To my colleagues – you rock! Vince, thanks for tag-teaming this project with me so much! Sometimes it was hard to remember who started an experiment and who finished it. Peter, thanks for all the trouble-shooting with me, the fun and the friendship. Ken, thanks for the fun, the expertise and keeping me company and sane in the cleanroom. Your perspective challenged the way I think. Brian, thanks for helping me to get started on this project. Dave – from experimental design to a sounding board, you're an amazing person. And the oh-so-many laughs – thanks for them all! B-ri, thanks for the friendship, being a sounding board and all the fun! Jenn, thanks for the girl talk, the workouts and the laughs. Sean, thanks for the fun, the laughs and the insight into thesis writing – it makes more sense now.

To Mike – my lobster, my rock, my love, my husband, my best friend. You've seen me at my worst, and still support me every step of the way. When I'm about to lose it, you can still make me smile (even if it's a crazy smile sometimes). Every day is a little better with you in it. Thanks for EVERYTHING!

To my family, thanks for everything. Mom, you were always happy to do whatever you can whenever you can. From hemming pants to bringing me hot chocolate at 2 AM so that I could keep studying, I couldn't have gotten here

without you. Dad, your point of view has challenged my decisions or how I feel about a decision countless times. You've challenged me to become the person I am today. Jane, thanks for listening even when I don't make any sense. Sometimes, you're the only one who really understands. Uncle Boyce and Aunt Daisy, Pat and Shirley, and Patrick and Alice, thanks for caring how things are going and the encouragement. Bernice, thanks for the kind words, they go a long way.

Last but not least, to my friends, thanks for sticking by my side. Joel and Tiara (and Ridley too), thanks for always being there. Your support through tough times makes them a little easier and you've become family. Tiff, the walks, the talks, the workouts, the hanging out and the laughs – thanks. Your way of looking at things is honest and refreshing. Aruna, Keith and Lorraine, thanks for the walks, the talks and the laughs. You've gotten me through some pretty bad days.

TABLE OF CONTENTS

Chapter 1 - Introduction	1
References	16
Chapter 2 – Coating of Stainless Steel	23
Introduction	23
Results and Discussion	27
Conclusions	45
Experimental	45
Acknowledgements	56
References	56
Chapter 3 – Functionalization of Silica-Coated Stainless Steel	62
Introduction	62
Results and Discussion	66
Conclusions	84
Experimental	85
Acknowledgements	91
References	91
Chapter 4 – Synthesis of Silica Nanoparticles and Microparticles	95
Introduction	95
Results and Discussion	98
Conclusions	111
Experimental	112
Acknowledgements	116
References	117

Chapter 5 – Functionalization of Silica Nanoparticles and Microparticles	122
Introduction	122
Results and Discussion	125
Conclusions	139
Experimental	140
Acknowledgements	144
References	144
Chapter 6 - Conclusions	149
Coating of Stainless Steel	153
Functionalization of Silica-Coated Stainless Steel	154
Synthesis of Silica Nanoparticles and Microparticles	156
Functionalization of Silica Nanoparticles and Microparticles	157
Future Work	158
References	159

LIST OF TABLES

Chapter 1

Table 1.1	Compatible and incompatible blood types for organ recipients	1
Table 1.2	Compatible and incompatible blood types for organ donors	2
Table 1.3	ABO blood type antibodies produced and ABO blood type compatibility for organ transplant	3

Chapter 2

Table 2.1	Infrared stretching frequencies found in stainless steel 316L coated with silica	29
Table 2.2	Electroactive area, film thicknesses, and percent metals of silica-coated stainless steel samples	33
Table 2.3	Tabulated values of equivalent circuit model values	55

Chapter 3

Table 3.1	Silane concentration used to functionalize stainless steel	73
-----------	--	----

LIST OF FIGURES

Chapter 1

Figure 1.1	Antibody levels detected in newborn O blood type pigs	5
Figure 1.2	Depiction of the six A type antigen subtypes	6
Figure 1.3	Functionalization of silica nanoparticles	9
Figure 1.4	Silane functionalization of silica-coated stainless steel	11
Figure 1.5	Sol-gel reactions	11
Figure 1.6	Tolerogen project flowchart	13

Chapter 2

Figure 2.1	SEM image of a tilted stainless steel stent	23
Figure 2.2	Coating of stainless steel	25
Figure 2.3	Depiction of thin film formation by atomic layer deposition	26
Figure 2.4	Deposition methods used to compare silica thin film coatings on 316L stainless steel	28
Figure 2.5	Infrared spectra of uncoated and silica-coated stainless steel samples	29
Figure 2.6	Experimental setup for electroactive area evaluation by cyclic voltammetry	30
Figure 2.7	Representation of cyclic voltammetry characterization of coatings on stainless steel	30
Figure 2.8	Electrochemical evaluation of representative silica-coated stainless steel samples	32
Figure 2.9	SEM image of a 316L stainless steel coupon with a TEOS electrodeposited silica coating	34
Figure 2.10	AFM height images of silica-coated stainless steel samples	35
Figure 2.11	Elemental composition of silica-coated stainless steel samples in atomic percent	37

Figure 2.12	Plot of the dielectric thickness measured by VASE for a selection of silica thin films deposited by ALD	38
Figure 2.13	High resolution XPS of Si, O, and Cr peaks from a clean stainless steel coupon	39
Figure 2.14	SEM image and AES spectra of an untreated 316L stainless steel stent	40
Figure 2.15	SEM image and AES spectra of a silica-coated 316L stainless steel stent	41
Figure 2.16	Three point bending of metal oxide-coated stainless steel coupons	42
Figure 2.17	Representative cyclic voltammograms of metal oxide-coated stainless steel	44
Figure 2.18	Equivalent circuit used to model EIS data	54
 Chapter 3		
Figure 3.1	Schematic of tissue and biomimetic surfaces	63
Figure 3.2	Immobilization of carbohydrates on solid substrates	64
Figure 3.3	Silane functionalization of stainless steel with desired molecules	65
Figure 3.4	Schematic of stainless steel coating and functionalization	66
Figure 3.5	The silane derivatives of trisaccharide, tetrasaccharide and PEG used to functionalize stainless steel	67
Figure 3.6	Schematic of reaction to produce GlcNAc silane and subsequent reaction with stainless steel	68
Figure 3.7	Transmission FTIR of a series of GlcNAc and PEG functionalized porous silicon surfaces	70
Figure 3.8	Schematic of reaction to produce Gal silane and subsequent reaction with stainless steel	71
Figure 3.9	Atomic % of N, S and O of 316L stainless steel, and silica coated 316L stainless steel reacted with mixtures of GlcNAc or Gal and PEG silanes	72

Figure 3.10	The detection of monosaccharides using an enzyme-linked lectin assay (ELLA)	74
Figure 3.11	Wheat germ agglutinin (WGA) ELLA specific for GlcNAc	76
Figure 3.12	Peanut agglutinin (PNA) ELLA specific for Gal	77
Figure 3.13	Functionalization of silica-coated stainless steel surface with A type I and PEG silanes	78
Figure 3.14	Detection of N and S concentration of silica-coated stainless steel samples functionalized with mixtures of A antigen and PEG silanes as characterized by XPS	79
Figure 3.15	The ELISA assay used to detect A antigens on stainless steel coated by ALD	80
Figure 3.16	Detection of A antigens by ELISA assay before and after incubation in A or O blood plasma for a month	81
Figure 3.17	ABO antigen carbohydrate conjugation to amine-functionalized microarray slides	83
 Chapter 4		
Figure 4.1	Potential applications of multifunctional nanoparticles depending on their constituent materials	95
Figure 4.2	Stöber synthesis used to synthesize metal oxide nanoparticles such as silica	97
Figure 4.3	SEM images of silica nanoparticles prepared by the Stöber method	99
Figure 4.4	Distribution plot of sizes used to calculate the diameters of silica particles	100
Figure 4.5	SEM image of 10 nm NPs after centrifugation	101
Figure 4.6	NP and MP architectures developed herein	104
Figure 4.7	Fluorescent micrograph and images of fluorescent MPs	106
Figure 4.8	Detection of fluorophores incorporated in a shell of MPs by flow cytometry	107

Figure 4.9	Detection of fluorescence of MPs by flow cytometry with varying amounts of incorporated dye	108
Figure 4.10	Images of 20 nm fluorescent core nanoparticles and TRITC dye under white light and under UV light	109
Figure 4.11	Images of nanoparticle solution injection, and vessel in chicken embryo	109
Figure 4.12	TEM images of the magnetite core nanoparticles	110
Figure 4.13	Removal of magnetic nanoparticles in water upon exposure to a magnetic field	110

Chapter 5

Figure 5.1	Functionalization of nanoparticles with biomolecules	123
Figure 5.2	Synthesis of amine-terminated silica nanoparticles and their subsequent functionalization with biomolecules	124
Figure 5.3	The synthesis of silica NPs functionalized with monosaccharide	126
Figure 5.4	Schematic of silica NP surface functionalization via thiol-ene chemistry and detection of GlcNAc	127
Figure 5.5	Fluorescence microscopy images of FITC labelled agglutinin binding to GlcNAc-functionalized silica NPs	128
Figure 5.6	Fluorescence intensity of fluorescent agglutinin binding to GlcNAc-functionalized silica NPs	129
Figure 5.7	High resolution XPS of C and S peaks for silica NPs functionalized with mixtures of MPTMS and PEGTMS	130
Figure 5.8	Schematic of A type antigen binding to MPs	133
Figure 5.9	Semi-quantitative detection of Fmoc	134
Figure 5.10	The detection of A antigen on MPs using antibodies	135
Figure 5.11	Flow cytometry detection of antibodies bound to A and B antigen	136
Figure 5.12	Flow cytometry results for detection of A type II surface functionalization and fluorescent microparticles	137

Figure 5.13	Flow cytometry results for detection of A type II surface functionalization	138
Figure 5.14	Flow cytometry results of fluorescent anti-PEG antibody	139

LIST OF ABBREVIATIONS

Abbreviation	Meaning
AES	Auger electron spectroscopy
AF	Alexa Fluor®
AFM	atomic force microscopy
ALD	atomic layer deposition
APTMS	aminopropyltrimethoxysilane
AS	alkoxy silane
CV	cyclic voltammetry
DLS	dynamic light scattering
EIS	electrochemical impedance spectroscopy
ELISA	enzyme-linked immunosorbent assay
ELLA	enzyme-linked lectin assay
Et	ethyl
FITC	fluorescein isothiocyanate
Fmoc	fluorenylmethyloxycarbonyl
FTIR	fourier transform infrared spectroscopy
Gal	galactose
GlcNAc	N-Acetylglucosamine or N-acetyl-D-glucosamine
HRP	horseradish peroxidase
IgM	immunoglobulin M
Me	methyl
MP	microparticle
MPTMS	mercaptopropyltrimethoxysilane
MS	monosaccharide
NP	nanoparticle
OPD	<i>o</i> -phenylenediamine
PE	phycoerythrin
PEG	poly(ethylene glycol)

Abbreviation	Meaning
PNA	peanut agglutinin
PnP	<i>p</i> -nitrophenol
SEM	scanning electron microscope
SS	stainless steel
TEM	transmission electron microscope
TEOS	tetraethyl orthosilicate
TPE-FCS	two-photon excitation fluorescence correlation spectroscopy
TRITC	tetramethylrhodamine isothiocyanate
TS	trisaccharide or tetrasaccharide
VASE	variable angle spectroscopic ellipsometry
WGA	wheat germ agglutinin
XPS	x-ray photoelectron spectroscopy

CHAPTER 1 – INTRODUCTION

Organ transplant is a necessity for a number of different ailments. For example, congenital cardiac malformations and cardiomyopathies in infants can be lethal unless the required heart transplant is performed in time. Transplant waiting lists can be quite long, and the donor pool can be quite small depending on the recipient and required organ. Patients who require transplants can be quite ill, and patients often die before appropriate donor organs can be found. Additionally, immunosuppressive drug therapy is necessary following organ transplant. This therapy has undesirable side effects that can become life threatening.(1)

In transplantation, ABO compatibility is another limiting factor in finding suitable donor organs.(2) General guidelines are used in order to ensure the safety of the organ recipient.(2,3) The compatible and incompatible blood types for both recipients and donors are listed in Table 1.1 and Table 1.2.(2) From Table 1.1, it can be seen that AB blood type is the universal recipient – it can receive organs from any blood type. Table 1.2, the universal donor, in contrast is O blood type. Although the method is unknown, the immune system produces antibodies against antigens not presented in the body.

Table 1.1. Compatible and incompatible blood types for organ recipients.

Recipient Blood Types	Compatible Blood Types	Incompatible Blood Types
O	O	A, B, AB
A	O, A	B, AB
B	O, B	A, AB
AB	O, A, B, AB	none

Table 1.2. Compatible and incompatible blood types for organ donors.

Donor Blood Types	Compatible Blood Types	Incompatible Blood Types
O	O, A, B, AB	none
A	A, AB	O, B
B	B, AB	O, A
AB	AB	O, A, B

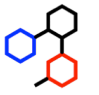
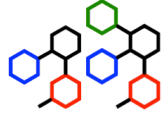
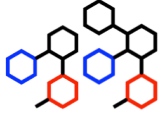
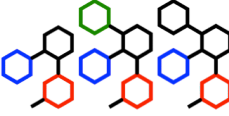
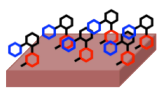
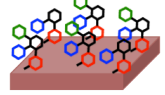
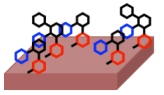
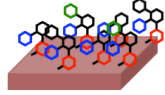



The guidelines outlined in Tables 1.1 and 1.2 limit the already limited quantity of viable donor organs. The life-saving surgery patients require often cannot be performed for this reason. The ABO incompatibility is derived from ABO antigens, polysaccharides presented on the surfaces of many tissues.(4-6) The antigen presented for O blood type is only the H antigen. Other blood types are derived from the addition of A and/or B terminal saccharides to the H antigen by genetically determined enzymes. These antigens are presented in Table 1.3. When the ABO compatibility guidelines are not followed, hyperacute rejection occurs, beginning with binding of antibodies already present in blood plasma.(7,8) This can result in organ rejection and death of the patient.





Even with these risks, attempts to cross the ABO blood barrier have been made in kidney transplantation.(9-13) In the case of kidney transplant, dialysis is still possible in the event of renal failure. Removal of antibodies by splenectomy, plasmapheresis, and B-cell pharmacologic agents are required for successful transplants. However, antibodies can return as a result of B-cell memory.(1)

In the case of heart transplant, there are no alternative therapies in the event of cardiac failure. Most ABO-incompatible heart transplant proved lethal in the past and were performed as a result of errors.(14) For adults, these ABO incompatibility guidelines hold true and should be followed. However, an infant's immune system is not fully developed and does not produce antibodies against carbohydrate antigens, such as ABO blood types, until the immune system matures. A depiction of this is presented in Table 1.3. In infants, maternally derived ABO antibodies are the sole source of blood type antibodies until the

immune system develops which takes months. As such, in the absence of antibody sources such as breast milk, these antibodies will deplete within a couple of weeks.

Table 1.3. ABO blood type antibodies produced in adults and infants and ABO blood type compatibility for organ transplant in infants.

	O blood type	A blood type	B blood type	AB blood type
Antigens Present	 H antigen	 H & A antigens	 H & B antigens	 H, A & B antigens
Tissue Surface				
Antibodies Produced (Adult)	 Anti-A & Anti-B	 Anti-B	 Anti-A	Minimal
Antibodies Produced (Infant)	Minimal	Minimal	Minimal	Minimal
ABO Compatible Tissues (Infant)	All	All	All	All
ABO Incompatible Tissues (Infant)	None	None	None	None

 Galactose  Fucose  N-acetyl glucosamine  N-acetyl galactosamine

From Table 1.3, it can be assumed that this barrier can safely be surmounted in infants, which has been proven.(2) Most ABO incompatible heart transplants were successful, and the unsuccessful cases were unrelated to hyperacute rejection. This expands the donor pool and dramatically decreases the waiting list mortality rate – from 58% to 7%. More than 20 centres worldwide have adopted this protocol with more than 100 patients with a good success rate. This type of organ transplant has also been noted for minimizing the need for chronic systematic pharmacologic immunosuppression, and the derived side effects. This protocol, however, is limited to infants with an immature immune system.

Interestingly, the recipients of ABO incompatible organ recipients do not develop immunity to the donor antigens, called immunologic tolerance.(3) Neonatal tolerance can be induced when foreign antigens are introduced to an immature immune system.(15-18) The immune tolerance is thought to develop in the same way as self-tolerance. The donor-specific tolerance develops spontaneously after ABO incompatible organ transplant. This tolerance persists years after organ transplant. Injection of ABO saccharides has been performed as an attempt to reduce the risk of rejection in ABO incompatible organ transplant. These studies required large amounts of saccharides, which was quite costly, and resulted in offsetting rejection, but did not prevent rejection.(19,20)

The development of a device to induce ABO tolerance in patients, a tolerogen, to extend the window of opportunity for ABO incompatible organ transplant could result in a number of desirable outcomes. An effective tolerogen could result in increasing the potential donor pool for patients, decreasing waitlist times, increasing the survival rate of patients on the organ transplant waitlist, and efficient use of all available organs. This is a large ultimate goal of this work.(21)

For testing of ABO tolerance, a porcine model was chosen because they naturally express A and O blood types and naturally produce anti-A and anti-B antibodies. Upon implantation of tolerogen devices in O blood type piglets, the anti-A and anti-B antibodies can be assessed. The absence of these antibodies would be an effective evaluation of tolerogen utility.

In order for the porcine model to be used effectively, the window of opportunity when minimal ABO antibodies are present and in circulation in the piglets must be identified. Anti-A antigen assays were performed on newborn O blood type pig blood samples by Dr. West and co-workers. The antibody assay was detected by the fluorescent antigen used in the assay and were detected at 405 nm by UV/Vis spectroscopy (depicted in Fig. 1.1). Low optical density (OD) at 405 nm indicates low amounts of detected anti-A antibodies. These results indicate that antibodies

derived maternally are depleted within two weeks. Additionally, it is evident that the piglets begin to produce their own anti-A antibodies after 5 weeks. This indicates that 2-5 weeks is the ideal window for implanting tolerogen devices.

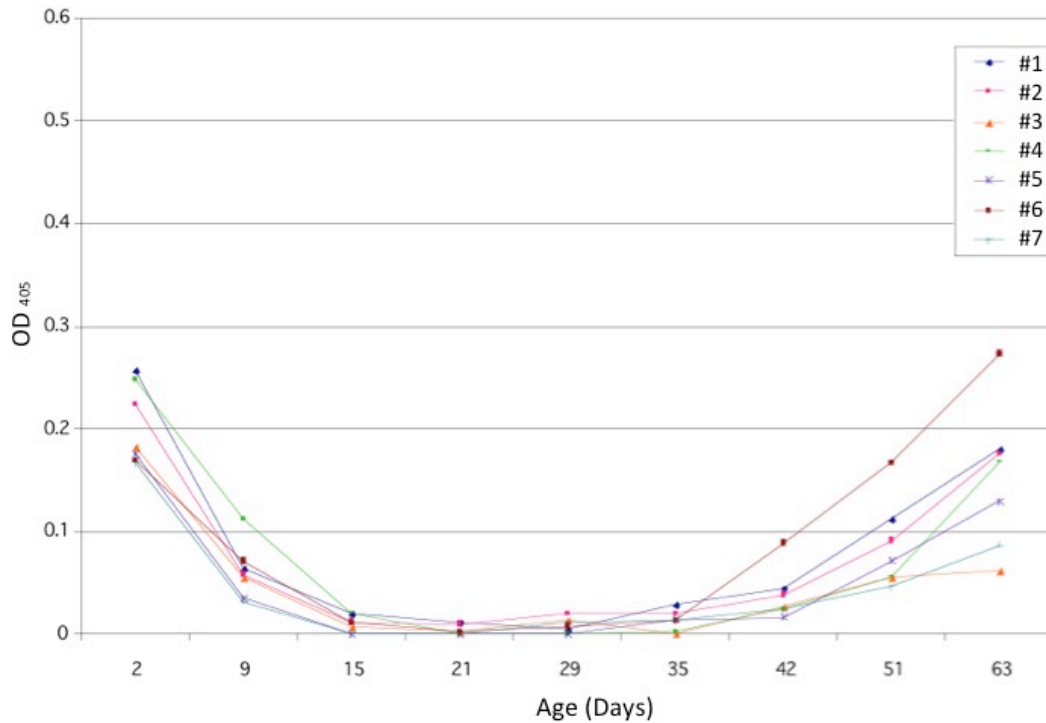


Figure 1.1. Anti-A antibody levels detected in 7 newborn O blood type pigs through optical density at 405 nm.

Additional technologies utilizing functional ABO blood type saccharides have also been developed. Each blood type antigen, (A, B and H) has six subtypes (I-VI).(22) The subtypes are diastereomers of the blood antigen, as demonstrated by the A antigen subtypes depicted in Fig. 1.2. The different subtypes are expressed on different tissues of humans, with the exception of type V antigens.(23-25) These subtypes are an important additional consideration for transfusion and transplant compatibility.(22) These different blood types can be presented in different concentrations, which can make it difficult to detect the blood type and result in mistyping.(26)

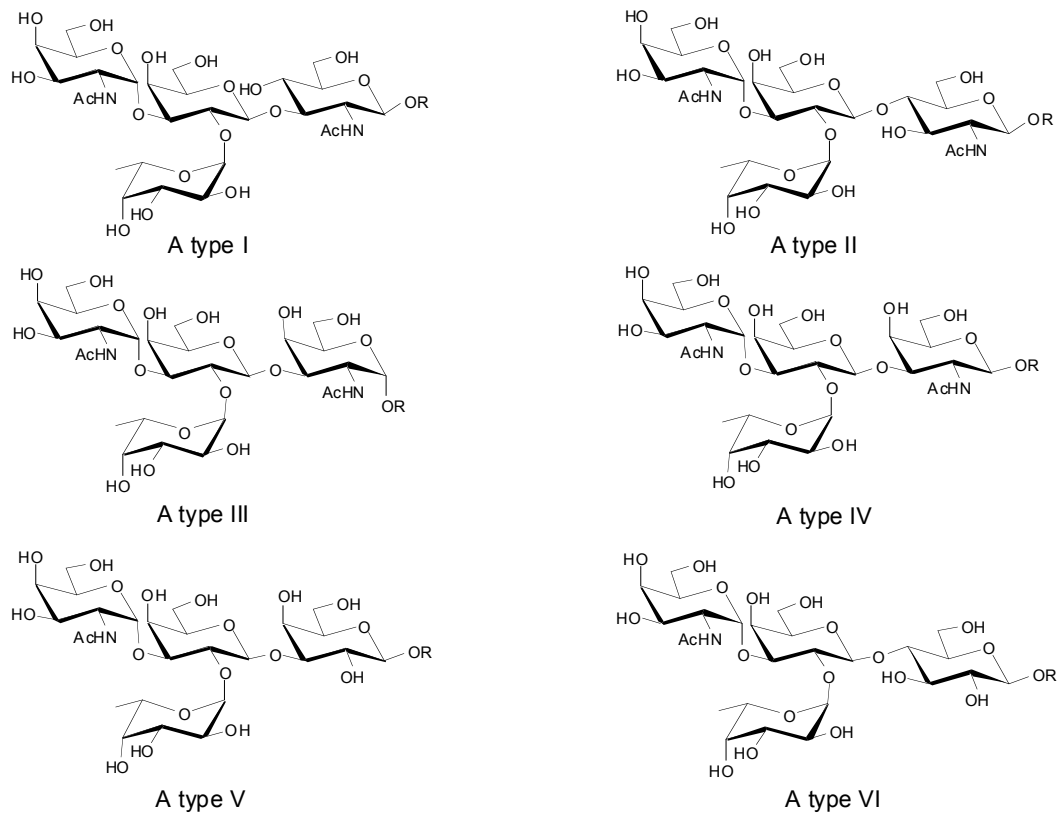


Figure 1.2. Depiction of all six A type antigen subtypes.

The traditional method for ABO compatibility testing between donor and recipient is forward typing (agglutination of the recipient's red blood cells) or reverse typing (agglutination of the recipient's blood serum). From these results, a donor match is determined. In this procedure, subtypes are not determined. It has previously been noted that serious complications can arise from transfusions and transplants between different subtypes of the same blood type.(27,28) Incompatibilities between ABO subtypes often give rise to unexpected results.(29) A trial and error method is typically used for more extensive testing and for better typing between donor and recipient, which can be time consuming and lead to delays in treatment. This delay is unacceptable in an emergency situation, and therefore may result in subtype mismatch.(30) These blood typing methods give no indication of reactivity of a recipient to a particular subtype. Assessing the compatibility by the presence or absence of antibodies toward ABO

subtypes may offer a more effective means of determining subtype compatibility.(1)

Current methods cannot effectively assess ABO subtype compatibility. With better identification of ABO subtype incompatibility, ABO blood barrier may prove easier to overcome than previously thought. This could allow for more effective use of available organs. Quantitative assessments of the ABO subtype antibodies would lead to more extensive assessment of compatibility and better clinical decisions could be made.

A previous attempt has been made to detect ABO antigen subtypes using a bead-based assay.(31) Other multiple ABO subtype glycan microarrays have been used previously.(32,33) However, these methods do not quantitatively assess all subtypes simultaneously. Without the additional subtype information, potential recipients are often declined due to unknown risk of potentially life-saving transplants.

Furthermore, the underlying mechanism of ABO immunologic tolerance is still unknown. Accordingly, it would be ideal to develop a method to study this. Isolation of carbohydrate-specific B cells could allow for this opportunity. This is a difficult task due to the weak interaction between carbohydrates and immunoglobulins, the low frequency of specific B-cells, and non-specific cell adhesion. Developing a flow cytometry assay for detection and characterization of ABO blood type antigen-specific B cells could allow this opportunity.

In preparing tolerogens, long-term exposure of antigens in the blood system is desired. Therefore, nanoparticles and stents were decided as the platforms for attachment of synthetic ABO blood type antigens for introduction into immature immune system to induce tolerance to the antigens. As nanoparticles, the tolerogen could be injected intravenously for circulation. As a stent, the tolerogen could be surgically implanted as a stationary implant. Both of these platforms

must be carefully designed to achieve ideal characteristics for their intended purpose.

The small size of nanoparticles offers a lot of potential in a variety of biomedical applications, including drug delivery.(34-39) Nanoparticles also often have tunable properties that differ from their constituent material in bulk.(38,40,41) The material for the construction of nanoparticles must be carefully selected for its intended purpose.(37,38,42) Silica is a good candidate since it is biocompatible, resists degradation in a biological environment and is easy to functionalize.(43-51) Additionally, silica nanoparticles of a variety of sizes are simple to synthesize and it is also easy to incorporate magnetic or fluorescent properties within them to allow for efficient capture or detection.(38,42,45,46,49,52-55) Varying the size and functionalization of nanoparticles is also simple to change synthetically for silica nanoparticles.(46,48,49) These facile manipulations are ideal since both of these factors can change the effects in biological systems.(38,39,48,56,57)

The nanoparticle functionalization is also very important.(37,39,44,57-61) Covalent attachment of molecules is necessary for stable functionalization of antigen molecules.(45,49,50,52,60,62) Different strategies can be used to bind molecules, including antigen, however, if the nanoparticles were functionalized solely with antigen, they could become susceptible to protein adsorption.(38,41,52,60-63) Protein adsorption would lead to removal from the blood stream.(48,64) This would not be an ideal situation, as numerous injections would be required in order to sustain a sufficient concentration of nanoparticles in the blood stream.

“Stealth” nanoparticles, which have longer half-life in blood circulation, have been established with poly(ethylene glycol) (PEG) functionalization.(37,49,57,63,65-67) By increasing the time these nanoparticles stay in circulation, there is greater opportunity for contact with antigens, and

decrease the need for additional injections.(66) Additionally, by incorporating PEG as well as antigen functionalization onto the silica nanoparticles a biomimetic concentration of antigen may be targeted.

Silane functionalization of silica has proven successful, and as such, this is used for functionalization of both the antigens and PEG.(39,41,45,49,68) This functionalization is depicted in Fig. 1.2.i). For functionalization, either antigen or PEG silane molecules can be used to directly attach them to the silica nanoparticles.(41,49,51) Alternatively, functional silanes can be used to functionalize the nanoparticles as a linker for additional molecules.(38,41,60-62,68) The functionalized nanoparticles can subsequently react with functional groups of the desired molecules for covalent bonding.(38,39,41,60,62,63,68) This type of functionalization is depicted in Fig. 1.2.ii). Mixtures of PEG and antigen in different ratios can be used in this way to optimize antigen presentation and prolong circulation *in vivo*.

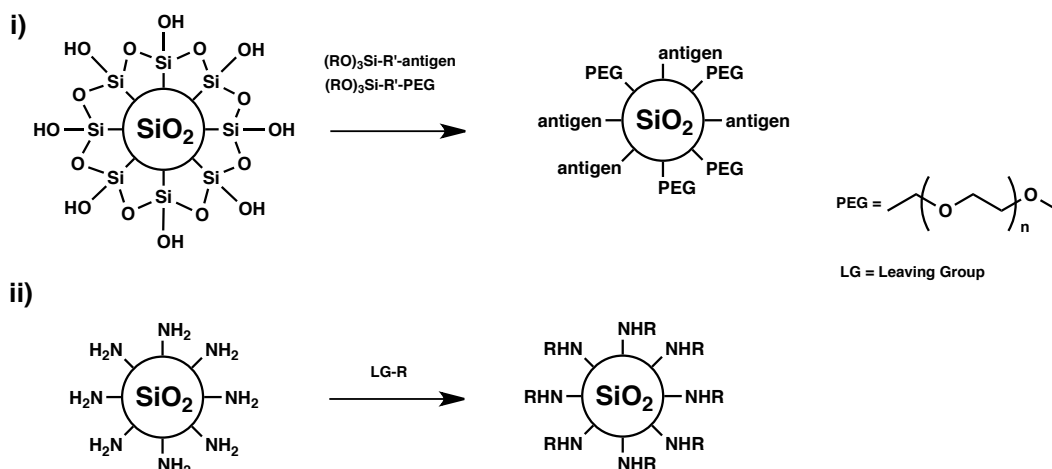


Figure 1.3. i) Functionalization of silica nanoparticles has been successful using silane derivatives of antigen or PEG molecules.(39,41,49) ii) Functionalization using derivatives of desired molecules that are amine reactive with amine-functionalized silica nanoparticles has also been successful.(38,68)

Stainless steel is one of the most widely used materials for stent construction.(69-73) The corrosion resistance, biocompatibility, strength, ease of manipulation and

low cost of stainless steel make it ideal for the fabrication of stents.(69,74-76) However, there is need for coating the stainless steel as ions are released during corrosion *in vivo*.(72,77-80) These ions can be harmful as they consist of carcinogens, allergens and they can cause inflammation.(77-83) Additionally, the metallic stainless steel is susceptible to one-electron reduction of proteins onto the surface, which could cause failure of the tolerogen.(84) Specifically, the one-electron reduction of fibrinogen involves polymerization, which would coat an implant.(85) The formation of a fibrin layer is a normal step in wound healing.(86) This layer promotes the attachment of fibroblast cells, which then allows for the growth of other cells on top of the implant.(86) This cascade would lead to coatings on top of our implants and limit the bioavailability of biomolecules on the surface. As such, it is important for the stainless steel to be coated with an electrically insulating, biocompatible material such as silica, alumina or titania.(84,87-89) The brittle nature of ceramics, however, is a concern upon expansion of the stent *in vivo*.(90-94) Thin films of these ceramic materials have been found to adhere more strongly to stainless steel and tend to be more flexible than thicker films.(89,95)

Silica is an excellent material for functionalization with organic molecules, including biomolecules.(96,97) In coating with ceramic coatings, the surface hydroxyl groups lend to functionalization similar to the silane molecule functionalization used for silica nanoparticles.(96,98-100) Mixed monolayers of both carbohydrate and PEG silanes can be deposited through solution sol-gel deposition.(98,101-103) This functionalization is depicted in Fig. 1.3. A depiction of sol-gel reactions under both acidic and basic conditions can be seen in Fig. 1.4. On these substrates, PEG acts both to prevent nonspecific protein binding and as a spacer molecule for antigens.(104,105)

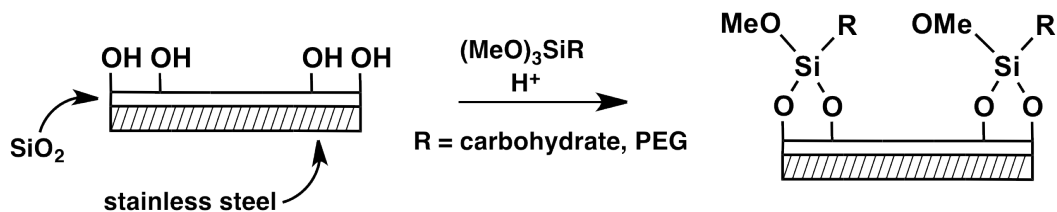


Figure 1.4. Silane derivatives of carbohydrates or PEG molecules can be used to functionalize silica-coated stainless steel through a sol-gel reaction using acid.(96,99,100)

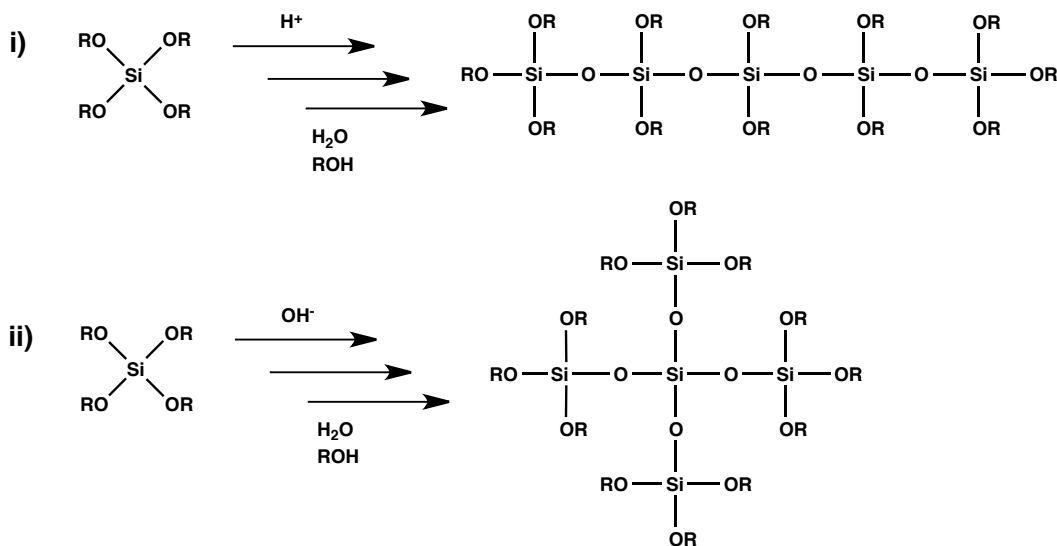


Figure 1.5. Sol-gel reactions consist of condensation and hydrolysis reactions. i) Under acidic conditions, linear chains of siloxanes are formed. ii) Under basic conditions, more highly branched siloxane networks are formed.

Having access to synthetic versions of all 18 ABO blood antigen subtypes allowed for development of an improved method and system for ABO blood type matching, for a more effective matching for organ transplant. This could better determine compatible and incompatible ABO subtypes more effectively and accurately.(1) Additionally, this could offer better monitoring of patients following organ transplant in order to assess for rejection and indicate if intervention is necessary. A simple test of a blood sample could determine compatible ABO subtypes. The development of a ABO antigen glycan microarray device on a substrate would allow for binding of antigen subtype antibodies. Fluorescent antibody detection can then be used for quantitative analysis. By

immobilization of the antigens in an ordered arrangement on a solid surface, simultaneous quantitative detection can be performed. The attachment of the ABO antigens onto silica substrates such as glass slides is an extension of other work outlined here.

Additionally, ABO antigen microarrays of the 18 subtypes were prepared using microscope slide substrates. Similar to other work, antigens can be attached to either silica or amine-terminated surfaces. An array can be fabricated by placement of the subtypes using a commercial microarray printer. Blood serum samples from ABO typed blood can then be assessed for ABO subtype antibodies to better evaluate incompatibilities.

For detection of ABO blood type antigen-specific B cells, antigen-functionalized microparticles were developed. These microparticles included PEG in their design to reduce the non-specific protein binding, and different fluorophores for ease of detection. To identify the rare cell population, microparticles with one of two fluorophores, both functionalized with a single antigen were developed. These two fluorophores allowed for dual staining to allow for increasing specificity for incubation with B cells. With these microparticles as a tool, the isolation of specific B cells could allow for studying this mechanism, and a better understanding of its role in ABO incompatible organ transplantation.

This project is the subject of a collaborative effort between Dr. Lori West, of the University of Alberta Departments of Pediatrics, Surgery and Immunology, Dr. Todd Lowary, of the University of Alberta, Department of Chemistry and the Alberta Ingenuity Centre for Carbohydrate Science, Dr. Jillian Buriak of the University of Alberta, Department of Chemistry and NRC National Institute of Nanotechnology, Dr. Christopher Cairo, of the University of Alberta, Department of Chemistry and the Alberta Ingenuity Centre for Carbohydrate Science and Dr. David Cramb of the University of Calgary, Department of Chemistry. A general overview of the tolerogen project is outlined in Fig. 1.5.

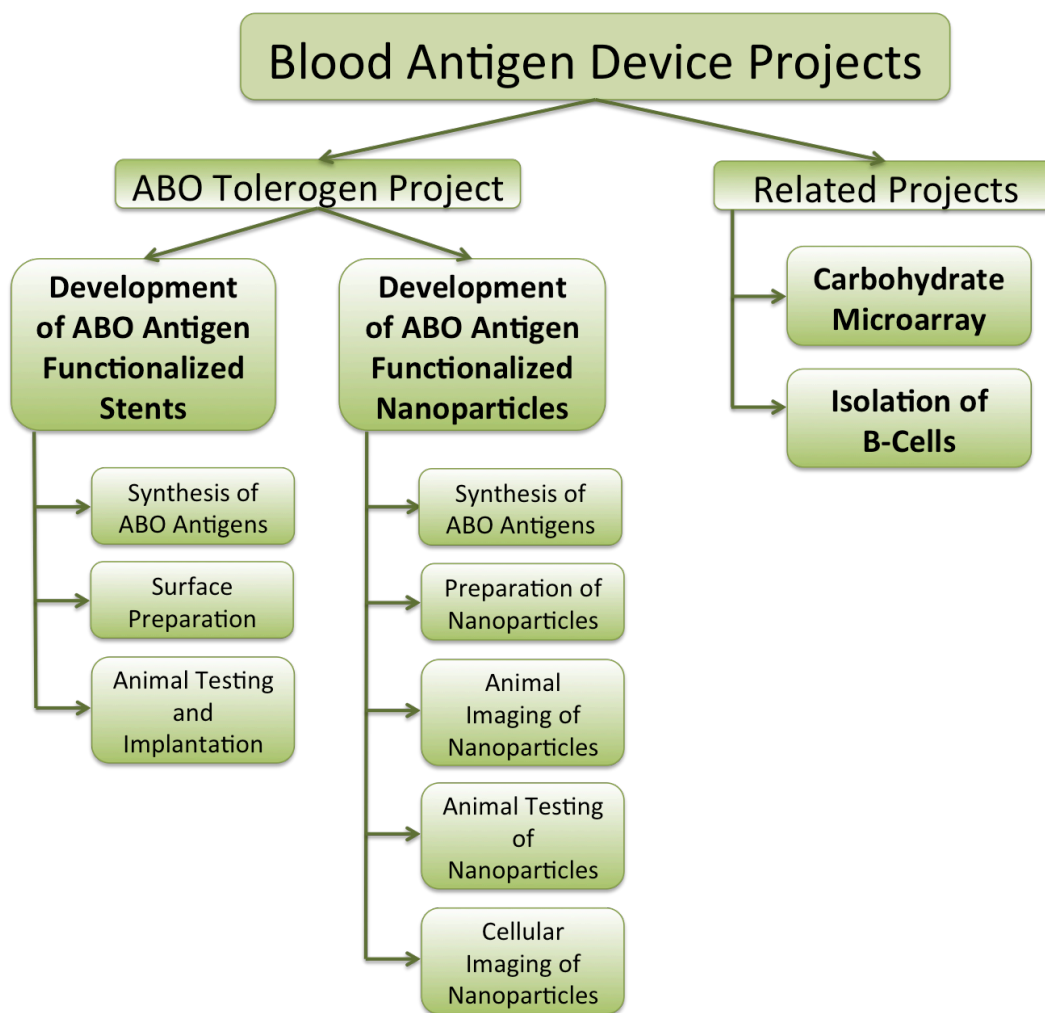


Figure 1.6. Tolerogen project flowchart.

The main projects involve the development of ABO antigen functionalized stents, nanoparticles and microarray slides. The Lowary group is responsible for the synthesis of the antigens and work cooperatively with the Buriak group (the group of which the research herein pertains to) to functionalize substrates. Additionally, the Buriak group is responsible for the surface preparation of stents, the preparation and surface preparation of nanoparticles and microparticles. The West group is responsible for animal testing and implantation and isolation of B-cells. The Cramb group is responsible for imaging of nanoparticles in an animal model, tracking the nanoparticles in tissue to assess their toxicology. The Cairo group is

responsible for studying nanoparticle interactions with cell receptors to optimize tolerogen utility.

Of particular interest for the work explained herein, the Lowary group was involved in the characterization of functionalizations. In particular, the development of enzyme-linked lectin assays (ELLAs) for the monosaccharide model compounds and a fluorenylmethyloxycarbonyl (Fmoc) detection method to assess amine functionalization of nanoparticles and microparticles. The Lowary group also performed the synthesis of all of the carbohydrates used herein. The West group is responsible for the porcine animal testing, the antibody detection and cell detection. The antibody detection was a good indicator for antigen presentation, allowing the assessment of the refinement of functionalizations. The Cramb group is responsible for characterizing the circulation of nanoparticles in chicken embryos. The Cairo group is responsible for the fluorescence imaging of ELLAs.

The Buriak group and the work performed directly by me involved the preparation and functionalization of substrates. Chapter 2 entails the coating of stainless steel. For implant success, the stainless steel requires effective electrical insulation to prevent nonspecific protein binding. Silica coatings were deposited by solgel dip-coating and electrodeposition and atomic layer deposition. Each type of coating was evaluated for the uncoated area, or the electroactive area. The coatings were also evaluated for texture by SEM and AFM. The thickness of the films was evaluated by variable angle spectroscopy ellipsometry. The silica coatings were also evaluated by FTIR, X-ray photoelectron spectroscopy (XPS), and Auger electron spectroscopy. Additionally, silica and titania coatings deposited by atomic layer deposition (ALD) were stressed by three-point bending in an attempt to simulate stress caused to stents upon deployment in an artery. These stressed films were then reevaluated for their electroactive area in order to indicate any changes in the film structure.

In Chapter 3, the functionalization of silica ALD films was evaluated. Monosaccharides were first used as model compounds to assess functionalization before the functionalization with the more valuable tetrasaccharide antigens was explored. Poly(ethylene glycol) was functionalized to prevent nonspecific binding of proteins to preserve the integrity of the implants. Mixtures of monosaccharide and PEG silanes were used to functionalize oxidized porous silicon for evaluation by FTIR. Then silica-coated stainless steel was functionalized with these monosaccharide and PEG silanes for evaluation by XPS and ELLA for detection by UV-Vis. Silica-coated stainless steel were also functionalized with tetrasaccharide and PEG silanes and evaluated by XPS and enzyme-linked immunosorbent assay (ELISA) again for detection by UV-Vis. Additionally the tetrasaccharide and PEG silane-functionalized silica-coated stainless steel were incubated in blood plasma and again evaluated by ELISA as detected by UV-Vis. Additionally, silanes were used to functionalize spots on microscope slides in order to develop microarrays. These microscope slides were characterized by ToF-SIMS and ELISA. They were also used to detect antibodies in human blood plasma in order to identify incompatible blood types based on antibody presence rather than based on the antigen presence.

Chapter 4 deals with the preparation of silica nanoparticles and microparticles by the sol-gel or Stöber synthesis. Different sizes were evaluated by SEM images and dynamic light scattering (DLS). The charge of the particle surface was evaluated by zeta potential measurements. Functionalization of these nanoparticles with simple amine and PEG silanes were evaluated by DLS and zeta potential measurements. Different silica NP architectures were also developed for fluorophore and magnetic NP incorporation. The fluorescence was evaluated fluorescence by fluorescence imaging, flow cytometry and two-photon excitation fluorescence correlation spectroscopy. Additionally, magnetic iron oxide nanoparticles were characterized by transmission electron microscopy.

Finally in Chapter 5, the functionalization of the prepared nanoparticles and microparticles was evaluated. Different methods of functionalizing these surfaces were assessed. Monosaccharide silanes in a mixture with PEG silanes were used for functionalization and were detected using fluorescent lectins, specific for the monosaccharides. Mixtures of simple silanes, specifically thiol and PEG silanes, were detected using XPS. The functionalization of amine silanes on the surface of nanoparticles and microparticles was optimized using a semi-quantitative Fmoc assay as detected by UV-Vis absorbance spectroscopy. Tetrasaccharide ABO blood type antigens were also used to functionalize silica nanoparticles and microparticles with the amine silane as a linker molecule. Dual detection of tetrasaccharide functionalized fluorescent microparticles was performed for both the fluorescent antibody used in the ELISA for specific antigen detection and the fluorescent microparticle, fluorescing at different wavelengths by flow cytometry. Using a PEG antibody, PEG was also detected on functionalized microparticles by flow cytometry. The results are explained within.

ACKNOWLEDGEMENTS

CIHR and NSERC for funding of this project. NSERC and AIF for scholarship funding. The West, Lowary, Buriak, Cramb, Cairo groups for their work on this collaborative project. Dr. Jeyakanthan Mylvaganam for obtaining the antibody data for antibody levels in a porcine model.

REFERENCES

1. Lowary, T.; Cairo, C.; West, L.; Buriak, J.; Jeyakanthan, M.; Slaney, A.; Meloncelli, P. Method and system for ABO compatible blood type matching. US61529082, 2011.
2. West, L.; Pollock-Barziv, S.; Dipchand, A.; Lee, K.; Cardella, C.; Benson, L.; Rebeyka, I.; Coles, J., *New Engl. J. Med.* **2001**, *344* (11), 793-800.
3. Fan, X.; Ang, A.; Pollock-BarZiv, S.; Dipchand, A.; Ruiz, P.; Wilson, G.; Platt, J.; West, L., *Nat. Mater.* **2004**, *10* (11), 1227-1233.
4. Cartron, J.; Colin, Y., *Transfus. Clin. Biol.* **2001**, *8* (3), 163-199.

5. Mollicone, R.; Candelier, J.-J.; Mennesson, B.; Couillin, P.; Venot, A.; Oriol, R., *Carbohydr. Res.* **1992**, *228* (1), 265-276.
6. Oriol, R.; Mollicone, R.; Couillin, P.; Dalix, A.; Candelier, J., *APMIS Suppl.* **1992**, *27* (2), 28-38.
7. Starzl, T.; Ishikawa, M.; Putnam, C.; Porter, K.; Picache, R.; Husberg, B.; Halgrimson, C.; Schroter, G., *Transplant. Proc.* **1974**, *6* (4), 129-139.
8. Stock, P.; Sutherland, D.; Fryd, D.; Ascher, N.; Payne, W.; Simmons, R.; Najarian, J., *Transplant. Proc.* **1987**, *19* (1), 711-712.
9. Slapak, M.; Naik, R.; Lee, H., *Transplantation* **1981**, *31* (1), 4-7.
10. Bennett, A.; Bensinger, W.; Raja, R.; Baquero, A.; McAlack, R., *Transplantation* **1987**, *43* (6), 909-911.
11. Alexandre, G.; Squifflet, J.; Bruyere, M. D.; Latinne, D.; Reding, R.; Gianello, P.; Carlier, M.; Pirson, Y., *Transplant. Proc.* **1987**, *19* (6), 4538-4542.
12. Takahashi, K.; Yagisawa, T.; Sonda, K.; Kawaguchi, H.; Yamaguchi, Y.; Toma, H.; Agishi, T.; Ota, K., *Transplant. Proc.* **1993**, *25* (1), 271-273.
13. Gugenheim, J.; Samuel, D.; Bismuth, H.; Reynes, M., *Lancet* **1990**, *336* (8714), 519-523.
14. Cooper, D., *J. Heart Lung Transpl.* **1990**, *9*, 376-381.
15. Billingham, R.; Brent, L.; Medawar, P., *Nature* **1953**, *172* (4379), 603-606.
16. Owen, R., *Science* **1945**, *102* (2651), 400-401.
17. Streilein, J.; Klein, J., *J. Immunol.* **1977**, *119* (6), 2147-2150.
18. McCarthy, S.; Bach, F., *J. Immunol.* **1983**, *131* (4), 1676-1682.
19. Romano, E.; Neething, F.; Nilsson, K.; Kosanke, S.; Shimizu, A.; Magnusson, S.; Svensson, L.; Samuelsson, B.; Cooper, D., *Xenotransplantation* **1999**, *6* (1), 36-42.
20. Cooper, D.; Y.Ye; Niekrasz, M.; Kehoe, M.; Martin, M.; Neething, F.; Kosanke, S.; DeBault, L.; Worsley, G.; Zuhdi, N.; Oriol, R.; Romano, E., *Transplantation* **1993**, *56* (4), 769-777.
21. West, L.; Lowary, T.; Buriak, J.; Daly, B.; Mylvaganam, J.; Meloncelli, P.; Wright, V.; Cooper, A. Methods and Systems for Inducing Immunologic

Tolerance to Non-Self Antigens. PCT Patent (PCT/CA2009/001814), December, 2009.

22. Meloncelli, P. J.; West, L. J.; Lowary, T. L., *Carbohydr. Res.* **2011**, *346* (12), 1406-1426.
23. Ravn, V.; Dabelsteen, E., *APMIS* **2000**, *108* (1), 1-28.
24. Oriol, R., *Transplant. Proc.* **1987**, *19* (6), 4416-4420.
25. Yamamoto, F., *Immunohematology* **2004**, *20* (1), 3-22.
26. Sapanara, N.; Swami, V.; Besa, E., *LabMedicine* **2004**, *35* (9), 538-541.
27. Contreras, M.; Hazlehurst, G.; Armitage, S., *Br. J. Haematol.* **1983**, *55* (4), 657-663.
28. Gorodzinsky, F.; Stechison, M.; Poon, A.; Arbus, G., *Can. Med. Assoc. J.* **1981**, *125* (8), 871-873.
29. Elsevier Inc.: New York, 2009.
30. Chaudhari, C.; Misra, R.; Nagpal, A., *MJAFI* **2008**, *64* (4), 371-372.
31. Holgersson, J.; Liu, J.; Lindberg, L.; Grufman, P. Blood group antigens of different types for diagnostic and therapeutic applications 7897328, 2011.
32. Bochner, B.; Alvarez, R.; Mehta, P.; Bovin, N.; Blixt, O.; White, J.; Schnaar, R., *J. Biol. Chem.* **2005**, *280* (6), 4307-4312.
33. Blixt, O.; Head, S.; Mondala, T.; Scanlan, C.; Huflejt, M.; Alvarez, R.; Bryan, M.; Fazio, F.; Calarese, D.; Stevens, J.; Razi, N.; Stevens, D.; Skehel, J.; Die, I. v.; Burton, D.; Wilson, I.; Cummings, R.; Bovin, N.; Wong, C.-H.; Paulson, J., *PNAS* **2004**, *101* (49), 17033-17038.
34. Park, J.-H.; Gu, L.; Maltzahn, G. v.; Ruoslahti, E.; Bhatia, S.; Sailor, M., *Nat. Mater.* **2009**, *8* (4), 331-336.
35. Choi, J.; Zheng, Q.; Katz, H.; Guilarte, T., *Environ. Health Perspect.* **2010**, *118* (5), 589-595.
36. Nagao, D.; Yokoyama, M.; Saeki, S.; Kobayashi, Y.; Konno, M., *Colloid Polym. Sci.* **2008**, *286* (8-9), 959-964.
37. Mohanraj, V.; Chen, Y., *Trop. J. Pharm. Res.* **2006**, *5* (1), 561-573.
38. Tan, W.; Wang, K.; He, X.; Zhao, X.; Drake, T.; Wang, L.; Bagwe, R., *Med. Res. Rev.* **2004**, *24* (5), 621-638.

39. Jana, N.; Earhart, C.; Ying, J., *Chem. Mater.* **2007**, *19* (21), 5074-5082.
40. Hoet, P.; Bruske-Hohlfeld, I.; Salata, O., *J. Nanobiotechnology* **2004**, *2* (1), 12-26.
41. Kim, Y.-J.; Ha, S.-W.; Jeon, S.-M.; Yoo, D.; Chun, S.-H.; Sohn, B.-H.; Lee, J.-K., *Langmuir* **2010**, *26* (10), 7555-7560.
42. Gupta, R.; Kumar, A., *Biomed. Mater.* **2008**, *3* (3), 034005.
43. Kumar, R.; Roy, I.; Ohulchanskyy, T.; Vathy, L.; Bergey, E.; Sajjad, M.; Prasad, P., *ACS Nano* **2010**, *4* (2), 699-708.
44. Ha, S.-W.; Camalier, C.; Jr., G. B.; Lee, J.-K., *Chem. Commun.* **2009**, (20), 2881-2883.
45. Burns, A.; Ow, H.; Wiesner, U., *Chem. Soc. Rev.* **2006**, *35* (11), 1028-1042.
46. Ma, D.; Guan, J.; Normandin, F.; Denommee, S.; Enright, G.; Veres, T.; Simard, B., *Chem. Mater.* **2006**, *18* (7), 1920-1927.
47. Insin, N.; Tracy, J.; Lee, H.; Zimmer, J.; Westervelt, R.; Bawendi, M., *ACS Nano* **2008**, *2* (2), 197-202.
48. Burns, A.; Vider, J.; Ow, H.; Herz, E.; Penate-Medina, O.; Baumgart, M.; Larson, S.; Wiesner, U.; Bradbury, M., *Nano Lett.* **2009**, *9* (1), 442-448.
49. He, X.; Nie, H.; Wang, K.; Tan, W.; Wu, X.; Zhang, P., *Anal. Chem.* **2008**, *80* (24), 9597-9603.
50. Wang, Y.; Liu, B., *Langmuir* **2009**, *25* (21), 12787-12793.
51. He, R.; You, X.; Shao, J.; Gao, F.; Pan, B.; Cui, D., *Nanotechnology* **2007**, *18* (31), 315601-315607.
52. Liu, S.; Zhang, H.-L.; Liu, T.-C.; Liu, B.; Cao, Y.-C.; Huang, Z.-L.; Zhao, Y.-D., *J. Biomed. Mater. Res. A* **2007**, *80* (3), 752-757.
53. Corsi, F.; Palma, C. D.; Colombo, M.; Allevi, R.; Nebuloni, M.; Ronchi, S.; Rizzi, G.; Tosoni, A.; Trabucchi, E.; Clementi, E.; Prospero, D., *Small* **2009**, *5* (22), 2555-2564.
54. Lu, C.-W.; Hung, Y.; Hsiao, J.-K.; Yao, M.; Chung, T.-H.; Lin, Y.-S.; Wu, S.-H.; Hsu, S.-C.; Liu, H.-M.; Mou, C.-Y.; Yang, C.-S.; Huang, D.-M.; Chen, Y.-C., *Nano Lett.* **2007**, *7* (1), 149-154.

55. Ow, H.; Larson, D.; Srivastava, M.; Baird, B.; Webb, W.; Wiesner, U., *Nano Lett.* **2005**, *5* (1), 113-117.
56. Warheit, D.; Webb, T.; Colvin, V.; Reed, K.; Sayes, C., *Toxicol. Sci.* **2007**, *95* (1), 270-280.
57. Nel, A.; Madler, L.; Velegol, D.; Xia, T.; Hoek, E.; Somasundaran, P.; Klaessig, F.; Castranova, V.; Thompson, M., *Nat. Mater.* **2009**, *8* (7), 543-557.
58. Senarath-Yapa, M.; Phimphivong, S.; Coym, J.; Wirth, M.; Aspinwall, C.; Saavedra, S., *Langmuir* **2007**, *23* (25), 12624-12633.
59. Zhang, J.; Srivastava, R.; Misra, R., *Langmuir* **2007**, *23* (11), 6342-6351.
60. Gann, J.; Yan, M., *Langmuir* **2008**, *24* (10), 5319-5323.
61. Kim, J.; Cho, J.; Seidler, P.; Kurland, N.; Yadavalli, V., *Langmuir* **2010**, *26* (4), 2599-2608.
62. Nakamura, M.; Shono, M.; Ishimura, K., *Anal. Chem.* **2007**, *79* (17), 6507-6514.
63. Shi, M.; Lu, J.; Shoichet, M., *J. Mater. Chem.* **2009**, *19* (31), 5485-5498.
64. Dobrokvolskaia, M.; McNeil, S., *Nat. Nanotechnol.* **2007**, *2* (8), 469-478.
65. Zillies, J.; Zwioerek, K.; Winter, G.; Coester, C., *Anal. Chem.* **2007**, *79* (12), 4574-4580.
66. Gref, R.; Luck, M.; Quellec, P.; Marchand, M.; Dellacherie, E.; Harnisch, S.; Blunk, T.; Muller, R., *Colloids Surf., B* **2000**, *18* (3-4), 301-313.
67. Lin, Y.-S.; Haynes, C., *Chem. Mater.* **2009**, *21* (17), 3979-3986.
68. Banet, P.; Marcotte, N.; Lerner, D.; Brunel, D., *Langmuir* **2008**, *24* (16), 9030-9037.
69. Lim, I., *MURJ* **2004**, *11*, 33.
70. Tammareddi, S.; Li, Q., *Adv. Mater. Res.* **2010**, *123-125* (Pt. 1, Multi-Functional Materials and Structures III), 315-318.
71. Mani, G.; Feldman, M. D.; Patel, D.; Agrawal, C. M., *Biomaterials* **2007**, *28* (9), 1689-1710.
72. Bayram, C.; Mizrak, A. K.; Akturk, S.; Kursaklioglu, H.; Iyisoy, A.; Ifran, A.; Denkbaz, E. B., *Biomed. Mater.* **2010**, *5* (5), 055007/1-055007/8.

73. Szabadits, P.; Dobranszky, J., *Mater. Sci. Forum* **2010**, 659 (Materials Science, Testing and Informatics V), 337-342.
74. Shahryari, A.; Azari, F.; Vali, H.; Omanovic, S., *Acta Biomater.* **2010**, 6 (2), 695-701.
75. Raman, A.; Gawalt, E. S., *Mater. Sci. Eng., C* **2010**, 30 (8), 1157-1161.
76. Lo, K. H.; Shek, C. H.; Lai, J. K. L., *Mater. Sci. Eng., R* **2009**, 65 (4-6), 39-104.
77. Ekqvist, S.; Svedman, C.; Moeller, H.; Kehler, M.; Pripp, C. M.; Bjoerk, J.; Gruvberger, B.; Holmstroem, E.; Gustavsson, C. G.; Bruze, M., *Br. J. Dermatol.* **2007**, 157 (4), 730-738.
78. Touzin, M.; Chevallier, P.; Lewis, F.; Turgeon, S.; Holvoet, S.; Laroche, G.; Mantovani, D., *Surf. Coat. Technol.* **2008**, 202 (19), 4884-4891.
79. Liu, C. L.; Chu, P. K.; Lin, G. Q.; Qi, M., *Surf. Coat. Technol.* **2006**, 201 (6), 2802-2806.
80. Gallino, E.; Massey, S.; Tatoulian, M.; Mantovani, D., *Surf. Coat. Technol.* **2010**, 205 (7), 2461-2468.
81. Ratner, B. D., *Biomaterials* **2007**, 28 (34), 5144-5147.
82. Okazaki, Y.; Gotoh, E., *Corros. Sci.* **2008**, 50, 3429-3438.
83. Diaz, M.; Sevilla, P.; Galán, A. M.; Escolar, G.; Engel, E.; Gil, F. J., *J. Biomed. Mater. Res. B* **2008**, 87B (2), 555-561.
84. Mikhalovska, L.; Chorna, N.; Lazarenko, O.; Haworth, P.; Sudre, A.; Mikhalovsky, S., *J. Biomed. Mater. Res. B* **2011**, 96B (2), 333-341.
85. Telford, J. N.; Nagy, J. A.; Hatcher, P. A.; Scheraga, H. A., *Proc. Natl. Acad. Sci. USA* **1980**, 77 (5), 2372-2376.
86. Bronzino, J. D., *The Biomedical Engineering Handbook*. 2nd ed.; Springer: 2000; Vol. 1.
87. Wang, D.; Bierwagen, G., *Prog. Org. Coat.* **2009**, 64 (4), 327-338.
88. Gurappa, I., *Surf. Coat. Technol.* **2002**, 161 (1), 70-78.
89. Monsma, D.; Becker, J., *ECS Trans.* **2007**, 11 (7), 39-44.
90. Indolfi, L.; Causa, F.; Netti, P. A., *J. Mater. Sci. - Mater. Med.* **2009**, 20 (7), 1541-1551.

91. Levy, Y.; Mandler, D.; Weinberger, J.; Domb, A. J., *J. Biomed. Mater. Res. B* **2009**, *91B* (1), 441-451.
92. van Ooij, W. J.; Zhu, D.; Stacy, M.; Seth, A.; Mugada, T.; Gandhi, J.; Puomi, P., *Tsinghua Sci. Technol.* **2005**, *10* (6), 639-664.
93. Checmanowski, J.; Szczygiel, B., *Corros. Sci.* **2008**, *50* (12), 3581-3589.
94. Guglielmi, M., *J. Sol-Gel Sci. Technol.* **1997**, *8* (1-3), 443-449.
95. Matero, R.; Ritala, M.; Leskela, M.; Salo, T.; Aromaa, J.; Forsen, O., *J. Phys. IV* **1999**, *09* (PR8), 493-499.
96. Meth, S.; Sukenik, C. N., *Thin Solid Films* **2003**, *425* (1-2), 49-58.
97. Fischer, H.; Wirtz, D.; Weber, M.; Neuss, M.; Niethard, F.; Marx, R., *J. Biomed. Mater. Res.* **2001**, *57* (3), 413-418.
98. Hatano, K.; Yamazaki, T.; Yoshino, K.; Ohyama, N.; Koyama, T.; Matsuoka, K.; Terunuma, D., *Tetrahedron Lett.* **2008**, *49* (39), 5593-5596.
99. Maat, J.; Regeling, R.; Yang, M.; Mullings, M.; Bent, S.; Zuilhof, H., *Langmuir* **2009**, *25* (19), 11592-11597.
100. Anderson, A.; Ashurst, W., *Langmuir* **2009**, *25* (19), 11541-11548.
101. Earhart, C.; Jana, N.; Erathodiyil, N.; Ying, J., *Langmuir* **2008**, *24* (12), 6215-6219.
102. Lim, J. A.; Cho, J. H.; Jang, Y.; Han, J. T.; Cho, K., *Thin Solid Films* **2006**, *515* (4), 2079-2084.
103. Liu, L.; Engelhard, M.; Yan, M., *J. Am. Chem. Soc.* **2006**, *128* (43), 14067-14072.
104. Park, S.; Lee, M.-R.; Shin, I., *Chem. Commun.* **2008**, *44* (37), 4389-4399.
105. Slater, J.; Frey, W., *J. Biomed. Mater. Res. A* **2007**, *87* (1), 176-195.

CHAPTER 2 – COATING OF STAINLESS STEEL

INTRODUCTION

Coronary artery disease is a leading cause of death in North America and around the world.(1-3) The most commonly used treatment for atherosclerosis is angioplasty and stent implantation.(4-8) Stents are mesh tubes that act as a scaffold to keep an artery open and prevent the narrowing of arteries, or restenosis, after being expanded by a balloon.(9-15) An SEM image of a stent can be seen in Fig. 2.1. An estimated 400,000 stents are used in the U.S., and 4 million are used worldwide annually.(1,16) Of the stents approved by the U.S. Food and Drug Administration (FDA), most are stainless steel-based.(9,17-19) Stainless steel is used because it is resistant to corrosion, it is strong, it is easy to manipulate and it is inexpensive.(1,20,21) However, in-stent restenosis frequently occurs, a cascade of biological events ending in the re-narrowing of the artery, which is effectively a failure of the implant.(2,4,6,17,22,23)

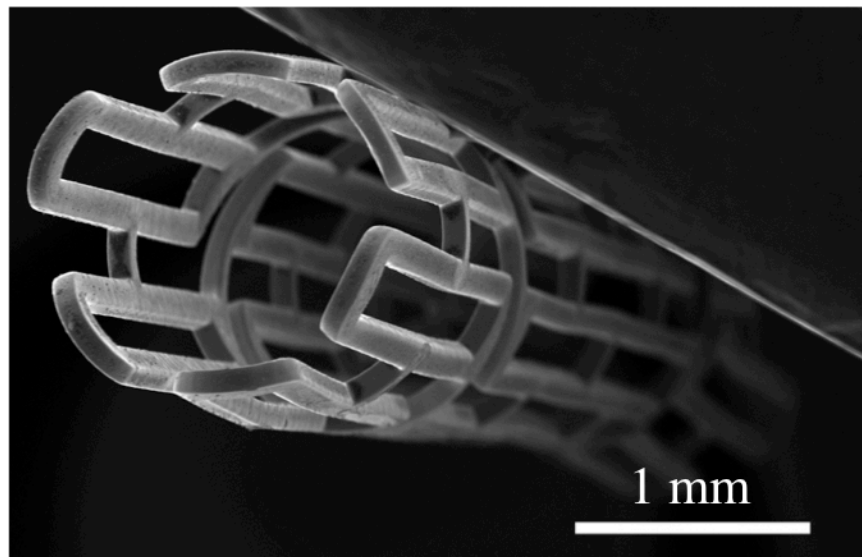


Figure 2.1. SEM image of a tilted stainless steel stent.

One suggested cause of this failure is ions released during the corrosion of stainless steel.(5,15,18,24,25) The release of nickel and chromium ions, known

carcinogens, can cause allergic reactions and inflammation.(5,15,16,24-27) To overcome such issues, drug eluting stents (DESs) have been developed.(12,25,28-30) FDA-approved DESs are generally stainless steel stents with a polymer coating.(31-33) This polymer then releases a drug, which prevents restenosis.(2,14,23,31-38) Although it has been found that these DESs prevent restenosis, late stage thrombosis, the formation of a clot and renarrowing of an artery, can occur. (2,6,17,30,32-34,36,37,39-41)

In light of the issues with DESs, the coating of stainless steel stents, particularly with polymers, has become a growing area of research. One advantage of coating with polymers is that they can be applied in a number of different ways – electropolymerization, spray coating, dip coating, chemical vapour deposition, and even grafting. (40,41) Although polymethacrylates and a variety of fluorinated polymers have proven viable, biocompatible polymers such as polypyrroles and polylactic acids have been of particular interest.(3,12,15,28,29,31,32,34,35,37) PEG coatings have also been studied for their ability to enhance biocompatibility and anti-fouling properties of implants.(14,42-46) However, conformal coatings have been problematic, and some of these coatings have been found to trigger an adverse immune response or degrade over prolonged periods of time.(12,15,29,34,37) Fig. 2.2i depicts this type of polymer coatings that can degrade over time. Bonding of polymer to stainless steel surfaces has shown to enhance the stability of the coating during expansion of the stent and biological tests.(31,32,40) To this end, silanes have shown promise and have provided a method that allows the addition of molecules other than polymers.(43,44,47-49)

Other research has focused on ceramic coatings on stainless steel in part for their ability to protect metals from corrosion, and in part for a means to which desired molecules can be chemically bound.(7,49-52) Sol-gel coatings have shown promise in producing such corrosion resistance on stainless steel.(53,54) Sol-gels are appealing because they involve solution processes that are cheap and easy to

apply a ceramic coating, and they allow deposition onto various geometries.(55,56) Sol-gels are deposited in a variety of methods such as dip coating, spin coating, spray coating, and electrodeposition.(50,57) Sol-gels are also extremely versatile – different materials including titania, silica and alumina films can all be fabricated from sol-gels.(56,58) Controlling certain experimental factors like pH, solvent composition, and molecular precursors can also control the characteristics of the resulting product.(50,55) Of the different coatings, silica is the most common, and dip coating has proven a convenient, effective method in applying a homogeneous silica sol-gel thin film onto stainless steel.(49,57,59) On the other hand, electrodeposited films are uniform, have controllable thickness and improved corrosion resistance.(55,60)

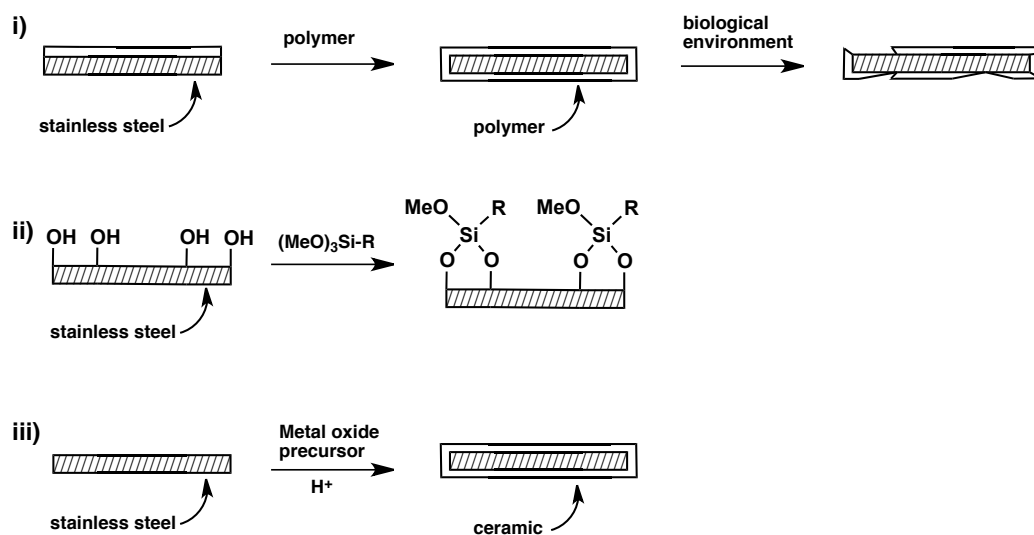


Figure 2.2. i) Polymer coatings on stainless steel tend to degrade over time in biological environments.(12,15) ii) Coatings on stainless steel using silane molecules show improved stability.(48,49) iii) Ceramic coatings deposited on stainless steel using sol-gel reactions have also shown stability in biological environments. (53,54,57,59)

It is important for stainless steel to be electrically isolated to prevent the one-electron reduction of fibrinogen (a cell adhesion protein) onto the surface of the stent, which would render functional stents useless.(39) Specifically, silica, alumina and titania have shown promise due to their biocompatibility and their

insulating properties (or low electron conductivity in the case of titania).(39,50,61,62) Titania coatings have been found to reduce adhesion of fibrinogen and can be used as a platform to bind organic molecules that are stable *in vivo*.(7,39) Silica coatings on stainless steel have proven good surfaces to securely bind organic molecules.(49,63) The adhesion of thinner films rather than thicker ones to stainless steel has been demonstrated for titania.(64) Additionally, atomic layer deposition (ALD) has been proven to produce highly uniform, pinhole-free coatings even as thin layers and over complex geometries, and have improved the stability of self-assembled monolayers.(62,65,66) This technique involves precise control over the dosing of gas precursors into a vacuum chamber. Cycles of different precursor dosing steps and purging steps made possible by ALD offer the opportunity to reproducibly create such conformal, thin films. This stepwise process is outlined in Figure 2.3. However, the brittle nature of ceramic coatings may be an issue – from handling to deployment, the coating could change, and therefore alter the integrity of the coating.(3,41,55,67,68)

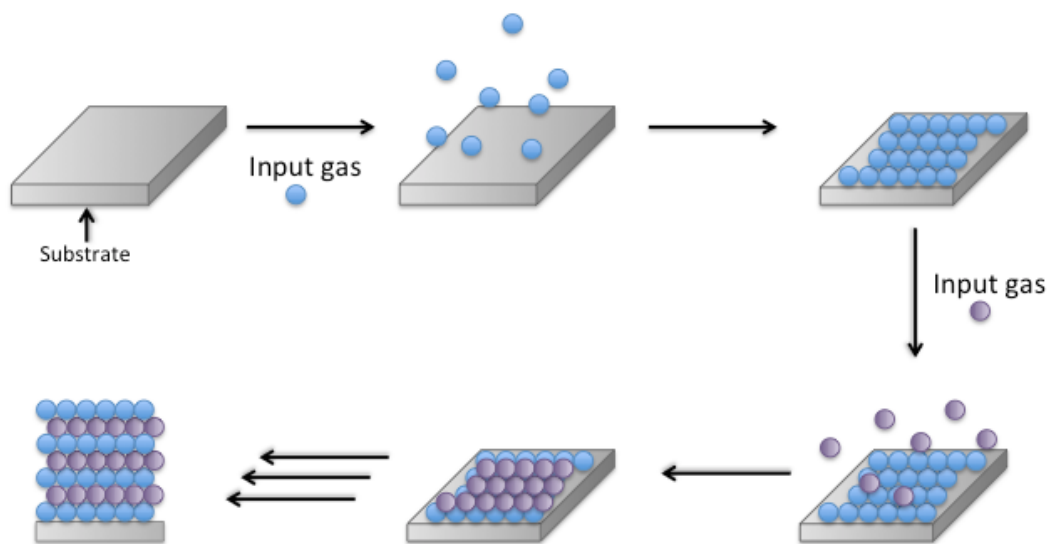


Figure 2.3. Depiction of thin film formation by atomic layer deposition (ALD) in which dosing of precursors and reactants are cycled with purging and stabilizing steps.

Here, stainless steel is coated with biocompatible materials through sol-gel deposition (silica) and ALD (silica, alumina or titania) for use in biomedical

applications. These coatings were evaluated for conformal coatings through cyclic voltammetry and were characterized by FTIR, XPS, EIS, VASE, SEM, AFM and AES. Coatings were stressed in a consistent, controllable method using three-point bending. Such bending tests have previously been used to study the structural integrity of ceramic films.(69) These coatings were then evaluated for their structural integrity through electrochemical evaluation. Following the evaluation of films, the ideal substrates can subsequently be functionalized through the addition of specific silanes. Much of this data was previously published and patented.(70,71)

RESULTS AND DISCUSSION

The goal of this portion of work is to determine an ideal interlayer, the best possible coating on stainless steel for further functionalization with desired molecules. Stainless steel was chosen as a substrate because it is one of the most widely used materials in biomedical implants and more specifically, for stents.(9,17-19) An SEM image of a stent can be seen above in Fig. 2.1.

Stainless steel spontaneously forms a passivating surface layer less than 10 nm thick, which generally inhibits further corrosion. However, in biological environments, corrosion of stainless steel can occur over time, and may cause the release of undesirable ions.(5,15,24-27) Additionally, one-electron reductions on the surface of stainless steel could cause a cascade on the surface of a biomedical implant that could lead to the loss of its utility.(12,15,29,34,37) For these two reasons, an insulating metal oxide coating was selected. Of the numerous options available, silica, alumina and titania offered two additional desirable properties – biocompatibility and ease of functionalization.(7,39,50-52,61-63)

A number of different deposition methods have been developed to deposit metal oxide thin films onto substrates. In order to evaluate the three deposition techniques of sol-gel dip coating, electrodeposition, and atomic layer deposition (ALD), a single metal oxide, silica, was selected. The functionalization of silica

surfaces has been well studied and is well understood. Below, the three different deposition techniques are depicted in Fig. 2.4.

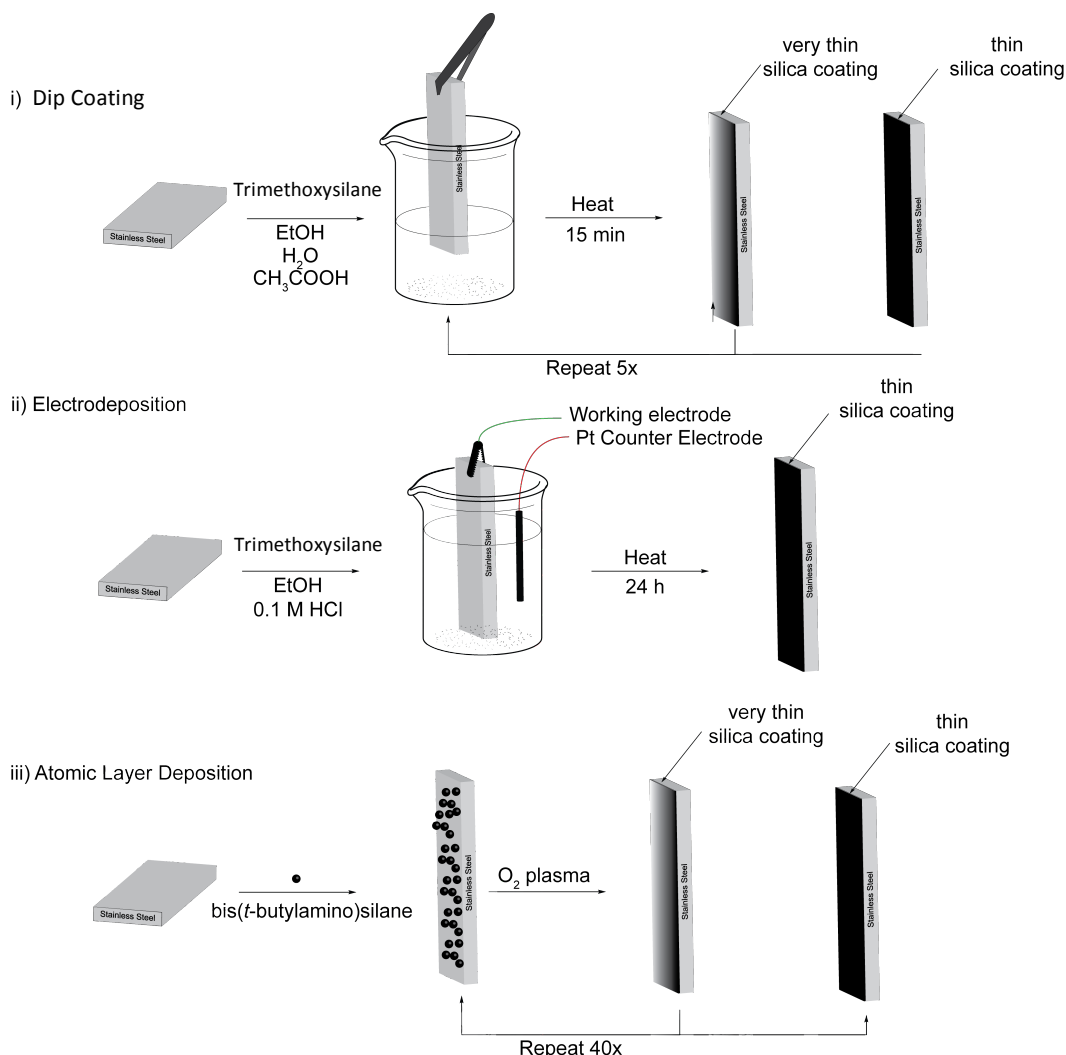


Figure 2.4. A depiction of the three deposition methods used to compare silica thin film coatings on 316L stainless steel: i) dip coating, ii) electrodeposition, or iii) atomic layer deposition. Adapted with permission from (70). Copyright 2011 American Chemical Society.

The silica coated stainless steel samples prepared by sol-gel dip coating and ALD were characterized by FTIR. Similar peaks were found in the spectra for each silica-coated stainless steel sample. Many characteristic peaks were found in the spectra, demonstrated in Fig. 2.5 and summarized in Table 2.1. Si-O-Si and Si-O asymmetric stretches were found in each spectrum, indicating the presence of

silica on each sample.(49,72) However, the presence of silica on the surface of these samples does not give a clear indication of the quality of the coating on stainless steel.

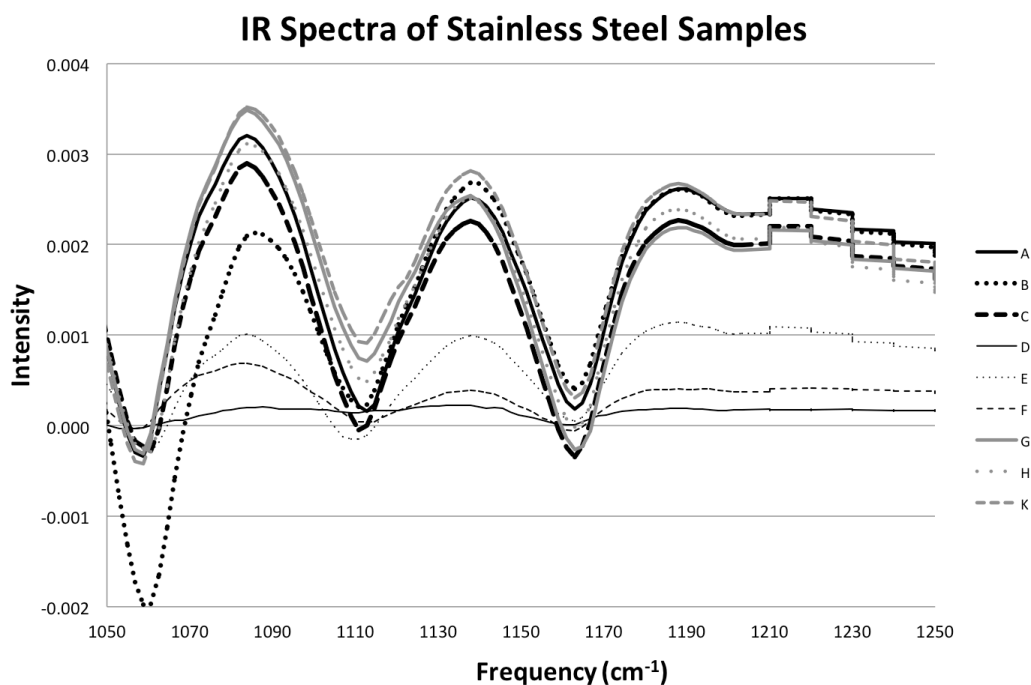


Figure 2.5. Characteristic infrared spectra of a variety of stainless steel samples, either uncoated or coated with silica. The sample labels correlate to Table 2.2.

Table 2.1. Infrared stretching frequencies found in stainless steel 316L coated with silica.

Frequency (cm ⁻¹)	Assignment
1190	Si-O asymmetric stretch
1140	Si-O-Si asymmetric stretch
1090	Si-O-Si asymmetric stretch

To assess the electrical accessibility of the stainless steel beneath the different silica coatings, the silica-coated stainless steel coupons were used as a working electrode in a standard three electrode cell as depicted in Fig. 2.6. The electroactive area of each sample was determined using cyclic voltammetry – an excellent way to detect faults in these insulating films. The idea behind this is demonstrated in Fig. 2.7. As depicted, the reduction of Ru³⁺ to Ru²⁺ is possible on

stainless steel, however, does not occur effectively on stainless steel coated with an insulating metal oxide coating like silica, alumina or titania. The amount of reduction of Ru^{3+} to Ru^{2+} is proportional to the area above the reduction peak. The area that is ineffectively coated, or that is electroactive, can be calculated from this area above the reduction peak.

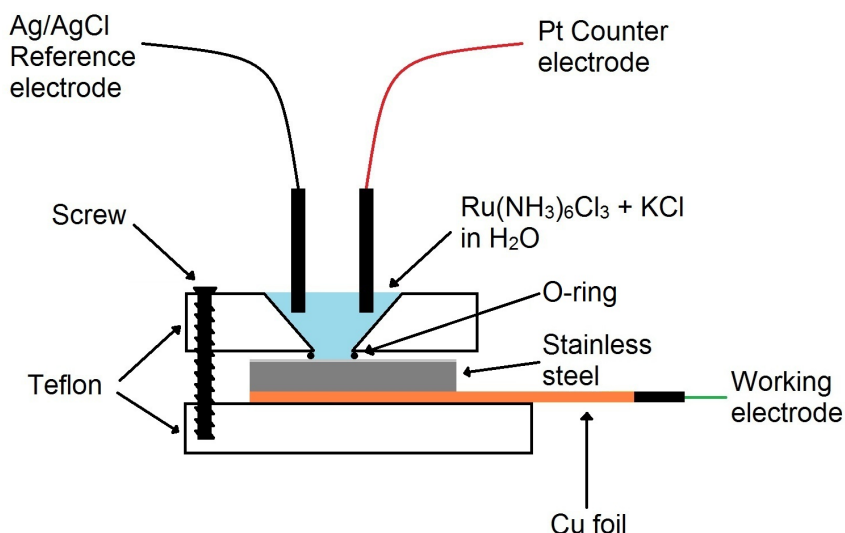


Figure 2.6. Experimental setup for electroactive area evaluation by cyclic voltammetry. Adapted with permission from (70). Copyright 2011 American Chemical Society.

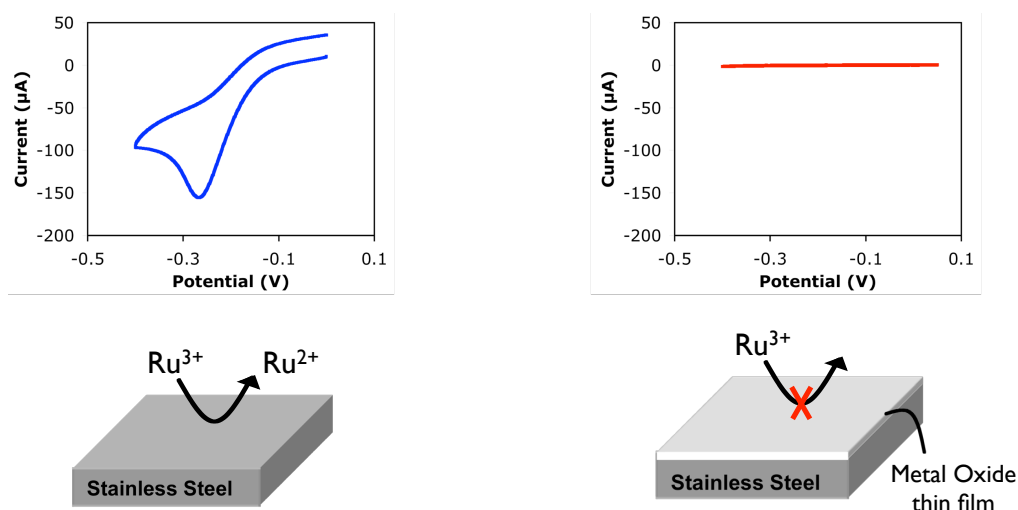


Figure 2.7. The reduction of a species such as Ru^{3+} to Ru^{2+} can take place on a conductive surface like stainless steel (left), however does not occur on a well-insulated surface such as stainless steel coated with a metal oxide thin film (right).

In Fig. 2.8i, representative cyclic voltammograms of clean 316L stainless steel and the PEG trimethoxysilane functionalized stainless steel are shown as A and B, respectively. Clearly, the two curves are qualitatively similar, indicating that the PEG coating is not electrically blocking to any great extent. The effective electroactive area of an electrode can be calculated from a plot of cyclic voltammogram peak current versus scan rate^{1/2} using the Randles-Sevcik equation.(73) The calculated electroactive area was divided by the area of the working electrode exposed to the electrolyte and was expressed as a percentage. For further details, refer to the experimental section. The values listed in Table 2.2 were averaged over six samples. Notable variation was observed between samples considering all were cut from the same 10 cm x 10 cm stainless steel foil. These variations can be attributed to the difference in composition of the alloy from one area to another and the resulting passivation layer.(74) Indeed, it can be observed in comparing the calculated electroactive area of clean 316L stainless steel to that of the PEG functionalized surface from Table 2.2 that there is little difference between the two as they are within experimental error. The presence of the metal oxide passivation layer is likely, in part, responsible for the calculated electroactive area of clean 316L stainless steel at 83% ($\pm 5\%$), which is less than 100% expected for an ideal conductor.

From the subsequent data in Table 2.2 obtained for the electroactive area of other silica layers using dip-coating methods in our studies, it can be observed that effective electric insulation has not been achieved. Silica films deposited by dip-coating methods could only reduce the electroactive area by up to 20%. On the other hand, it can be observed that electrodeposition proved a more effective means of depositing an electrically insulating silica thin film under our conditions – more than twice as effective in reducing the electroactive area of stainless steel in the case of electrodeposited TEOS. However, the electroactive area was reduced to below detectible limits using cyclic voltammetry when the silica thin film is deposited by ALD. This is also apparent in Fig. 2.8ii where no reduction peak can be observed in the CV. The functionalization of this ALD coated surface

with PEG silane does not alter, but may improve this electrical insulation. These results remain unaltered after applying scotch tape to the substrates.

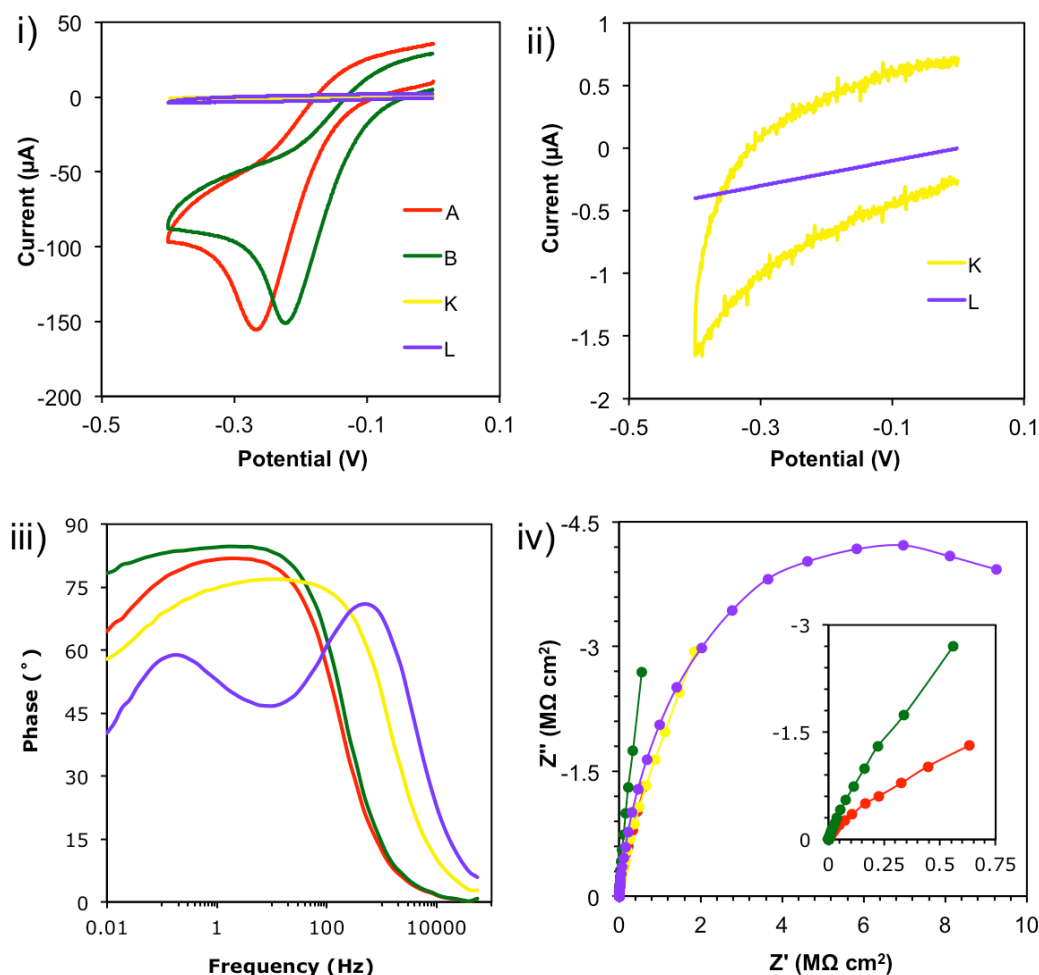


Figure 2.8. For all plots (i – iv) the red line (A) denotes clean 316L SS; the green line (B) is PEG silane functionalized 316L SS; the yellow line (K) is 316L SS coated with 5 nm of SiO₂ deposited via atomic layer deposition (ALD); and the purple line (L) is PEG silane functionalized ALD deposited SiO₂ on 316L SS. i) Cyclic voltammograms of A, B, K and L over the voltage range 0.0 V to -0.4 V versus Ag/AgCl in saturated KCl solution with 2 mM Ru(NH₃)₆Cl₃. ii) Cyclic voltammograms of K and L over the same voltage range. iii) Bode plot (phase versus frequency) of EIS response of A, B, K and L. iv) Nyquist plot of EIS response of A, B, K and L; inset shows only A and B on a smaller scale. Adapted with permission from (70). Copyright 2011 American Chemical Society.

Table 2.2. Electroactive area (measured by CV), film thicknesses (as determined by variable angle spectroscopic ellipsometry (VASE)), and fraction of Fe, Cr, Mo and Ni metals (as observed by low resolution XPS). Refer to Surface Characterization in the Experimental for further details. Adapted with permission from (70). Copyright 2011 American Chemical Society.

Sample	Electroactive Area (%)	Film Thickness (nm)	% Metal
Reference			
A) Clean 316L SS	83 (5)	6	11 (3)
Dip Coating			
B) PEG silane	78 (10)	7	4 (1)
C) 1,2-bis (trimethoxysilyl) ethane	67 (5)	8	1.2 (0.6)
D) 100% TEOS (No Curing)	79 (8)	6	3.0 (0.6)
E) 100% TEOS	75 (10)	8	6 (1)
F) 1:1 TEOS:100% EtOH	66 (8)	6	10 (1)
G) 1:1 TEOS:95% EtOH/AcOH	68 (8)	7	6 (2)
H) 1:1 TEOS:95% EtOH	73 (8)	8	8 (2)
Electrodeposition			
I) Electrodeposited PEG silane	54 (9)	40	0.7 (0.4)
J) Electrodeposited TEOS	18 (14)	103	2(2)
Atomic Layer Deposition			
K) ALD SiO ₂	0 (0)	11	0.7 (0.3)
L) ALD SiO ₂ - PEG silane	0 (0)	23	0.03 (0.04)

The little difference in electroactive area in Table 2.2 between the clean stainless steel (A) and the PEG silane dip-coated (B) samples is not surprising given the thickness of the dip coated PEG silane coating. Variable angle spectroscopy ellipsometry (VASE) measurements of (B), the PEG silane functionalized surface, attribute a Cauchy dielectric thickness of 7 nm versus 6 nm for clean stainless steel (A), also in Table 2.2. In fact, there is negligible difference between the curve-fitted VASE data from each of the dip-coated silica coatings (samples B-H). The thickest coatings were obtained by electrodeposition (samples I and J), followed by ALD (samples K and L). Although the electrodeposited coatings are thicker according to the VASE measurements, they are less electrically insulating

than the ALD silica coatings on stainless steel as demonstrated by the larger electroactive areas of the electrodeposited samples. To further examine the electrodeposited films, an SEM image was obtained of the thickest coating according to the VASE measurements, the electrodeposited TEOS coating (J), and is shown in Fig. 2.9. It is evident from the SEM image that portions of the film obtained by this method are quite thick. However, the film is inconsistent and rough, giving rise to the incomplete electrical insulation of the stainless steel. The averaged thickness value offered by the VASE measurement cannot reflect this inconsistency, highlighting the necessity of corroborating data.

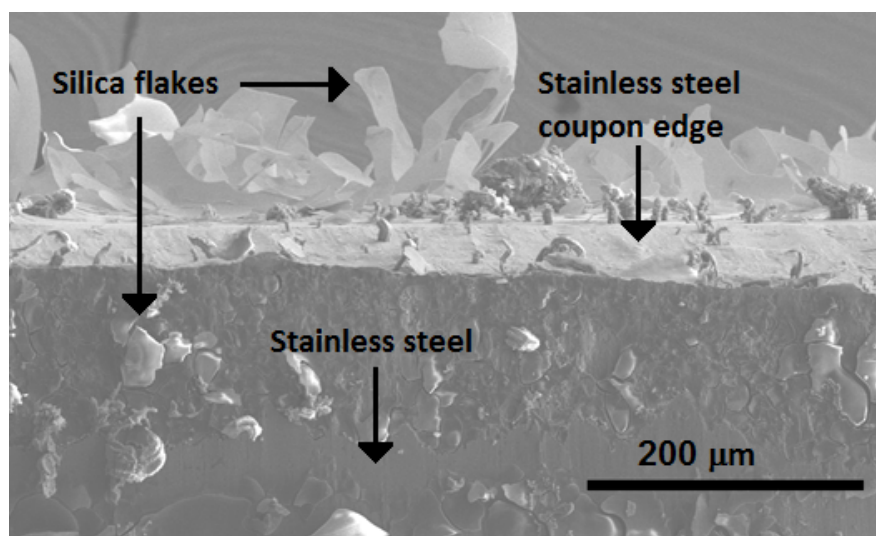


Figure 2.9. Scattered electron SEM image from the side of a 316L stainless steel coupon with a TEOS electrodeposited silica coating (J). Adapted with permission from (70). Copyright 2011 American Chemical Society.

Additional topography comparisons were performed by AFM. The results from clean stainless steel, and dip coated and ALD silica coated stainless steel can be compared in Fig. 2.10. These results indicate that there is no discernable difference between the samples on this scale. The topography of the stainless steel is so rough that any differences that arise from the silica deposited by dip coating and ALD are negligible. This was also found by SEM imaging (not shown).

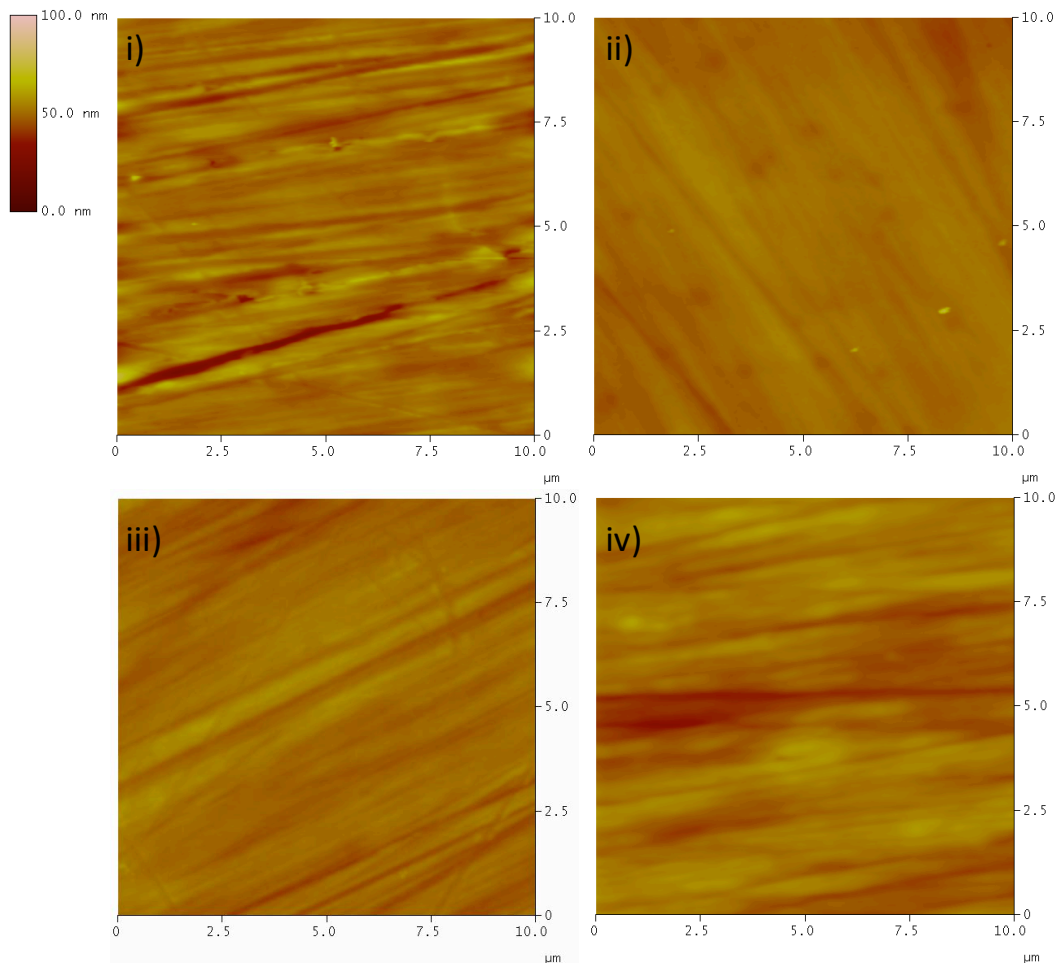


Figure 2.10. AFM height images of i) clean SS, and ii) PEG, iii) Heat Cure 50% TEOS: 50% EtOH, and iv) silica ALD on stainless steel 316L. The height scale is to the left for all samples.

In contrast to the TEOS electrodeposited silica coating, the film thickness of the silica ALD coating is very thin, less than 15 nm thick according to VASE. Yet the thinner silica ALD coating demonstrates superior insulating properties on stainless steel, apparent by the effective electroactive area of 0%. Some interesting observations can be made in comparing the ALD silica coated stainless steel subsequently functionalized with PEG silane and the PEG silane functionalized 316L stainless steel (L and B respectively) in Table 2.2. From Fig. 2.8i), the representative cyclic voltammograms of ALD SiO₂ coated stainless steel (K) and PEG silane functionalized ALD SiO₂ coated stainless steel (L) can be directly compared with those of clean 316L stainless steel (A) and PEG silane

functionalized stainless steel (B). The cyclic voltammograms of both the ALD coated samples appear as flat lines on the same scale as clean and PEG silane functionalized stainless steel. Clearly, the ALD SiO₂ coating effectively insulates the stainless steel samples. Fig. 2.8ii shows the cyclic voltammograms of ALD coated stainless steel and PEG silane functionalized ALD coated stainless steel on a smaller current scale. On this scale it is apparent that the shape of the cyclic voltammograms of the ALD SiO₂ coated samples are different from that of the clean and PEG silane functionalized stainless steel. The small amount of current measured in the cyclic voltammogram is due to capacitive charging of the system. No reduction peak is present in either cyclic voltammograms, which indicates that no pinholes are present in the ALD SiO₂ coating. If this were not the case, the Ru(NH₃)₆³⁺ species would be able to undergo reduction at the stainless steel working electrode of the cell, and thus to the sensitivity limit of our apparatus, the ALD silica coating acts as a perfect blocking layer.

The different silica-coated stainless steel surfaces were also examined with low resolution X-ray photoelectron spectroscopy (XPS). The atomic percentages of silicon and alloy metals (i.e., Fe, Cr, and Ni) for each of the samples are presented in Fig. 2.11. The atomic percentages of silicon for each of the samples do not correlate with either the electroactive area measurements or the thickness measurements. In particular, samples I-L have the thickest coatings according to VASE measurements and the smallest electroactive areas according to cyclic voltammetry, yet have no apparent correlation in their percentages of silicon and alloy metals in comparison to the rest of the samples. However, it can be observed that well-insulated samples from Table 2.2 generally have high silicon content and low alloy metal content. Exceptions to this exist where silanes used to coat the stainless steel have silicon-carbon bonds, which are unreactive under the sol-gel (both dip-coating and electrodeposition) reaction conditions. Although an alkoxy silane functionality can undergo hydrolysis and condensation reactions to produce Si-O-Si from the Si-O-C in the precursors, a Si-C bond will remain

intact.(58,72) A large carbon content, which remains a part of the attached silane on the surface, in turn decreases the percentage of silicon detected.

Elemental Analysis by Low Resolution XPS

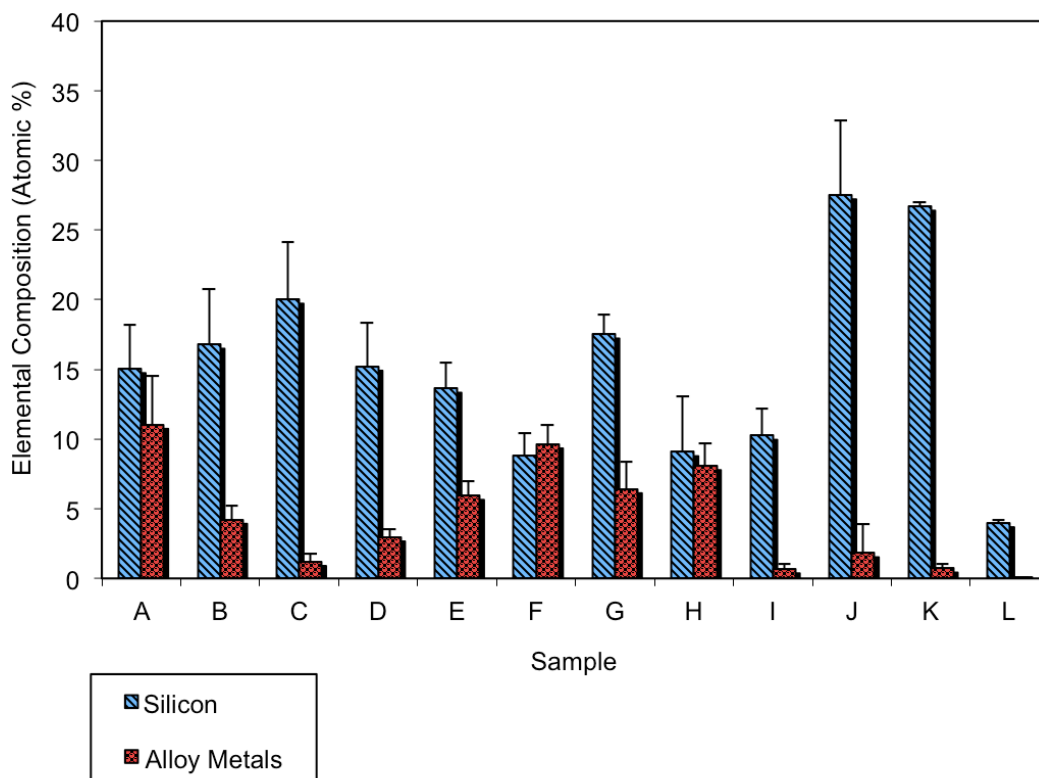


Figure 2.11. Elemental composition in atomic percent determined by low resolution XPS. Alloys metals are the sum of Fe, Cr, Mo and Ni signals. Adapted with permission from (70). Copyright 2011 American Chemical Society.

Additionally from Fig. 2.11, the alloy metal (i.e., Fe, Cr, and Ni) atomic percentages in the clean and PEG silane functionalized surfaces (samples A and B respectively) revealed significant decrease from 11% to 3%, which can be attributed to an increased carbon and oxygen atomic percentage from the poly(ethylene glycol) chains. The detection of metal signals in the XPS spectrum of the electrodeposited PEG silane functionalized surface (sample I) can be attributed to incomplete surface coverage, as VASE measurements estimate a 40 nm thickness, but the cyclic voltammetry indicates that the electroactive area is around 50%. Another notable observation is that the most insulated samples (K

and L) also have the smallest standard deviations associated with them. This correlates well with the electroactive area measurements. This may be indicative of a more uniform and consistent coating of the stainless steel being achieved through ALD.

The fine control of silica film thickness in an ALD experiment is demonstrated in Fig. 2.12. In this experiment, ALD was performed on cleaned silicon substrates using the parameters described in the experimental section, varying only the number of repeat cycles in the ALD process. A linear thickness evolution was observed and a growth rate of 0.123 nm/cycle was determined.

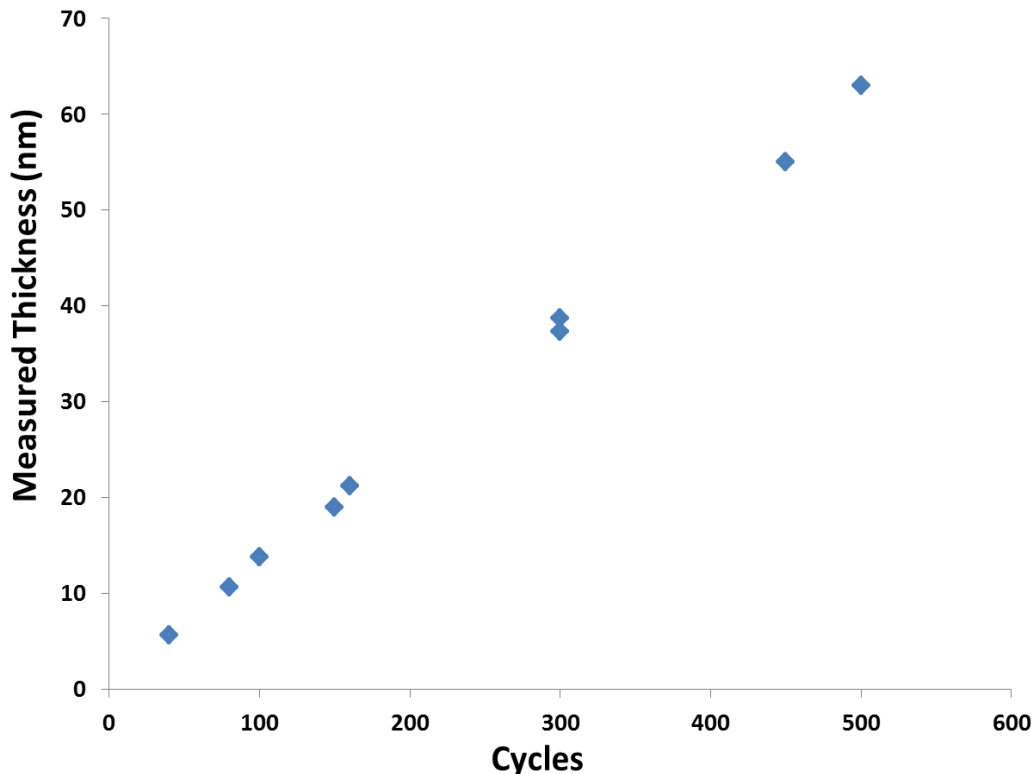


Figure 2.12. Plot of the dielectric thickness measured by VASE for a selection of silica thin films deposited by ALD. Adapted with permission from (70). Copyright 2011 American Chemical Society.

One point of note is that the silicon atomic percentages determined by XPS were similar between clean and PEG silane coated stainless steel at approximately 15%, as averaged over five spots per sample, as shown in Fig. 2.11. The presence

of silicon in the stainless steel coupons was verified by EDX. Depth profiling of the clean 316L stainless surface, and the silicon, oxygen and chromium was evaluated by high resolution XPS. This data is presented in Fig. 2.13. These spectra revealed that only the top 2 nm contained appreciable silicon, and the elimination of this silicon signal was correlated with a chromium peak shift from 576.5 eV to 574.1 eV which indicates a change from Cr(III) to Cr(0).(75,76) Since chromium oxide is the major component of the native passivation oxide of stainless steel, and the metallic chromium indicates the end of the surface oxide, accordingly, the silicon contamination is restricted to the passivation layer of the clean 316L. This additional silicon in the oxide passivation layer may have also contributed to a decrease in the electroactive area from the expected 100% of the clean 316L stainless steel surface noted previously. The silicon may be present at the surface due to the casting or cutting process.(77)

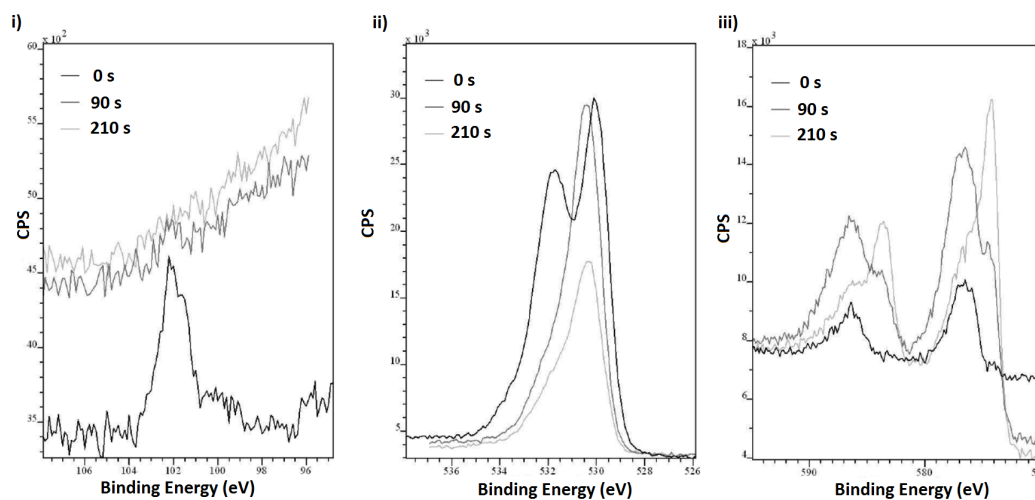


Figure 2.13. High resolution XPS of i) Si2p ii) O1s and iii) Cr2p peaks from a clean stainless steel coupon. A sputtering rate of 0.5 nm per minute was used in order to get a depth profile. Adapted with permission from (70). Copyright 2011 American Chemical Society.

Stainless steel stents were also used as substrates and were evaluated by Auger electron spectroscopy (AES) to compare their elemental composition. Two of these evaluations are presented in Fig. 2.14 and 2.15 where one stent was evaluated as received and the second stent was functionalized with silica by dip

coating using the 100% TEOS procedure. In contrast to the stainless steel coupons, no silicon was detected in the uncoated stainless steel stents. However, silicon was detected in the stent coated with silica by dip coating. From this data, further study was done on this type of dip coating. Preliminary assessment of the functionalization silica coated stainless steel was performed on this type of coating, which will briefly be discussed in the functionalization chapter.

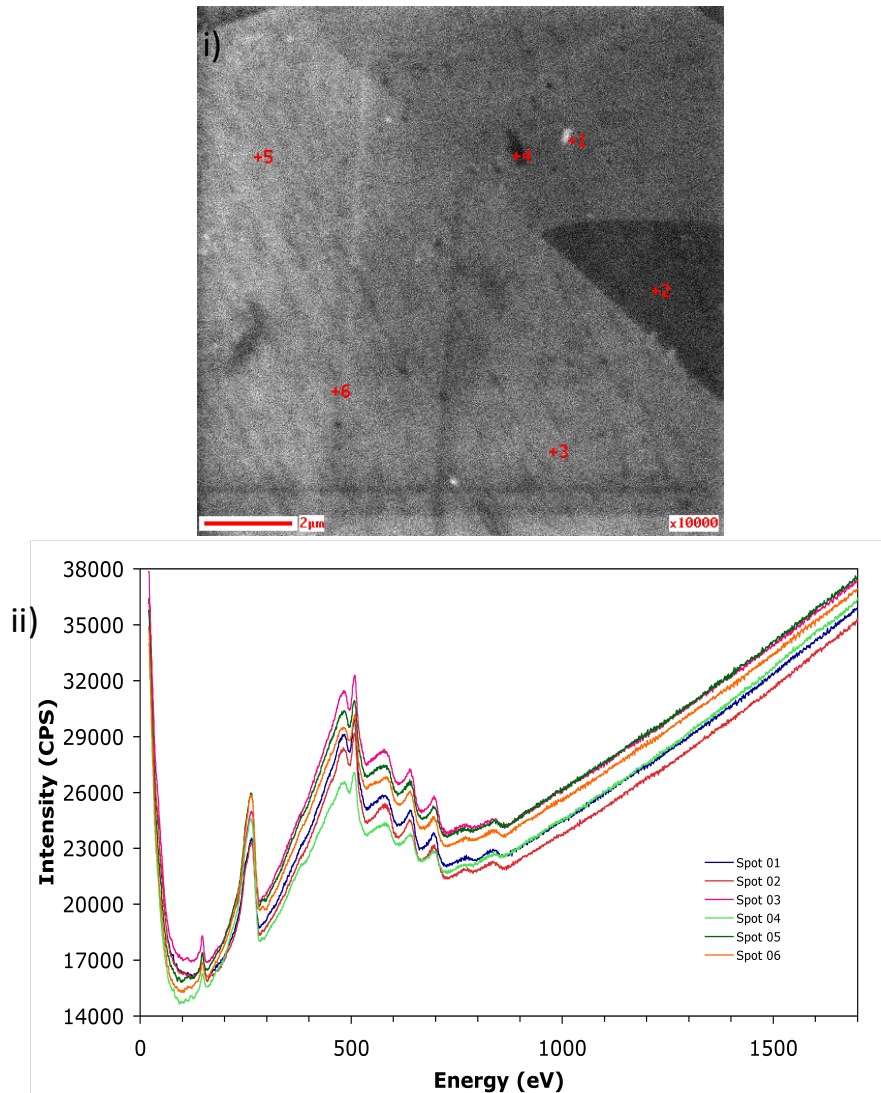


Figure 2.14. i) A scanning electron micrograph (SEM) of an untreated 316L stainless steel stent. The crosses indicate sample points at which Auger electron spectroscopy (AES) was performed. The scale bar is 2 μm . ii) AES of an untreated 316L stainless steel stent. The spectra reveal signals for Fe, Cr, Ni, C, and O but not silicon.

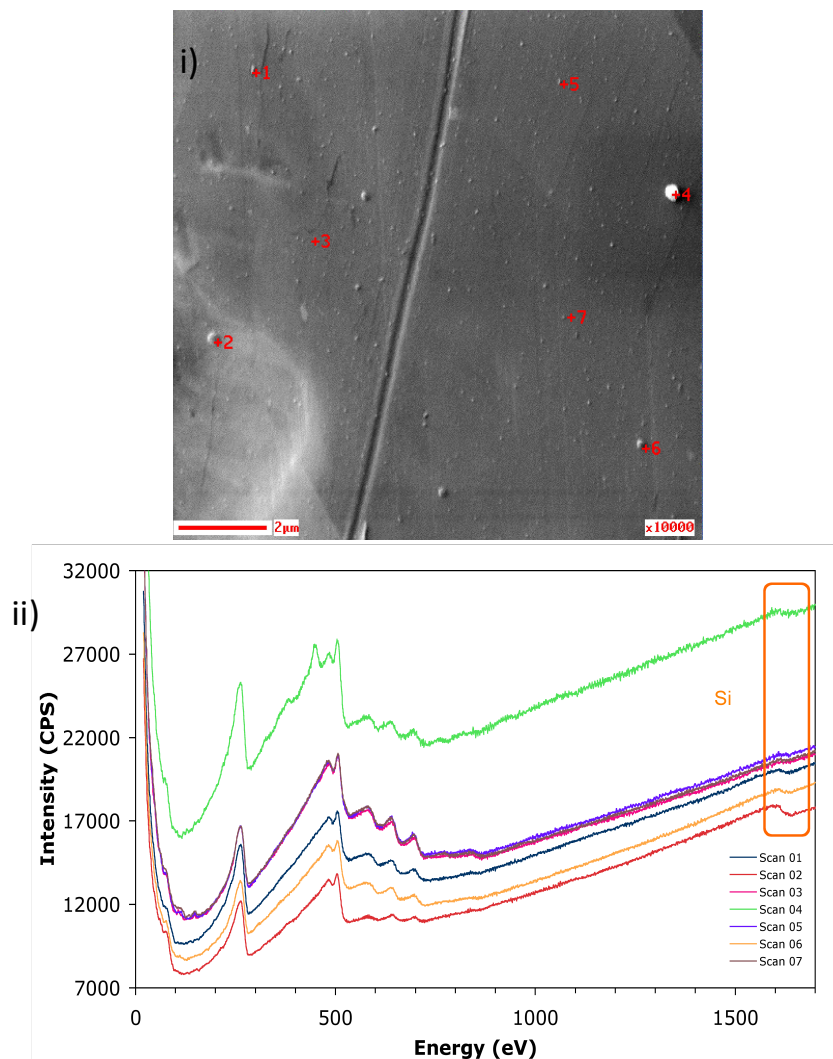


Figure 2.15. i) An SEM of a 316L stainless steel stent covered with an SiO₂ layer, prepared using a TEOS dip. The crosses indicate sample points at which Auger electron spectroscopy (AES) was performed. The scale bar is 2 μm. ii) AES of seven spots on a SiO₂ coated 316L stainless steel stent. The spectra reveal signals for Fe, Cr, Ni, C, and O, as well as Si. The signal for silicon is expected at a binding energy of approximately 1615 eV, and has been highlighted with a rectangle in ii).

To further evaluate ALD coatings, three different metal oxides, silica, alumina, and titania, were chosen to coat stainless steel by ALD. Limited evaluation of the alumina coating was performed, which is discussed below. However, to evaluate the adherence of the silica and titania coated stainless steel, they were stressed by three point bending using a dynamic mechanical analyzer, shown in Fig. 2.16.

This was done to determine the optimal surface treatment and coating for stents upon stressing since stents are expanded during implantation. Three point bending offered a consistent, controllable method of performing stressing on the stainless steel coupons. This stressing was performed for an hour on each of the uncoated stainless steel, the stainless steel coated with silica, and the stainless steel coated with titania.

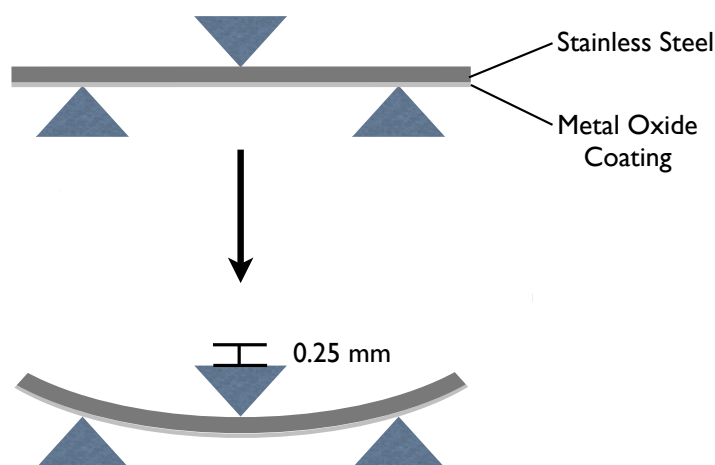


Figure 2.16. Three point bending is used to reproducibly stress the stainless steel coupons uncoated and coated by ALD with silica or titania.

Additionally, three different surface treatments were used to ensure optimal surface condition of the stainless steel for increased adhesion of the ceramic coatings fabricated by ALD. Depending on the surface cleaning method, the concentration of hydroxy groups present on the stainless steel surface varies.(2,49,78,79) Given a sufficiently hydroxy rich surface, alkoxy silanes tend to form covalent bonds primarily with the surface and do not cross-polymerize with neighbouring alkoxy silanes. However, if there are insufficient hydroxy groups to satisfy the bonding of the trialkoxy silanes to the surface, they will tend to bind to each other rather than the stainless steel surface.(80) By extension, it is useful to know if the surface treatment method could enhance the adherence of the silica or titania ALD coatings. In order to fabricate a thin, conformal coating, surface hydroxides are required. Surface treatments used to hydrolyze the surface include a piranha dip, a nitric acid dip or an air plasma clean in an attempt to

enhance the bonding of thin ceramic coatings to the native oxide of stainless steel. Piranha dip was previously used to hydroxylate silica substrates in order to functionalize them with silanes.(2,70,81) Nitric acid treatments have also shown promise for attachment of further coatings such as silica.(78) Air plasma has previously been used on stainless steel to then coat with silica.(49,79) All samples were made and evaluated in triplicate to ensure statistical significance.

To determine the consistency of these films following stressing, the electroactive area was calculated from cyclic voltammetry measurements. Again, this is an effective method to determine the difference between a well-insulated pin-hole free coating and a coating with faults which is ineffective in insulating a metallic substrate. To ensure consistency in the evaluation of substrates, only one side of the stainless steel coupons was coated and a fixed area was evaluated with cyclic voltammetry and the ruthenium solution was replenished from the same stock solution for the evaluation of each substrate. The electrochemical cell setup is the same as shown above in Fig. 2.6.

It was determined that after an hour of stressing by three point bending, all the silica-coated samples were still consistently electrically insulated, whereas a couple of the titania coated samples were less electrically insulating. This can be seen in the cyclic voltammograms, in Fig. 2.17. The CV in blue of stainless steel demonstrates a clear reduction peak. The CV in orange of stainless steel with the silica ALD coating demonstrates that it is well-insulated. The CV in purple of stainless steel with the titania ALD coating demonstrates that it is well-insulated in comparison to uncoated stainless steel, but that it is slightly less effective than the silica coating. The CV in green of the stainless steel with titania ALD coating after bending demonstrates an example where following bending, the titania coating is no longer effectively insulating. Specifically, of the titania coatings that were no longer effectively insulating following bending, the surface treatments were different – one was subjected to a piranha dip while another was plasma cleaned. So, although silica was determined to be the ideal ceramic coating since

it moderately outperformed the titania coatings, the surface treatment had little impact on the adhesion of the coatings.

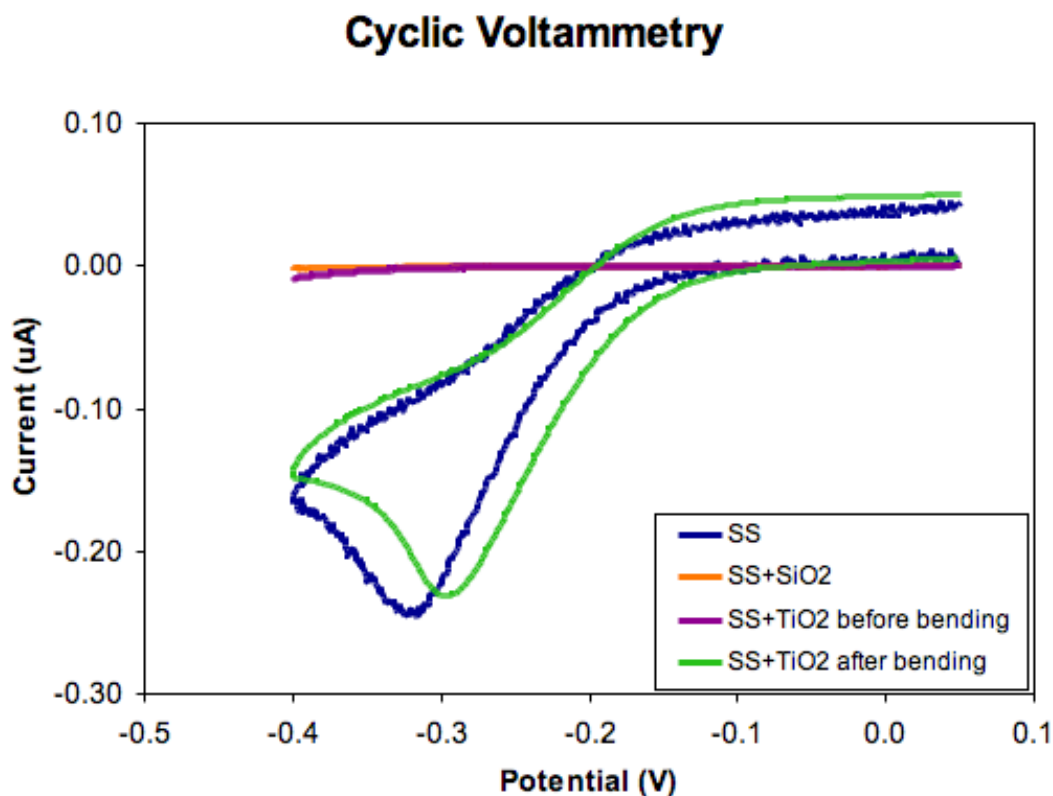


Figure 2.17. Representative cyclic voltammograms (CV) of the stainless steel (SS) and stainless steel coated by ALD with silica and titania, and titania following three-point bending which is no longer electrically insulating.

Although preliminary electrochemical data for alumina ALD films was obtained, the silica ALD films performance under stress conditions could not be surpassed within the limits of our experimentation. These alumina thin films were also promising in their functionalization with specific silanes (discussed in the following chapter). However, silica is an easier substrate to work with – the native oxide layer of silicon wafers could be functionalized with specific silanes and be directly characterized by IR (since silicon is IR transparent). Additionally, glass microscope slides and silicon wafers were readily available, which offered additional characterization that would have been more difficult to obtain for alumina. As such, further study of the alumina ALD film was not performed.

The silica ALD coatings have better insulating performance characteristics than the other types of coatings as characterized by cyclic voltammetry. Additionally, the coatings are thin, as shown by VASE data, and the coatings are conformal, as shown by the AFM images. Silica ALD coatings on stainless steel also outperform titania ALD coatings under stress conditions.

CONCLUSIONS

Silica coatings deposited by ALD on stainless steel was determined to be an ideal substrate for application on stents. They outperform silica thin films deposited onto stainless steel both by dip coating and by electrodeposition of sol-gels, as characterized by cyclic voltammetry and corroborated by the EIS. They also offer a thinner, more conformal coatings as determined by VASE and SEM, which seemed to be corroborated by XPS data. Silica thin films also moderately outperformed the titania coating on stainless steel under stress conditions as performed by three point bending and evaluated by cyclic voltammetry by determining the electroactive area. The surface pretreatment of the surfaces does not appear to greatly effect quality of the ALD metal oxide coatings. The ALD silica coated thin films on stainless steel were subsequently functionalized with specific silanes, as explained in the next chapter.

EXPERIMENTAL

Materials.

Nitric acid and sulphuric acid were purchased from J. T. Baker and used as received. Hydrogen peroxide, methylene chloride and acetone were purchased from Fischer Scientific and used as received. Glacial acetic acid, sodium chloride (ACS grade), magnesium chloride hexahydrate (ACS grade), potassium chloride (ACS grade), calcium chloride (anhydrous), and sodium bicarbonate (ACS grade) were purchased from EMD and used as received. 100% ethanol was purchased from Commercial Alcohols and used as received. Tetraethyl orthosilicate (reagent grade, 98%), 3-mercaptopropyl trimethoxysilane (MPTMS), 1,2-

bis(trimethoxysilyl)ethane, and potassium chloride (99.999%) were purchased from Aldrich and used as received. 2-[methoxy(polyethyleneoxy)propyl]-trimethoxysilane (6-9 or 9-12 repeat units; referred to as PEG silane) was purchased from Gelest Inc. and used as received. 18 M Ω (Barnstead) water was freshly generated before use. 0.9 mm thick and 0.1 mm annealed, mirror polished both sides stainless steel AISI 316L (Fe/Cr18/Ni10/Mo3) foil was purchased from Goodfellow Cambridge Limited. [Ru(NH₃)₆]Cl₃ was purchased from Strem Chemicals, and used as received. Palmaz-Schatz PS204C balloon expandable stainless steel stents were obtained from Johnson & Johnson (Miami, FL).

Methods.

Preparation and cleaning of stainless steel coupons

The 0.9 mm thick 316L stainless steel foil was rinsed with chloroform, ethanol, and pentane before being cut typically into 1 cm x 1 cm pieces with a press. Samples that were coated by electrodeposition were cut into 2.5 cm x 0.5 cm pieces or 1.5 cm x 1.5 cm to fit in the electrochemical setup shown in Fig. 2.6. Thinner stainless steel foil (0.1 mm) was used for the DMA studies, and they were cut into pieces 2.5 cm x 1.1 cm, which also allowed for the standardized electrochemical characterization. All samples of 316L stainless steel substrate were ultrasonically cleaned for 10 minutes in four solvents (18 M Ω H₂O, CH₂Cl₂, acetone, ethanol). Subsequently, the stainless steel sample was treated with air plasma for 60 minutes at a pressure of \sim 0.8 mTorr (Harrick Plasma, PDC32G, 18W).(82)

The different surface treatments of stainless steel samples before ALD coating involved dipping into either nitric acid or piranha for 15 minutes instead of the air plasma treatment for 60 minutes. A 5% nitric acid was in 100% ethanol using 70% nitric acid.(78,81) The piranha solution was prepared from a 1:3 mixture of concentrated sulfuric acid: 30% hydrogen peroxide. *[WARNING: The preparation of piranha solution is highly exothermic, and the mixture extremely reactive toward organic solvents. Preparation and use of piranha should be performed*

with extreme caution!] The piranha-cleaned substrates were washed with copious amounts of 18 M Ω •cm water to dilute the reactive piranha, and dried with nitrogen. In the majority of procedures samples were heat cured for 15 minutes at 110°C in a Thelco laboratory oven model 130DM.

For samples that were examined electrochemically, the stainless steel foil was covered on one side with adhesive putty, which was pressed onto a glass slide so that 6 samples could be prepared in tandem. This left one side unexposed to the silica precursor solutions. Following the dip procedure, the sample side exposed to the adhesive putty was rinsed with water, toluene, pentane, dichloromethane, acetonitrile, acetone and ethanol.

Formation of silica coatings on 316L stainless steel surfaces by dip-coating

97:2:1 95% EtOH: PEG: AcOH (used for preparing B and L samples). In a typical experiment, 22 μ L of 2-[methoxy(polyethyleneoxy)propyl]-trimethoxysilane (6-9 PEG repeat units, 24 mg; 4.33×10^{-5} mol) was dissolved in 1.0 mL of acidified 95% ethanol (1% v/v acetic acid). The silane solution was agitated for 5 minutes before freshly plasma cleaned silica coated 316L stainless steel sample was stirred through the silane solution for 2 minutes. The stainless steel samples were dip rinsed in 100% ethanol, and cured for 15 minutes in an oven heated to 110°C.

100% TEOS (used for preparing C samples). Upon removal from the plasma cleaner, the stainless steel foil was kept in 18 M Ω H₂O until it was dipped into the silica precursor (typically 5-15 minutes). The stainless steel foil was then dried under nitrogen and immediately immersed in neat TEOS. After 15 seconds, the stainless steel sample was removed, and submerged in 18 M Ω H₂O for 120 seconds.(49) The 316L stainless steel foil was dried under a stream of nitrogen before being immersed again into neat TEOS, completing one cycle. This cycle was typically repeated 5 times. Upon completion of the cycles, the stainless steel foil was left sitting in 18 M Ω H₂O for 1 hour.

100% TEOS (HC) (used for preparing D samples). The freshly cleaned 316L stainless steel foil samples were immersed in neat TEOS for 15 seconds. The edge of the sample was dabbed on a kimwipe to remove excess TEOS, and then cured for 15 minutes in an oven heated to 110°C, completing a cycle. Samples were immersed in 18 MΩ H₂O for 5 minutes and dried under nitrogen prior to being immersed in neat TEOS to commence the second cycle. Typically 5 cycles were performed.

1:1 TEOS:100% EtOH(used for preparing E samples). The freshly cleaned 316L stainless steel foil samples were immersed for 15 seconds in a solution that consisted of a 1:1 volume ratio of 100% ethanol and TEOS. Excess TEOS was removed with a kimwipe, and then samples were cured for 15 minutes in an oven heated to 110°C, completing the cycle. Subsequently, samples were immersed in 18 MΩ H₂O for 5 minutes and dried under nitrogen prior to being immersed in the silica precursor solution to commence the second cycle. Typically 5 cycles were performed.

1:1 TEOS:95% EtOH(used for preparing F samples). The freshly cleaned 316L stainless steel foil samples were immersed for 15 seconds in a solution that consisted of a 1:1 volume ratio of 95% ethanol and TEOS. Excess TEOS was removed with a kimwipe, and then samples were cured for 15 minutes in an oven heated to 110°C, completing the cycle. Subsequently, samples were immersed in 18 MΩ H₂O for 5 minutes and dried under nitrogen prior to immersion in the silica precursor solution to commence the second cycle. Typically 5 cycles were performed.

50:49.5:0.5 TEOS: 95% EtOH: AcOH (used for preparing G samples). The freshly cleaned 316L stainless steel foil samples were immersed for 15 seconds in a solution that consisted of a 1:1 volume ratio of 95% ethanol (1% acetic acid by volume) and TEOS. Excess TEOS was removed with a kimwipe, and then

samples were cured for 15 minutes in an oven heated to 110°C, completing the cycle. Subsequently, samples were immersed in 18 MΩ H₂O for 5 minutes and dried under nitrogen prior to being immersed in the silica precursor solution to commence the second cycle. Typically 5 cycles were performed.

97:2:1 95% EtOH: 1,2-bis(trimethoxysilyl)ethane: AcOH (used for preparing H samples). The freshly cleaned 316L steel samples were immediately immersed in an acidic ethanolic solution (95% ethanol, 1% acetic acid by volume) of 1,2-bistrimethoxysilylethane, and agitated for 120 seconds. Subsequently, the sample was dip rinsed in 100% ethanol before being cured for 15 minutes in an oven heated to 110°C.

Formation of silica coatings on 316L stainless steel surfaces by electrodeposition TEOS (used for preparing I samples). A sol-gel solution was prepared from 6.5 mL of ethanol, 1.0 mL of TEOS, and 2.5 mL of 0.1 M HCl and was stirred for at least three hours before use.⁽⁴⁵⁾ The sol-gel solution remained translucent for more than one month. Typically, a 1.5 cm x 1.5 cm 316L stainless steel coupon with 1.54 cm² exposed via a Teflon cell was the working electrode shown in Fig. 2.6. Heavy aluminum foil instead of the copper foil was used to make electrical contact with the stainless steel sample for electrodeposition. The counter electrode used was a platinum wire and Ag/AgCl in saturated KCl was used as a reference electrode. The current was monitored while -1 V was applied for 60 seconds. The stainless steel sample then removed from the Teflon cell, followed by rinsing with methanol. The sample was then left to dry in air for 24 hours followed by curing in an oven at 110°C for 24 hours.

PEG(9-12) silane (used for preparing J samples). A sol-gel solution was prepared from 6.5 mL of ethanol, 1.0 mL of PEG silane (9-12 PEG repeat units), and 2.5 mL of 0.1 M HCl and was stirred for at least three hours before use.⁽⁴⁵⁾ The sol-gel solution remained translucent for more than one month. Typically, a 1.5 cm x 1.5 cm 316L stainless steel coupon with 1.54 cm² exposed via a Teflon cell was

the working electrode shown in Fig. 2.6. Heavy aluminum foil was used instead of copper foil to make electrical contact with the stainless steel sample for the electrodeposition. The counter electrode used was a platinum wire and Ag/AgCl in saturated KCl was used as a reference electrode. The current was monitored while -1 V was applied for 60 seconds. The stainless steel sample then removed from the Teflon cell, followed by rinsing with methanol. The sample was then left to dry in air for 24 hours followed by curing in an oven at 110°C for 24 hours.

Preparation of coated stainless steel surfaces using ALD Silica (used for preparing K and L samples). Stainless steel samples were placed in an Oxford Industries FlexAL atomic layer deposition (ALD) apparatus within an hour of cleaning. During deposition, the substrates were maintained at 300°C. 40 sccm of oxygen was continuously passed through the plasma source. The ALD chamber was first evacuated for 180 s to achieve a base pressure $<5 \times 10^{-6}$ torr. Then the chamber was cycled through process gas flush and prestabilization steps, followed by a five step deposition cycle to build the appropriate silica film thickness. Each cycle begins with a 600 ms dose of bis(tertiarybutylamino)silane (BTBAS) at 80 mTorr delivered with a 30 sccm flow of argon carrier gas. A 5.5 s purge of 30 sccm argon at 15 mtorr was used to remove excess or loosely bound BTBAS from the deposition chamber in. Argon flow to the process chamber was then shut down, and the gas environment was allowed to restabilize for 2.5 s at 15 mtorr. 250W oxygen plasma was then initiated and maintained for 5 s at 15 mtorr. The final step of the cycle was a second, post-plasma, argon purge was then performed for 2 s at 15 mtorr. This process was repeated a specified number of times to produce silica films of the desired thickness. The growth per cycle was determined to be 1.23Å/cycle with careful calibration, such that a 40-cycle process resulted in the deposition of approximately 5 nm of SiO₂. A Si(100) witness substrate was always included in the deposition chamber, and this witness was later examined by variable angle spectroscopic ellipsometry (VASE) to allow for thickness verification. For silica ALD samples that were subsequently

functionalized, the 97:2:1 95% EtOH: PEG: AcOH dip coating procedure was performed to functionalize with PEG.

Alumina. Freshly cleaned stainless steel was placed in an Oxford Industries FlexAL for Atomic Layer Deposition (ALD). The substrates were first heated and maintained at 300°C. The chamber was then evacuated to $<5 \times 10^{-6}$ torr. A four-step repeating cycle was used to build the layers of alumina. The chamber was dosed for 30 milliseconds with trimethylaluminum, followed by purging of the chamber with argon for 4 seconds. followed by exposure to a 300 W oxygen plasma for 3 seconds and an additional purge for 800 milliseconds, during which the pressure was maintained at 15 mTorr. This cycle of alumina precursor addition, and plasma pulsing was repeated, throughout which oxygen was continually flowing at 60 sccm. Flat samples and stents were exposed to the same number of cycles on each side. Each cycle makes a layer of approximately 1.05 Å in thickness. This process was repeated a specified number of times to produce silica films of the desired thickness. A 47-cycle process resulted in the deposition of approximately 5 nm of Al₂O₃. During every ALD process, a Si(100) witness substrate was always included in the deposition chamber, and this witness was examined by variable angle spectroscopic ellipsometry (VASE) in addition to the Al₂O₃-coated 316L stainless steel samples.

Titania. Freshly cleaned stainless steel samples were placed in an Oxford Industries FlexAL atomic layer deposition (ALD) apparatus. During deposition, the substrates were maintained at a temperature of 300°C. To begin the process, the ALD chamber was first evacuated for 180 s to achieve a base pressure in the range $<5 \times 10^{-6}$ torr, followed by several process gas flush and prestabilization steps. The deposition chamber was then repeatedly cycled through a five-step sequence to build up a titania coating of the desired thickness. In each cycle, the chamber was first dosed for 4 s with titanium isopropoxide (TIPO) at 80 mTorr delivered with a 30 sccm flow of argon carrier gas. Excess or loosely bound TIPO was then removed from the deposition chamber in a 4 s purge step using 30 sccm

argon at 15 mtorr. Argon flow to the process chamber was then shut down, and the gas environment was allowed to restabilize for 6 s at 15 mtorr. 300W oxygen plasma was then initiated and maintained for 4 s at 15 mtorr. A second, post-plasma, argon purge was then performed for 4 s at 15 mtorr, completing the sequence. This process was repeated a specified number of times to produce titania films of the desired thickness. With careful calibration, growth per cycle was determined to be 0.49 Å/cycle, such that a 100 cycle process resulted in the deposition of approximately 5 nm of TiO₂. During every ALD process, a Si(100) witness substrate was always included in the deposition chamber, and this witness was examined by variable angle spectroscopic ellipsometry (VASE) in addition to the TiO₂-coated 316L stainless steel samples.

Film stressing

3-point bending was performed using the Perkin Elmer dynamic mechanical analyzer DMA 8000. DMA stresses a sample by applying a sinusoidal, controlled deformation by the drive shaft. Although data was obtained, the purpose of using the DMA was to perform standardized stressing of the silica thin films on stainless steel. Each distance measurement was obtained in triplicate with calipers, and the average value used in the program. The length between each stage was about 10 mm, the thickness about 0.1 mm, and the width about 11 mm. The drive shaft was displaced by 0.25 mm at 1 Hz at room temperature. The samples were stressed four times for 5 minutes each, followed by twice for 10 minutes and twice for 15 minutes. Electrochemical evaluation was performed after each 5, 10, or 15 minute run in the DMA.

Characterization

Electrochemical. Electrochemical impedance spectroscopy (EIS) and cyclic voltammetry (CV) was performed using a Princeton Applied Research Model 2273 potentiostat in a three-electrode electrochemical cell. All potentials were measured and reported relative to a Ag/AgCl reference electrode with a saturated KCl solution. The working electrode was the 316L stainless steel sample in a

Teflon sample holder shown in Fig. 2.6 with 1.54 cm² exposed using a 7 mm diameter viton o-ring. The counter electrode used was a platinum wire. To make electrical contact with the SS sample or the working electrode, a copper plate was used. A 2 mM [Ru(NH₃)₆]Cl₃ in 0.1 M KCl aqueous solution was used to provide the electroactive species and the electrolyte for the cyclic voltammetry and impedance experiments, respectively. This enabled the impedance and cyclic voltammetry experiments to be performed sequentially, in the same apparatus, without changing the solution in the cell. Each data set contained six samples, and the reported values are the averages over the six samples. The electrochemical impedance spectroscopy experiments were performed at room temperature inside a Faraday cage. 50 points over the frequency range 55 kHz to 10 mHz were measured, equally spaced on a logarithmic scale, with an AC amplitude voltage of 10 mV. For the cyclic voltammetry experiments, the potential was scanned from 0.05 V to -0.4 V at scan rates of 250, 200, 150, 100 and 50 mV/s. The peak current was determined from the cyclic voltammogram using Princeton Applied Research PowerCV software. These values were then used to calculate the electroactive surface area from the slope of a plot of I_p versus scan rate^{1/2} graph. The calculated electroactive area was divided by the exposed area of the working electrode, and expressed as a percentage. The EIS data was modeled using ZSimpWin version 3.21 software. The equivalent circuit model can be found below.

The amount of the conducting stainless steel covered by insulating silica would decrease the measurable electroactive area of the metal substrate. The electroactive area of an electrode can be calculated from a plot of cyclic voltammogram peak current versus scan rate^{1/2} using the Randles-Sevcik equation given in Equation (1) below.⁽⁷³⁾ In this equation, I_p is the peak current of the reduction peak determined from a cyclic voltammogram. n is the number of electrons transferred during the electrochemical reaction, which is one in the instance of the Ru^{III}/Ru^{II} pair. C is the concentration of the analyte [Ru(NH₃)₆]Cl₃ involved in the electrochemical reaction (in mol/mL). D is the diffusion

coefficient of the $\text{Ru}(\text{NH}_3)_6^{3+}$ electroactive species in solution [$9.78 \times 10^{-6} \text{ cm}^2/\text{s}$], v is the scan rate and A is the surface area of the electrode (in cm^2).⁽⁸³⁾ The electroactive area is then determined from the slope of the peak current versus scan rate^{1/2} graph. The calculated electroactive area was divided by the area of the working electrode, and expressed as a percentage.⁽⁷³⁾

$$I_p = (2.69 \times 10^5) n^{3/2} C D^{1/2} A v^{1/2} \quad (1)$$

The impedance response of these systems can be modeled with the equivalent circuit illustrated in Fig. 2.18. In the equivalent circuit, a physical meaning can be attached to the components. R_s represents the resistance of the electrolyte solution, R_p represents the resistance to charge transfer across the electrolyte – electrode boundary, and Q represents a constant phase element whose nature is determined by its exponent, n . If $n = 0$, then Q behaves like a resistor, or if $n=1$ then Q behaves as a capacitor. Q can be used in the case of an imperfect capacitor, such as when the surface is rough, as is the case with our stainless steel samples (as can be seen above in Fig. 2.10).⁽⁸⁴⁾ The model fitting data is given in Table 2.3. χ^2 is a measure of how well the data fits, calculated by a least squares method.

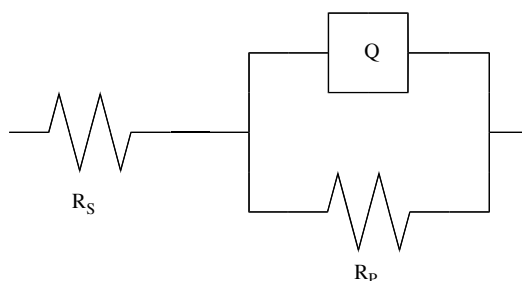


Figure 2.18. Equivalent circuit used to model EIS data. Reprinted with permission from (70). Copyright 2011 American Chemical Society.

R_p is the polarization resistance and is inversely proportional to the corrosion current and f_{\max} is the maximum frequency in Hertz. The higher the value of this resistance, the more resistant to corrosion a system will be. The

system capacity, a measure of the exposed surface area, can be calculated from equation 2.(73)

$$C = \frac{1}{2\pi f_{\max} R_p} \quad (2)$$

Table 2.3. Tabulated values of equivalent circuit model values. Adapted with permission from (70). Copyright 2011 American Chemical Society.

Sample	R_s (Ω)	Q ($\times 10^6$)	n	R_p ($M\Omega$)	χ^2
316L SS	182 (3)	7.12 (2.7)	0.905 (0.051)	3.20 (2.7)	8.60E-3 (1.1E-2)
PEG-silane	186 (2)	5.46 (1.1)	0.940 (0.015)	13.0 (4.7)	1.10E-3 (7.7E-4)
ALD SiO ₂	178 (1)	2.20 (0.6)	0.846 (0.019)	9.08 (6.0)	5.60E-3 (1.3E-3)
PEG-silane on ALD SiO ₂	182 (4)	1.10 (1.3)	0.917 (0.016)	19.2 (17)	6.48E-3 (4.1E-3)
Bissilane	186 (1)	6.67 (1.0)	0.932 (0.008)	7.44 (3.9)	1.42E-3 (9.9E-4)
Electrodeposited TEOS	185 (3)	9.67 (2.4)	0.826 (0.053)	2.82 (0.92)	1.78E-3 (2.1E-4)
Electrodeposited PEG-silane	191 (1)	8.89 (1.4)	0.898 (0.010)	3.40 (1.3)	4.47E-3 (6.9E-3)
100% TEOS(No Curing)	187 (1)	6.02 (1.3)	0.924 (0.033)	11.6 (7.8)	3.57E-3 (6.5E-3)
100% TEOS	186 (2)	5.49 (1.0)	0.911 (0.020)	10.2 (12)	1.72E-3 (2.1E-3)
1:1 TEOS:EtOH	185 (2)	5.21 (0.9)	0.912 (0.022)	6.81 (3.7)	2.01E-3 (1.5E-3)
1:1 TEOS:95% EtOH	187 (2)	4.49 (1.2)	0.917 (0.012)	25.3 (15)	9.07E-4 (6.3E-4)
1:1 TEOS:Acidic 95% EtOH	186 (2)	6.36 (0.8)	0.901 (0.014)	3.52 (2.0)	2.62E-3 (1.3E-3)

Film thickness measurements. Variable angle spectroscopic ellipsometry (VASE) experiments were performed on a J.A. Woollam VASE with HS-190 monochromator. Spectra were recorded every 7.5 nm in the range 300–1350 nm. Signals from 20 complete revolutions of the retarder were averaged for each data point, and spectra were recorded for three incidence angles (47°, 57° and 67°). Resulting Ψ and Δ data were fit with a simple model consisting of a Cauchy dielectric including Urbach absorption on a stainless steel substrate.

Additional Characterization. Stent and stainless steel surfaces were characterized by scanning Auger microscopy (SAM), X-ray photoelectron spectroscopy (XPS), scanning electron microscope (SEM), and atomic force microscopy (AFM). SAM, and XPS were performed under high-vacuum conditions ($<10^{-8}$ Torr). SAM (JAMP-9500F, JEOL) was performed at 15kV and 8 nA, for the accelerating voltage and emission current, respectively, and XPS (Kratos Analytical, Axis-Ultra) was performed using monochromatic Al KR with a photon energy of

1486.6 eV, in the Alberta Centre for Surface Engineering and Science (ACSES). The XPS instrument was calibrated on the basis of the C 1s peak. SEM was carried out using a Hitachi S-4880 FE-SEM operating at 5-15 kV. AFM was performed using a Nanoscope IV (Digital Instruments/Veeco) using commercial Si cantilevers. FTIR (Fourier transform infrared) spectra were collected on a Nicolet Nexus 760 spectrometer. Spectra of stainless steel samples were collected using a nitrogen purged sample chamber, a Harrick GATR accessory, a MCT/A detector, and 128 scans at 4 cm⁻¹ resolution.

ACKNOWLEDGEMENTS

CIHR and NSERC for funding of this project. NSERC and AIF for scholarship funding. Dr. Vincent Wright for his substantial work on this project including much experimental of the dip-coated samples and their electrochemical characterization. Dr. Brian Daly for help in the preliminary work. Dr. Kenneth Harris for his substantial work with ALD. Dr. Andrew Bonifas and Dr. David Rider for their help with the electrochemical analysis. Daniel Salomon for his help with SEM imaging. Bryan Szeto, Dr. Richard McCreery and the NINT cleanroom staff for access and aid in using the ALD. Dr. Anastasia Elias for the use of the DMA for the three point bending. ACSES for XPS and AES data and evaluation.

REFERENCES

1. Shahryari, A.; Azari, F.; Vali, H.; Omanovic, S., *Acta Biomater.* **2010**, *6* (2), 695-701.
2. Chuang, T.-W.; Chen, M.-H.; Lin, F.-H., *J. Biomed. Mater. Res. A* **2007**, *85A* (3), 722-730.
3. Indolfi, L.; Causa, F.; Netti, P. A., *J. Mater. Sci. - Mater. Med.* **2009**, *20* (7), 1541-1551.
4. Messer, R. L. W.; Mickalonis, J.; Lewis, J. B.; Omata, Y.; Davis, C. M.; Brown, Y.; Wataha1, J. C., *J. Biomed. Mater. Res. A* **2008**, *87A* (1), 229-235.

5. Ekvist, S.; Svedman, C.; Moeller, H.; Kehler, M.; Pripp, C. M.; Bjoerk, J.; Gruvberger, B.; Holmstroem, E.; Gustavsson, C. G.; Bruze, M., *Br. J. Dermatol.* **2007**, *157* (4), 730-738.
6. Lin, Q.; Ding, X.; Qiu, F.; Song, X.; Fu, G.; Ji, J., *Biomaterials* **2010**, *31* (14), 4017-4025.
7. Weng, Y.; Song, Q.; Zhou, Y.; Zhang, L.; Wang, J.; Chen, J.; Leng, Y.; Li, S.; Huang, N., *Biomaterials* **2011**, *32* (5), 1253-1263.
8. Atanasoska, L.; Gupta, P.; Deng, C.; Warner, R.; Larsen, S.; Thomson, J., *ECS Trans.* **2009**, *16* (38), 37-48.
9. Tammareddi, S.; Li, Q., *Adv. Mater. Res.* **2010**, *123-125* (Pt. 1, Multi-Functional Materials and Structures III), 315-318.
10. Stewart, H. J. S.; Guildford, A. L.; Lawrence-Watt, D. J.; Santin, M., *J. Biomed. Mater. Res. A* **2009**, *90A* (2), 465-471.
11. Thierry, B. M., Y.; Bilodeau, L.; Trepanier, C.; Tabrizian, M. , *Biomaterials* **2002**, *23* (14), 2997-3005.
12. Hale, P. T., Stephane; Horny, Paula; Lewis, Francois; Brack, Narelle; Van Riessen, Grant; Pigram, Paul; Mantovani, Diego *Langmuir* **2008**, *24* (15), 7897-7905.
13. Hanawa, T., *J. Artif. Organs* **2009**, *12* (2), 73-79.
14. Krishna, D. O.; Jeon, O. C.; Kim, K.; Byun, Y.; Moon, H. T., *J. Biomater. Sci., Polym. Ed.* **2010**, *21* (6-7), 789-802.
15. Touzin, M.; Chevallier, P.; Lewis, F.; Turgeon, S.; Holvoet, S.; Laroche, G.; Mantovani, D., *Surf. Coat. Technol.* **2008**, *202* (19), 4884-4891.
16. Ratner, B. D., *Biomaterials* **2007**, *28* (34), 5144-5147.
17. Mani, G.; Feldman, M. D.; Patel, D.; Agrawal, C. M., *Biomaterials* **2007**, *28* (9), 1689-1710.
18. Bayram, C.; Mizrak, A. K.; Akturk, S.; Kursaklioglu, H.; Iyisoy, A.; Ifran, A.; Denkbaz, E. B., *Biomed. Mater.* **2010**, *5* (5), 055007/1-055007/8.
19. Szabadits, P.; Dobranszky, J., *Mater. Sci. Forum* **2010**, *659* (Materials Science, Testing and Informatics V), 337-342.
20. Raman, A.; Gawalt, E. S., *Mater. Sci. Eng., C* **2010**, *30* (8), 1157-1161.

21. Lo, K. H.; Shek, C. H.; Lai, J. K. L., *Mater. Sci. Eng., R* **2009**, *65* (4-6), 39-104.
22. O'Brien, B.; Carroll, W., *Acta Biomaterialia* **2009**, *5* (4), 945-958.
23. Piedade, A. P.; Nunes, J.; Vieira, M. T., *Acta Biomater.* **2008**, *4* (4), 1073-1080.
24. Liu, C. L.; Chu, P. K.; Lin, G. Q.; Qi, M., *Surf. Coat. Technol.* **2006**, *201* (6), 2802-2806.
25. Gallino, E.; Massey, S.; Tatoulian, M.; Mantovani, D., *Surf. Coat. Technol.* **2010**, *205* (7), 2461-2468.
26. Okazaki, Y.; Gotoh, E., *Corros. Sci.* **2008**, *50*, 3429-3438.
27. Diaz, M.; Sevilla, P.; Galán, A. M.; Escolar, G.; Engel, E.; Gil, F. J., *J. Biomed. Mater. Res. B* **2008**, *87B* (2), 555-561.
28. Song, S.-J.; Kim, K. S.; Park, Y. J.; Jeong, M. H.; Ko, Y.-M.; Cho, D. L., *J. Mater. Chem.* **2009**, *19* (43), 8135-8141.
29. Zamiri, P.; Kuang, Y.; Sharma, U.; Ng, T. F.; Busold, R. H.; Rago, A. P.; Core, L. A.; Palasis, M., *Biomaterials* **2010**, *31* (31), 7847-7855.
30. Yin, M.; Yuan, Y.; Liu, C.; Wang, J., *Biomaterials* **2009**, *30* (14), 2764-2773.
31. Okner, R.; Oron, M.; Tal, N.; Nyska, A.; Kumar, N.; Mandler, D.; Domb, A. J., *J. Biomed. Mater. Res. A* **2008**, *88A* (2), 427-436.
32. Shaulov, Y.; Okner, R.; Levi, Y.; Tal, N.; Gutkin, V.; Mandler, D.; Domb, A. J., *ACS Appl. Mater. Interfaces* **2009**, *1* (11), 2519-2528.
33. Steigerwald, K.; Merl, S.; Kastrati, A.; Wieczorek, A.; Vorpahl, M.; Mannhold, R.; Vogeser, M.; Hausleiter, J.; Joner, M.; Schoemig, A.; Wessely, R., *Biomaterials* **2009**, *30* (4), 632-637.
34. Huang, Y.; Venkatraman, S. S.; Boey, F. Y. C.; Lahti, E. M.; Umashankar, P. R.; Mohanty, M.; Arumugam, S.; Khanolkar, L.; Vaishnav, S., *Biomaterials* **2010**, *31* (15), 4382-4391.
35. Duan, L. J.; Kim, M. J.; Jung, J. H.; Chung, D. J.; Kim, J., *Macromol. Res.* **2010**, *18* (8), 806-811.

36. Mani, G.; Macias, C. E.; Feldman, M. D.; Marton, D.; Oh, S.-H.; Mauli Agrawal, C., *Biomaterials* **2010**, *31* (20), 5372-5384.
37. Nelea, V.; Holvoet, S.; Turgeon, S.; Mantovani, D., *J. Phys. D: Appl. Phys.* **2009**, *42* (22), 225208/1-225208/9.
38. Halwani, D. O.; Anderson, P. G.; Brott, B. C.; Anayiotos, A. S.; Lemons, J. E., *J. Biomed. Mater. Res. B* **2010**, *95B* (1), 225-238.
39. Mikhalovska, L.; Chorna, N.; Lazarenko, O.; Haworth, P.; Sudre, A.; Mikhalovsky, S., *J. Biomed. Mater. Res. B* **2011**, *96B* (2), 333-341.
40. Levy, Y.; Tal, N.; Tzemach, G.; Weinberger, J.; Domb, A. J.; Mandler, D., *J. Biomed. Mater. Res. B* **2009**, *91B* (2), 819-830.
41. Levy, Y.; Mandler, D.; Weinberger, J.; Domb, A. J., *J. Biomed. Mater. Res. B* **2009**, *91B* (1), 441-451.
42. Zhang, F.; Kang, E. T.; Neoh, K. G.; Wang, P.; Tan, K. L., *Biomaterials* **2001**, *22* (12), 1541-1548.
43. Papra, A.; Gadegaard, N.; Larsen, N., *Langmuir* **2001**, *17* (5), 1457-1460.
44. Norrman, K.; Papra, A.; Kamounah, F.; Gadegaard, N.; Larsen, N., *J. Mass Spectrom.* **2002**, *37* (7), 699-708.
45. Okner, R.; Domb, A. J.; Mandler, D., *New J. Chem.* **2009**, *33* (7), 1596-1604.
46. Elise, C. P.; Gavin, S. W.; Colin, A. S.; David, F.; David, G., *J. Biomed. Mater. Res. A* **2009**, *90A* (4), 947-958.
47. Lewis, A. L.; Furze, J. D.; Small, S.; Robertson, J. D.; Higgins, B. J.; Taylor, S.; Ricci, D. R., *J. Biomed. Mater. Res.* **2002**, *63* (6), 699-705.
48. Ooij, W. v.; Child, T., *Chem. Tech.* **1998**, *28* (2), 26-37.
49. Meth, S.; Sukenik, C. N., *Thin Solid Films* **2003**, *425* (1-2), 49-58.
50. Wang, D.; Bierwagen, G., *Prog. Org. Coat.* **2009**, *64* (4), 327-338.
51. Perez, F.; Hierro, M.; Carpintero, M.; Gomez, C.; Pedraza, F., *Surf. Coat. Technol.* **2002**, *160* (1), 87-92.
52. Garcia, C.; Cere, S.; Duran, A., *J. Non-Cryst. Solids* **2004**, *348* (2004), 218-224.

53. Ballare, J.; Jiminez-Pique, E.; Anglada, M.; Pellice, S.; Cavalieri, A., *Surf. Coat. Technol.* **2009**, *203* (20-21), 3325-3331.
54. Vasconcelos, D.; Carvalho, J.; Mantel, M.; Vasconcelos, W., *J. Non-Cryst. Solids* **2000**, *273* (1-3), 135-139.
55. van Ooij, W. J.; Zhu, D.; Stacy, M.; Seth, A.; Mugada, T.; Gandhi, J.; Puomi, P., *Tsinghua Sci. Technol.* **2005**, *10* (6), 639-664.
56. Ichinose, I.; Senzu, H.; Kunitake, T., *Chem. Lett.* **1996**, *25* (10), 831-832.
57. Gupta, R.; Kumar, A., *Biomed. Mater.* **2008**, *3* (3), 034005.
58. Zheludkevich, *J. Mater. Chem.* **2005**, *15*, 5099-5111.
59. Castro, Y.; Duran, A.; Damborenea, J.; Conde, A., *Electrochim. Acta* **2008**, *53* (20), 6008-6017.
60. Gallardo, J.; Duran, A.; Damborenea, J., *Corros. Sci.* **2004**, *46* (4), 795-806.
61. Gurappa, I., *Surf. Coat. Technol.* **2002**, *161* (1), 70-78.
62. Monsma, D.; Becker, J., *ECS Trans.* **2007**, *11* (7), 39-44.
63. Fischer, H.; Wirtz, D.; Weber, M.; Neuss, M.; Niethard, F.; Marx, R., *J. Biomed. Mater. Res.* **2001**, *57* (3), 413-418.
64. Wang, Z.; Leng, Y.; Huang, N.; Zhu, M., *Key Eng. Mater.* **2007**, *353-358* (2007), 2127-2130.
65. Matero, R.; Ritala, M.; Leskela, M.; Salo, T.; Aromaa, J.; Forsen, O., *J. Phys. IV* **1999**, *09* (PR8), 493-499.
66. Yasseri, A.; Kobayashi, N.; Kamins, T., *Appl. Phys. A* **2006**, *84* (1), 1-5.
67. Checmanowski, J.; Szczygiel, B., *Corros. Sci.* **2008**, *50* (12), 3581-3589.
68. Guglielmi, M., *J. Sol-Gel Sci. Technol.* **1997**, *8* (1-3), 443-449.
69. Hugot, F.; Abgrall, E., *Mec. Ind.* **2008**, *9* (3), 177-182.
70. Slaney, A.; Wright, V.; Meloncelli, P.; Harris, K.; West, L.; Lowary, T.; Buriak, J., *ACS Appl. Mater. Interfaces* **2011**, *3* (5), 1601-1612.
71. West, L.; Lowary, T.; Buriak, J.; Daly, B.; Mylvaganam, J.; Meloncelli, P.; Wright, V.; Cooper, A. Methods and Systems for Inducing Immunologic Tolerance to Non-Self Antigens. PCT Patent (PCT/CA2009/001814), December, 2009.

72. van Ooij, W. J.; Zhu, D.; Palanivel, V.; Lamar, J. A.; Stacy, M., *Silicon Chem.* **2006**, *3*, 11-30.
73. Bard, A. J.; Faulkner, L. R., *Electrochemical Methods Fundamentals and Applications*. 2nd ed.; John Wiley & Sons: New York, 2001; p 833.
74. Hryniewicz, T.; Rokosz, K.; Filippi, M., *Materials* **2009**, *2* (1), 129-145.
75. Baccaria, A.; Castello, G.; Poggi, G., *Br. Corros. J.* **1995**, *30* (4), 283-287.
76. Lim, A.; Atrons, A., *Appl. Phys. A* **1990**, *51* (5), 411-418.
77. Al-Suhybani, A., *Surf. Coat. Technol.* **1988**, *34* (4), 463-470.
78. Hashimoto, M.; Miyajima, S.; Ito, W.; Ito, S.; Murata, T., *Surf. Coat. Technol.* **1988**, *36* (3-4), 837-845.
79. Haanappel, V.; Corbach, H. v.; Hofman, R.; Morssinkhof, R.; Fransen, T.; Gellings, P., *High Temp. Mater. and Processes* **1996**, *15* (4), 245-262.
80. Jussila, P.; Ali-Löytty, H.; Lahtonen, K.; Mirsimäki, M.; Valden, M., *Surf. Interface Anal.* **2010**, *42* (3), 157-164.
81. Chuang, T.-W.; Lin, D.-T.; Lin, F.-H., *J. Biomed. Mater. Res. A* **2007**, *86A* (3), 648-661.
82. Bertrand, N.; Drévillon, B.; Gheorghiu, A.; Sénémaud, C.; Martinu, L.; Klemberg-Sapieha, J. E., *J. Vac. Sci. Technol., A* **1998**, *16* (1), 6-12.
83. Csóka, B.; Nagy, G., *J. Biochem. Bioph. Methods* **2004**, *61* (1-2), 57-67.
84. Hsu, C. H.; Mansfeld, F., *Corrosion* **2001**, *57* (9), 747-748.

CHAPTER 3 – FUNCTIONALIZATION OF SILICA-COATED STAINLESS STEEL

INTRODUCTION

Hybrid materials comprising of inorganic, polymeric, organic and/or biological components are well studied for the combined properties they display from their individual counterparts.(1) By combining these materials together, desirable properties of each material can be integrated.(2-4) For example, the favorable characteristics of stainless steel such as its ductility and affordability can be combined with the resistance of PEGylated surfaces to prevent protein adsorption.(5,6) The properties of the hybrid materials can also be tailored for a variety of applications.(1-3,7)

For a number of biomedical implant applications, materials with effective biomolecule attachment can be essential.(8-11) One type of biomolecule, carbohydrates, can be found on cell surfaces and play an important role in a variety of biological processes.(12-15) As such, glycosylation of surfaces can open the opportunity for fabricating biomimetic surfaces.(12,16) Biomimetic surface performance can be greatly impacted by the density of biomolecules.(17) In order to replicate a cell surface, a spacer molecule can be used to achieve a suitable spacing of biomolecules.(18) PEG (polyethylene glycol) may be ideal for spacing of biomolecules as well as preventing nonspecific protein binding for biomimetic surfaces.(12,19) This depiction of biomolecule presentation on tissues and that functionalized on stainless steel surfaces is depicted in Fig. 3.1.

Effective attachment of these carbohydrates can be critical in biomedical applications.(14,17) Many different methods for immobilizing desired molecules have been developed, but they can broadly be divided into noncovalent and covalent means.(12,17) Noncovalent attachment involves adsorption of molecules by means of intermolecular forces such as hydrogen or ionic bonding.(12,17)

However, these weaker bonds can allow dissociation of the desired molecules.(7,12,17)

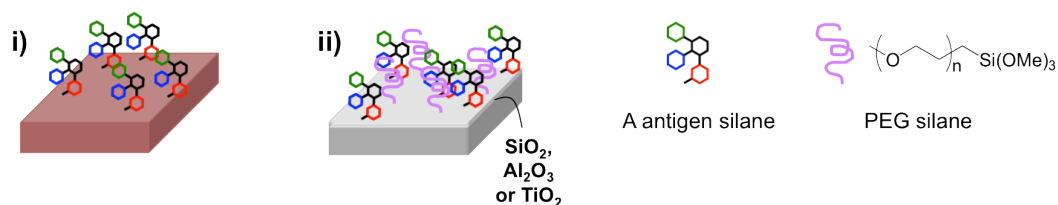


Figure 3.1. i) A schematic of A-type antigen biomolecule presentation on heart tissue surfaces. ii) A schematic of the replication of natural A-type antigen biomolecule presentation on stainless steel surfaces.

Covalent attachment of carbohydrates is a more popular method of immobilization.(12,17) The reaction of thiols on gold and silver surfaces, for example, shown in Fig. 3.2i, has been extensively examined. The biggest drawback is the susceptibility of Au-S bonds to oxidation.(13,17) Alcohols have also proven useful in creating monolayers on hydroxylated surfaces such as silica, shown in Fig. 3.2ii. However, the ethers produced are prone to hydrolysis.(20) Of particular interest, self-assembled monolayers (SAMs) on stainless steel have been shown to form with thiols, carboxylic acids, and phosphonic acids.(21-25) This functionalization of stainless steel is shown in Fig. 3.2iii. Again, the thiol is prone to oxidation, and phosphates tend to bind more strongly than carboxylic acids.(14,21) However, silane functionalization of stainless steel produces even more stable SAMs.(21)

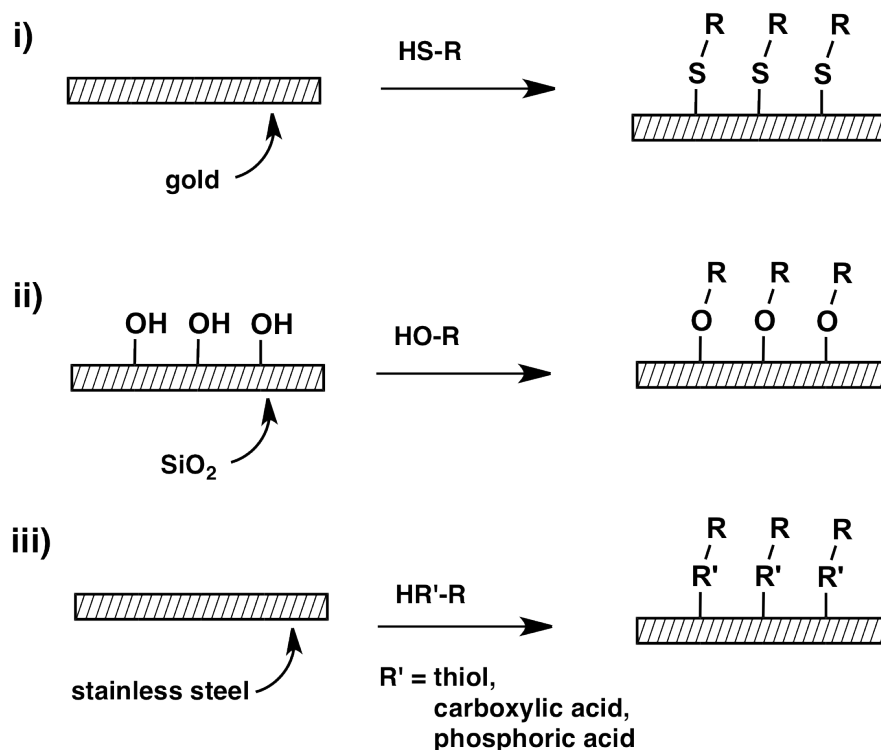


Figure 3.2. Immobilization of carbohydrates have been successful using i) thiol derivatives on gold surfaces,(13) ii) alcohol derivatives on hydroxyl-terminated silica surfaces,(20) and iii) thiol, carboxylic acid or phosphoric acid derivatives on stainless steel surfaces.(21,23,24)

Different methods have been developed to attach silane monolayers to surfaces. Some methods involve linkers to connect the carbohydrate to a substrate.(12,26) For example, aminopropyl- or mercaptopropyltrimethoxysilane can first form a functional layer on the substrate, followed by subsequent reaction to immobilize the desired molecules, demonstrated in Fig. 3.3i.(3,12,27-32) Amine and thiol functional groups can react with aldehydes and alkenes respectively to graft carbohydrates as depicted in Fig. 3.3ii.(6,7,12,14) Alternatively, silanes can be directly reacted onto a substrate, depicted in Fig. 3.3iii.(33) Silane derivatives of carbohydrates and PEG can be used to graft them to substrates and mixed silane monolayers have been successfully deposited from mixed silane solutions.(30,33-35)

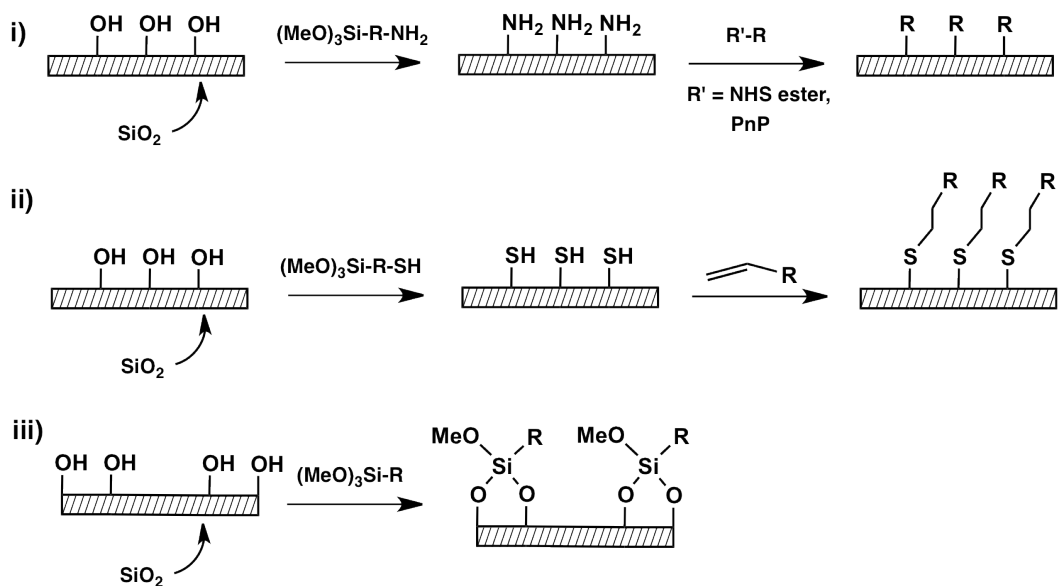


Figure 3.3. Silane functionalization of stainless steel with desired molecules have been successful by i) using silane derivatives of amines to subsequently react with amine-reactive derivatives of desired molecules,(12,27,29,32) ii) using silane derivatives of thiols to subsequently react with alkene derivatives of desired molecules,(12,28,29) and iii) alkoxysilane derivatives of desired molecules.(36,37)

To attach silane monolayers, either trichloro- or trimethoxysilane moieties can be used.(3,5) The chloro- and methoxy- groups are hydrolysable, and a fourth group is attached through a high stability Si-C bond.(36-38) The hydrolysable groups form Si-O-Si and Si-O-metal bonds to form a covalent network to each other and to the substrate.(37) However, the production of HCl from trichlorosilanes can cause undesirable side reactions such as corrosion of stainless steel.(21) Reactive groups, such as hydroxyl groups, on substrates are important for functionalization with organosilanes, and stainless steel and silica have both shown promise in this area.(20,39)

Here, silane derivatives of both carbohydrates and PEG were used to functionalize onto both stainless steel and silica substrates. PEG acts to dilute the more expensive synthetic carbohydrates and to prevent non-specific protein binding. The carbohydrate silanes used include monosaccharides (MSs) as well as a trisaccharide or tetrasaccharide (collectively TS) ABO histo-blood group antigens.

These substrates were evaluated for the successful attachment of the silanes as well as their stability and the biological availability of the carbohydrates. Much of this work has been published or patented.(40-42)

RESULTS & DISCUSSION

Stainless steel coated with silica obtained by ALD was determined to be the optimal coating technique in our earlier work.(40) As such, silica coated stainless steel, as well as stainless steel and additional silica surfaces were used as surfaces for subsequent functionalization for comparison and characterization. These surfaces were then functionalized as indicated in Fig. 3.4 with the A antigen, a tetrasaccharide (TS), as depicted. The silanes of particular interest for our devices are shown in Fig. 3.5. Although six different subtypes of each antigens exist and have been synthesized for our use, the type II antigen of each TS is depicted in Fig. 3.5 for simplicity. While the functionalization of TSs on stents is the goal of this work, preliminary studies were performed using monosaccharides (MS), which are much easier to synthesize, and are therefore much less expensive than TSs.

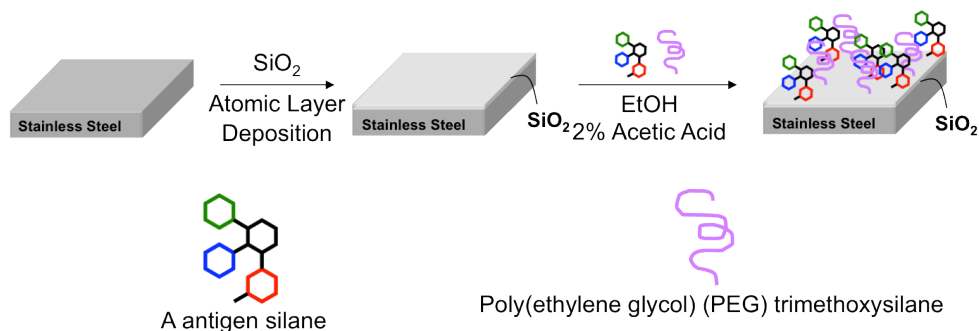
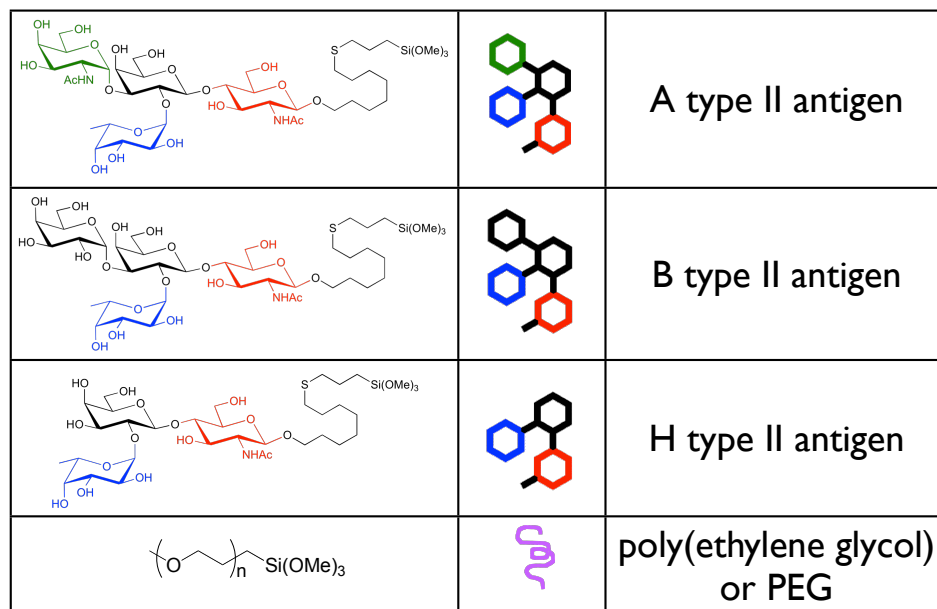


Figure 3.4. Stainless steel coupons were first coated with silica by ALD, followed by functionalization with PEG and monosaccharide (MS), trisaccharide or tetrasaccharide (TS) silanes. Here, the A antigen, a TS, is depicted in the functionalization. Adapted with permission from (40). Copyright 2011 American Chemical Society.



Galactose
 Fucose
 N-acetyl glucosamine
 N-acetyl galactosamine

Figure 3.5. The silane derivatives of trisaccharide, tetrasaccharide (TS) and PEG used to functionalize stainless steel.

A general scheme of the functionalization with the MS N-acetyl glucosamine (GlcNAc) and poly(ethylene glycol) (PEG) trimethoxysilane can be seen in Fig. 3.6. First, the synthetic GlcNAc derivative reacts with mercaptopropyltrimethoxysilane (MPTMS) to produce a GlcNAc silane through thiol-ene coupling. Then, the GlcNAc and PEG silanes were used to functionalize the stainless steel surface using a sol-gel dip-coating procedure. As the stainless steel substrate, silica ALD coated stainless steel will be used to provide the sufficient concentration of hydroxyl groups on the surface in order to functionalize with trimethoxysilanes. To characterize the functionalization of these trimethoxysilanes on silica substrates, porous silicon was used. Porous silicon was chosen because silicon is IR transparent, and porous silicon generates increased surface area while providing a silica substrate when oxidized.

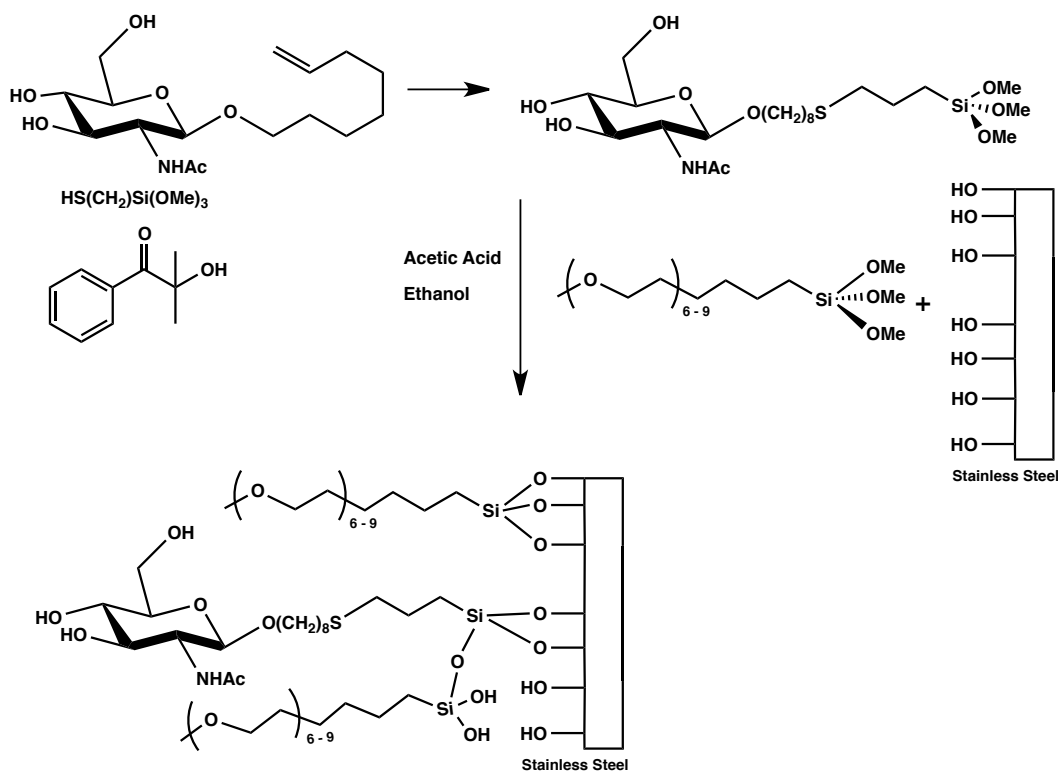


Figure 3.6. The reaction of the 2-*N*-acetamido-2-deoxy-β-D-glucopyranoside (GlcNAc) derivative with mercaptopropyltrimethoxysilane using 2-hydroxy-2-methylpropiophenone as a photoinitiator forms the GlcNAc silane under UV illumination. Stainless steel (SS) surface is subsequently functionalized via a dip-coating sol of a mixture of PEG and the GlcNAc silanes in a predetermined ratio. Adapted with permission from (40). Copyright 2011 American Chemical Society.

The porous silicon surface was functionalized by dip coating the sample the same acid-catalyzed sol-gel of the desired silanes as used for the silica-coated stainless steel samples. In this sol-gel reaction, the methoxy groups of the silane become hydrolyzed to silanols that can then hydrogen bond to the hydroxylated surface. As such, the concentration of hydroxyls on the surface is critical in the covalent attachment of the silanes. To enhance the hydroxyl concentration on their surfaces, the porous silicon samples were treated with piranha. These hydroxyl groups also allow the condensation with the physisorbed silanol groups of the silanes. Upon removal from the silane functionalization solution, the samples were cured, to drive the condensation reaction that forms the covalent silicon-oxygen-silicon bonds between the silanes and the oxidized porous silicon.

As expected, the mixture of silanes in the sol-gel solution results in proportional surface functionalization as determined by FTIR, as shown in Fig. 3.7. FTIR is an excellent technique to identify characteristic functional groups of the carbohydrates.⁽¹⁵⁾ The carbonyl peak in FTIR decreases with the decreasing concentration of GlcNAc on the surface. GlcNAc and acetic acid (the catalyst) are the only two sources of carbonyl used in the reaction. The near absence of carbonyl peak in the 100% PEG indicates that little contribution is derived from the acetic acid since all the functionalizations were performed in the same manner with an acetic acid catalyst. The porous silicon samples were rinsed thoroughly with methanol, an excellent solvent for GlcNAc and even after sonication of 100% GlcNAc functionalized porous silicon samples, equivalent transmission FTIR spectra were obtained. Therefore, it is unlikely that these peaks are due to physisorption of GlcNAc. Additionally, from Fig. 3.7, the ether signal evidently increases with increasing concentration of PEG silane. As there are more ether functionalities in the PEG than GlcNAc, this agrees with the silane ratios in solution.

For our purposes, we would like to replicate the antigen presentation on a cell surface. Just as a cell's surface does not present a continuum of a single antigen, spacing between antigens is necessary for many biomedical applications. PEG is used to prevent nonspecific protein binding, but also to act as a spacer molecule to achieve an appropriate antigen density to mimic that found on tissue surfaces.⁽¹⁸⁾ This spacing could lead to appropriate spacing of the antigen for successful antibody or lectin binding and a biomimetic surface. In addition, the PEG dilutes the more expensive saccharides.

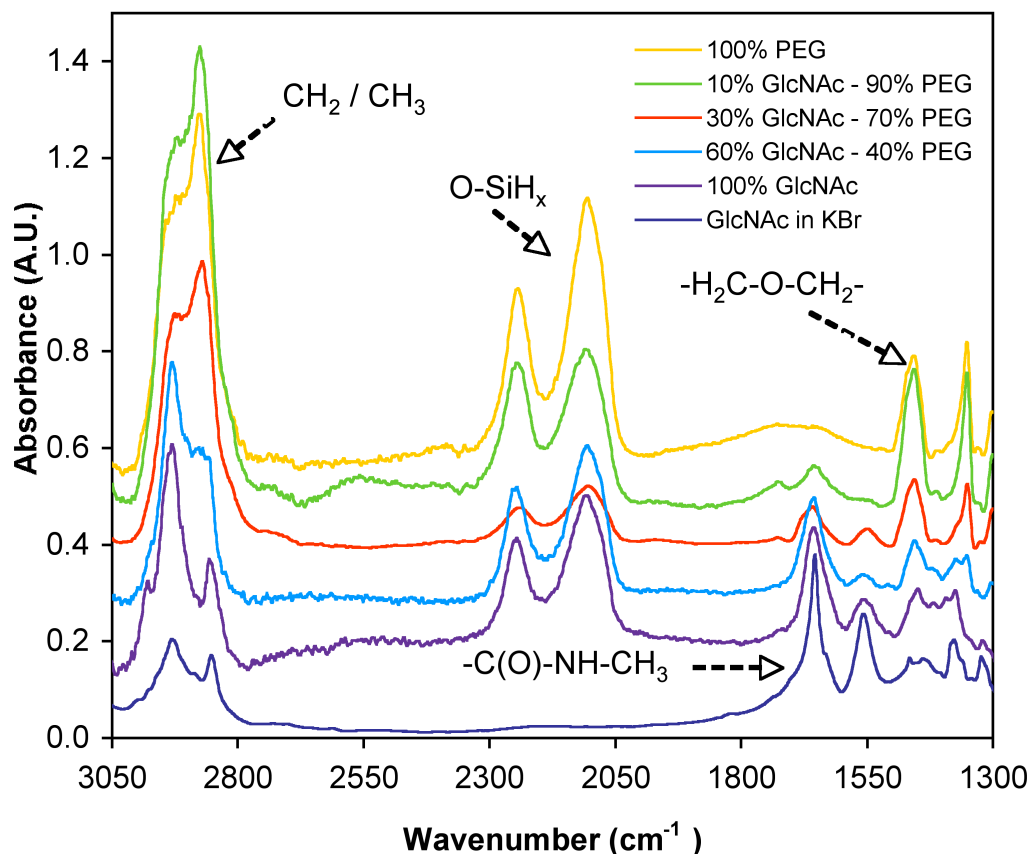


Figure 3.7. Transmission FTIR of a series of GlcNAc and PEG functionalized porous silicon surfaces, illustrating that the sol-gel deposition solution composition correlates with that deposited on the surface. Reprinted with permission from (40). Copyright 2011 American Chemical Society.

A second MS, galactose (Gal), was also used as a biologically significant molecule for functionalization of substrates. A schematic of this functionalization can be seen in Fig. 3.8. The presence of nitrogen in GlcNAc and its absence in both Gal and PEG gives a good handle for elemental analysis. Additionally, both of the MSs contain sulfur, which the PEG silane does not and the proportion of oxygen in the MSs is slightly less than is present in PEG. For the purpose of elemental analysis, low resolution XPS was performed on samples of varying concentrations of GlcNAc or Gal and PEG, as shown in Fig. 3.9. XPS has previously been used to identify functionalization of surfaces.(16,26,43,44) The varying concentrations of silanes used for the functionalization of stainless steel and silica-coated stainless steel (SS) are listed in Table 3.1.

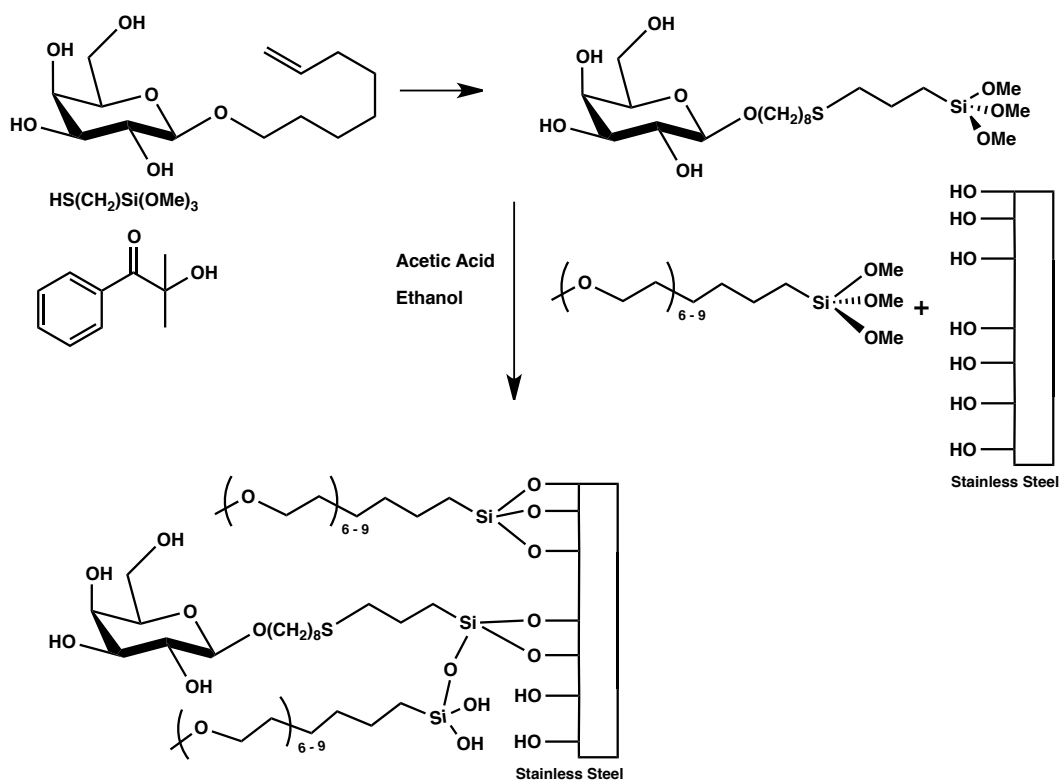


Figure 3.8. The reaction of the galactose (Gal) derivative with mercaptopropyltrimethoxysilane using 2-hydroxy-2-methylpropiophenone as a photoinitiator forms the Gal silane under UV illumination. Stainless steel (SS) surface is subsequently functionalized via a dip-coating sol of a mixture of PEG silane and the Gal silanes in a predetermined ratio. Adapted with permission from (40). Copyright 2011 American Chemical Society.

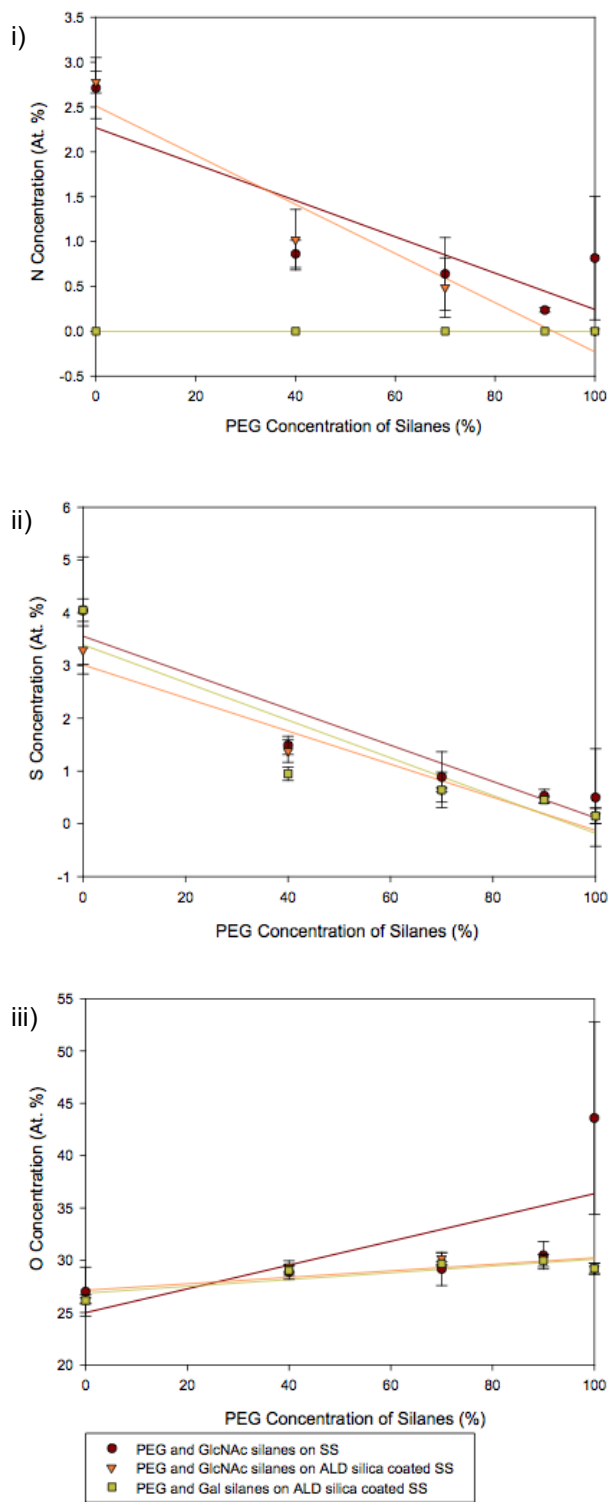


Figure 3.9. Atomic % of i) nitrogen, ii) sulfur and iii) oxygen determined via low resolution XPS of direct silanization of 316L stainless steel, and on 5 nm ALD silica coated 316L stainless steel with mixtures of GlcNAc or Gal and PEG. Adapted with permission from (40). Copyright 2011 American Chemical Society.

Table 3.1. Silane concentration used to functionalize stainless steel (SS). Adapted with permission from (40). Copyright 2011 American Chemical Society.

Uncoated SS	ALD silica-coated SS	ALD silica-coated SS
100% PEG	100% PEG	100% PEG
60% PEG:40% GlcNAc	60% PEG:40% GlcNAc	60% PEG:40% Gal
30% PEG:70% GlcNAc	30% PEG:70% GlcNAc	30% PEG:70% Gal
0% PEG: 100% GlcNAc	0% PEG: 100% GlcNAc	0% PEG: 100% Gal

From Fig. 3.9, it is apparent that there is a decrease in both the nitrogen and sulphur content increases as the ratio of GlcNAc to PEG increases. Also, the sulfur content increases as the ratio of Gal to PEG increases and the nitrogen content remains low across these Gal to PEG ratios. These are the expected results since the sulfur content is derived from the GlcNAc and Gal silanes used to functionalize the surface and the nitrogen content is derived solely from the GlcNAc. Additionally, the oxygen content increases as the ratio of PEG to GlcNAc or Gal silanes used increases as the PEG silane used has a slightly higher oxygen content than GlcNAc or Gal. This confirms that there is a general trend in correlation between the ratio of silanes used in the functionalization solution and the silanes attached to the surface. These trends are evident in both the silane functionalizations on clean stainless steel and on stainless steel coated with silica by ALD, and are fairly predictable within statistical deviations, as depicted with the trendlines. No distinct difference between the silane functionalized clean stainless steel and stainless steel coated with silica by ALD could be determined from this XPS data. The deviation in these plots from linearity are most likely due to packing of the molecules since PEG is a long, flexible chain that will be in constant motion, and will take up more room than the other silanes.

The results from both FTIR and XPS indicate that the functionalization of ALD silica-coated stainless steel is successful and that the mixture in solution roughly translates to the functionalization on the surface. However, this rough translation gives no indication of the biological availability of the GlcNAc or Gal on these surfaces. In order to assess the biological availability of these MSs, an enzyme-

linked lectin assay (ELLA) was used.(40) The ELLAs used are outlined in Fig. 3.10.

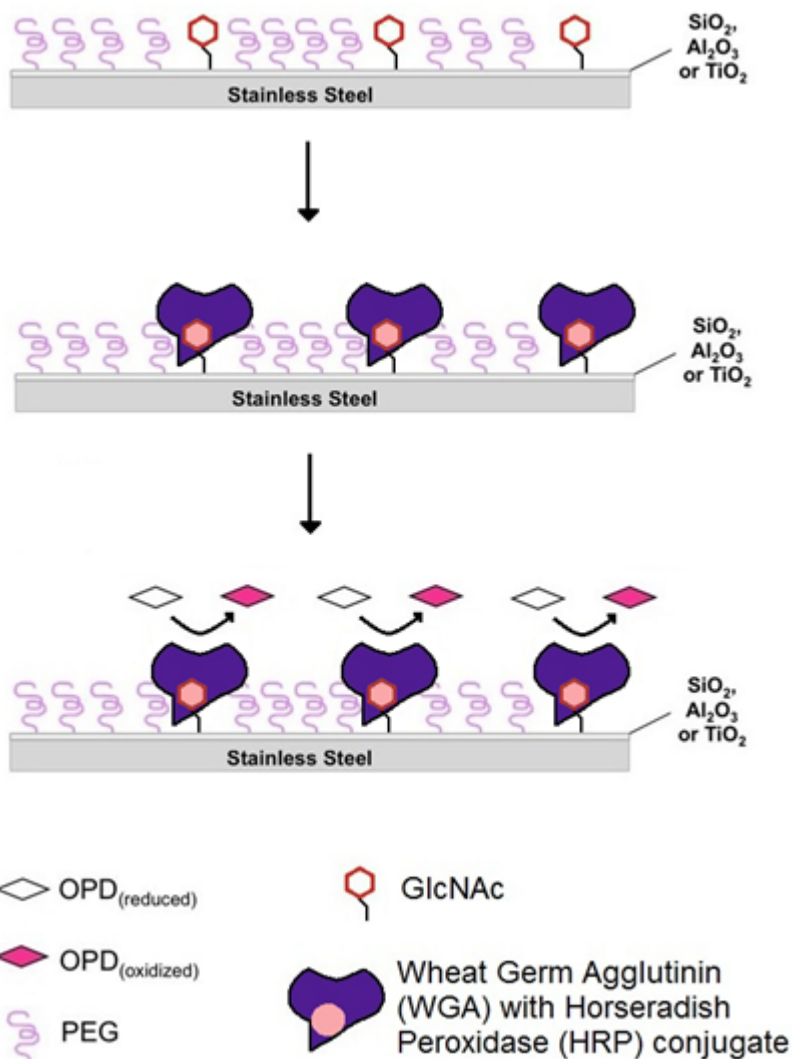


Figure 3.10. The detection of monosaccharides using an enzyme-linked lectin assay (ELLA). Adapted with permission from (40). Copyright 2011 American Chemical Society.

In the case of GlcNAc, the lectin wheat germ agglutinin (WGA) with a horseradish peroxidase conjugate was used. Peanut agglutinin (PNA) with a horseradish peroxidase conjugate, on the other hand, was used to detect GlcNAc. Using the functionalizations outlined in Table 3.1, each sample was incubated with either WGA or PNA and the excess lectin was washed off. The HRP

conjugate was detected using *o*-phenylenediamine (OPD) as an indicator. The oxidation of OPD is performed by HRP, which causes it to change to a red colour. This red colour of the oxidized OPD was then detected by UV/Vis absorbance spectroscopy, and the absorbance measured at 450 nm.

From Fig. 3.11, it is evident that WGA effectively detects GlcNAc and ineffectively detects Gal on the ALD silica-coated stainless steel. The GlcNAc is effectively detected by WGA even at lower concentrations of GlcNAc. Interestingly, the detection of GlcNAc on uncoated stainless steel is not as effective. The uncoated stainless steel was used as a control, just as the 100% PEG were prepared as controls. However, the absorbance of 100% PEG on uncoated stainless steel is high in comparison to that of 100% PEG on ALD silica-coated stainless steel. The absorbance of 100% PEG on uncoated stainless steel is, in fact, similar in intensity to the absorbance of the samples functionalized with GlcNAc silane and highlights the utility of the ALD silica coating on the stainless steel. The increased absorbance from the uncoated stainless steel samples may indicate insufficient functionalization with PEG silane, allowing for nonspecific binding of the WGA.

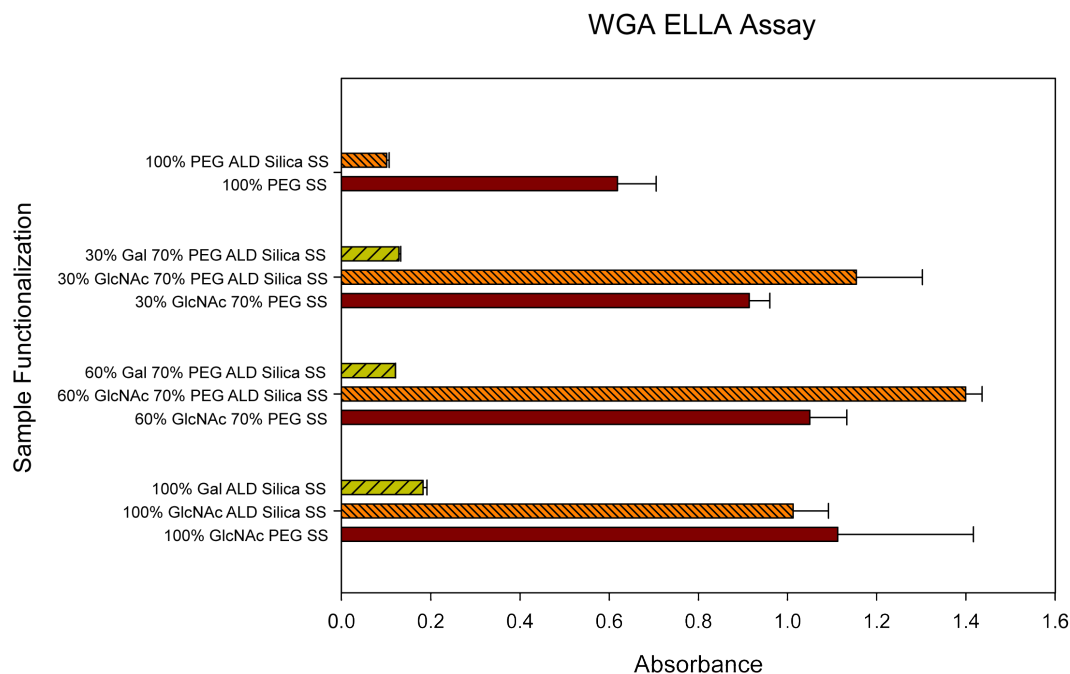


Figure 3.11. Wheat germ agglutinin (WGA) ELLA specific for GlcNAc. Reprinted with permission from (40). Copyright 2011 American Chemical Society.

The peanut agglutinin (PNA) ELLA, on the other hand, showed low absorbance for 100% PEG samples on both uncoated and ALD silica-coated stainless steel. This indicates little non-specific binding of PNA to either PEG or uncoated stainless steel. In contrast to the WGA ELLA, which appears to detect GlcNAc no matter the concentration (Fig. 3.11), the PNA ELLA detection evidently depends on the concentration of Gal (Fig. 3.12). PNA has fewer binding sites than WGA, giving rise to a lower affinity for Gal than WGA has for GlcNAc.(40) This lower affinity of PNA is supported by literature and explains why in this case, 30% Gal is inadequate for detection by PNA ELLA.(45,46) In contrast, the WGA ELLA detection peaks and levels off above 30% GlcNAc. This indicates that biological molecule density must be carefully selected. The density must be high enough for efficient detection and sufficient biological availability, however low enough to reduce the cost of prepared substrates – of particular importance as the samples prepared move from MSs to trisaccharide and tetrasaccharides (collectively TSs).

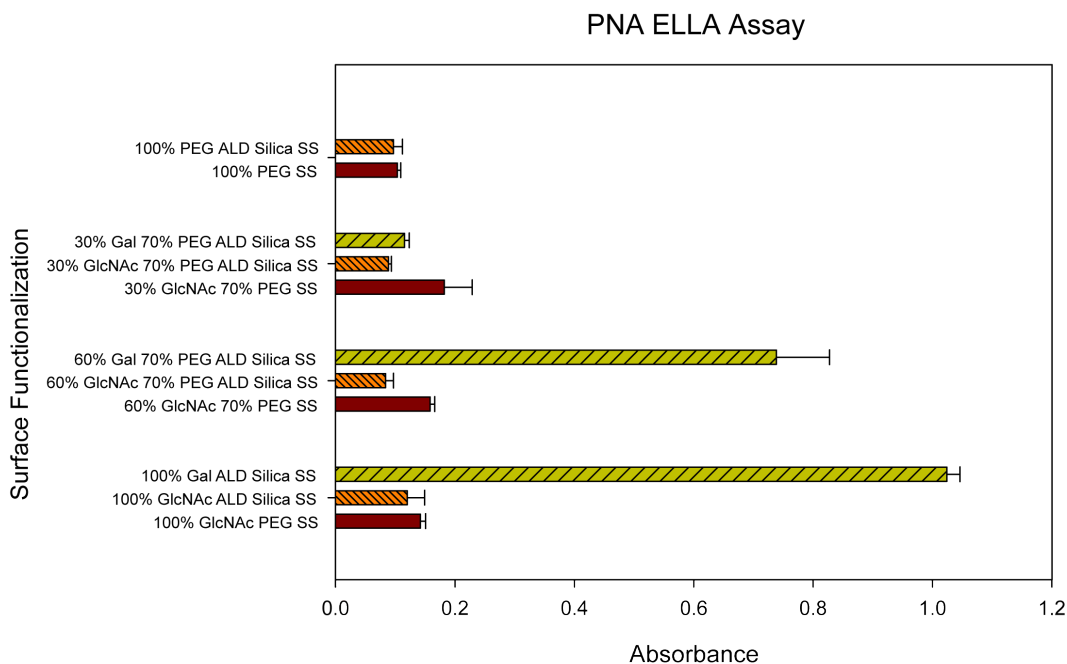


Figure 3.12. Peanut agglutinin (PNA) ELLA specific for Gal. Reprinted with permission from (40). Copyright 2011 American Chemical Society.

Six different types or isomers of each blood type antigen exist, which adds up to 18 ABO blood type antigens, and have been synthesized. Of the antigen types, the H type antigen is the antigen presented on O blood type cells. These synthetic TSs, along with PEG silane, were used to functionalize the silica ALD coated stainless steel, previously determined to be the best surfaces for this purpose. In order to characterize this functionalization, silica coated stainless steel was functionalized with varying ratios of A type II antigen to PEG silanes. This type of functionalization is depicted with the A type I antigen in Fig. 3.13. Varying ratios of A type II antigen to PEG were used to functionalize the silica ALD coated stainless steel and these samples were characterized by low resolution XPS (shown in Fig. 3.14). Similar to the results obtained by XPS for the MSs, both the nitrogen and sulfur concentration detected on the surfaces decrease as the concentration of A type II decreases. The A type II antigens contain both sulfur and nitrogen, whereas the PEG does not, therefore the XPS results were as expected.

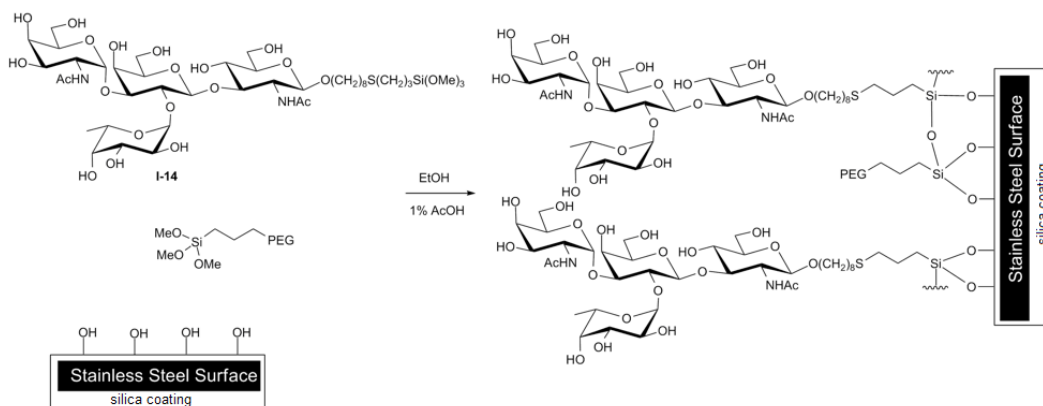


Figure 3.13. Functionalization of silica-coated stainless steel surface with A type I and PEG silanes.

To characterize the biological availability of antigen, the A antigens were detected using an enzyme-linked immunosorbent assay (ELISA) as depicted in Fig. 3.15. Similar to the ELLAs used to characterize the MS-functionalized substrates, ALD silica coated stainless steel functionalized with PEG and A type II antigen silanes was treated with a mouse anti-A antibody which binds to the A type antigens. Subsequently, these substrates were treated with a secondary goat anti-mouse antibody (which binds to the mouse antibody) with a horseradish peroxidase (HRP) conjugate. Just as in the ELLAs used to detect the MSs, an OPD indicator was used to detect the HRP conjugate. OPD is oxidized by HRP, which causes it to change to a red colour. The oxidized OPD can then be detected by UV/Vis spectrometry.

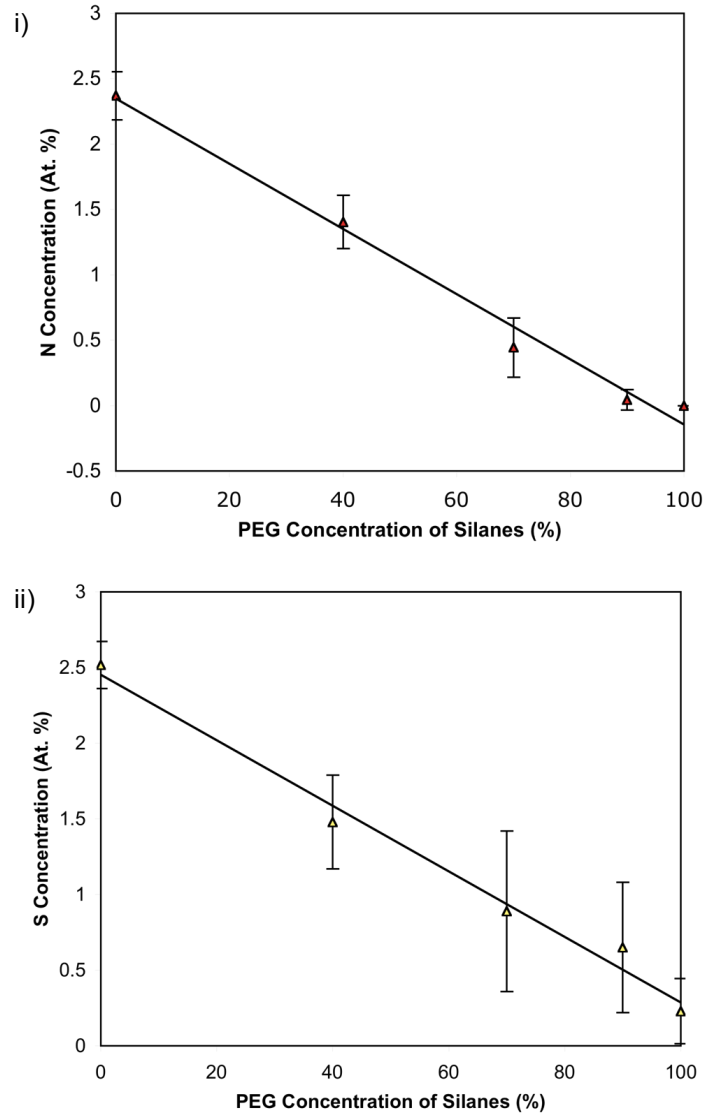


Figure 3.14. Detection of A antigens by i) nitrogen and ii) sulfur concentration of stainless steel coupons coated with silica by ALD and functionalized with mixtures of A antigen and PEG silanes as characterized by XPS.

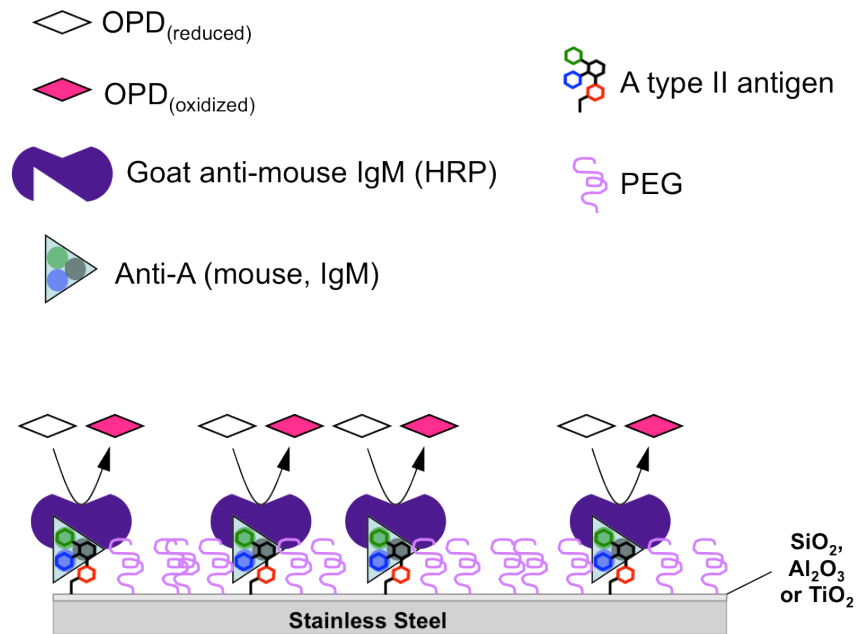


Figure 3.15. The ELISA assay used to detect A antigens on stainless steel coated by ALD.

A distinct increase in absorbance is observed between samples functionalized with 100% PEG and even with a low concentration of 10% A type II antigen shown in black in Fig. 3.16. In order to assess the stability of the A type II antigens, a couple of sample sets were incubated in blood plasma. One sample set with different ratios of PEG to A type II antigen (each in triplicate) was incubated each in A blood plasma and in O blood plasma. This incubation was performed for a month at 37°C under agitation, with replacement of the blood plasma every 2-3 days. These incubated samples were also compared to samples that were left in air at room temperature during this month rather than incubated in blood plasma as reference samples. The results are shown in Fig. 3.16 for a set of samples done in triplicate. In comparing samples functionalized with 100% PEG versus 100% A type II antigen, it is evident that there is an increase in absorbance when the A type II antigen is present. Even after a month of incubation in blood plasma increased absorbance can still be noted, and therefore the antigen is still present and accessible. One point of interest is the decrease in detection of the A antigen when incubated in O blood plasma over A blood plasma. As anti-A antibodies would be found in O blood plasma, but not in A blood plasma, these

results are promising in suggesting that the human anti-A antibody recognizes the synthetic A antigen used in this study.

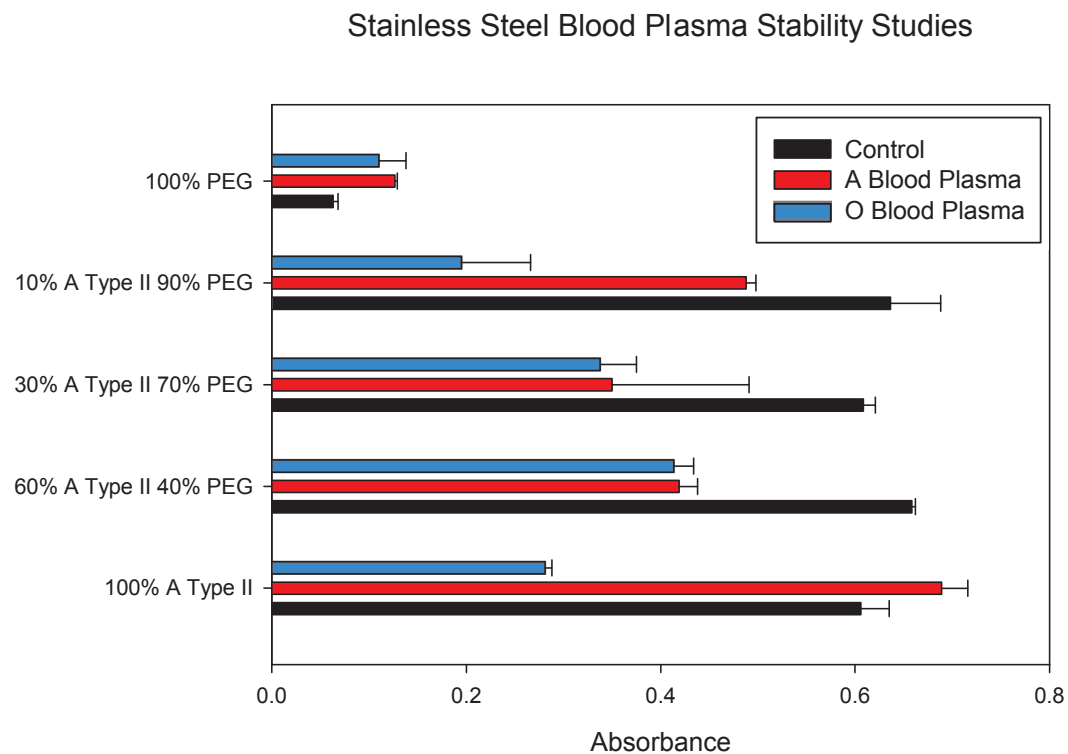


Figure 3.16. Detection of A antigens by ELISA assay before (as a control) and after incubation in A or O blood plasma for a month.

Alumina ALD coated stainless steel were also functionalized with PEG and A antigen silanes. Similar results of antigen detection were achieved with stainless steel coupons coated with alumina by ALD without incubation in blood plasma. Although alumina could potentially be another exceptional coating for functionalization, a coating superior to silica could not be determined within the limits of our experimentation. As such, further study of alumina thin films was not completed. Additionally, the extensive availability of silica substrates, from oxidized silicon to glass microscope slides, makes it an ideal substrate for further characterization.

From preliminary results of detecting silicon on stents coated with silica by sol-gel dip coating from AES (discussed in the previous chapter), functionalization of

stents with A type I and PEG silane was performed. Three different ratios of A antigen to PEG were used: 0% A type I: 100% PEG, 10% A type I: 90% PEG, and 20% A type I: 80% PEG. These A antigen functionalized stents were expanded in a porcine model, ideal for our purposes as they have two of the same blood types as humans, both A and O. The suppression of anti-A antibodies is the goal of our work on stainless steel. Anti-A antibodies would be present in adult O blood type pigs, but not A type pigs. Therefore, two stents of each of the three functionalizations listed above were prepared. One stent of each functionalization was expanded in a male and a female O blood type piglet. O blood type pigs tend to produce anti-A antibodies by the age of 2 months. Unfortunately, the results after months of blood sample collection were inconclusive for the successful suppression of anti-A antibodies. However, this is not surprising given the data collected regarding this type of coating (discussed in the previous chapter). A number of plausible scenarios may have led to the inconclusive suppression of the anti-A antibodies in the porcine model. The stents may have been insufficiently insulated and non-specific protein binding could have coated the stents, leaving the devices with inadequate biological availability of the A type antigen. Alternatively, the functionalization may have been incomplete, giving rise to insufficient coverage to elicit our desired results in the porcine model. In either case, this data does not in and of itself disprove the utility of the more suitable functionalized ALD silica-coated stainless steel protocol developed thus far. Another round of stents must be tested, again in a porcine model to draw further conclusions.

In addition to stainless steel and silica-coated stainless steel, glass microscope slides were used to attach TSs. ToF-SIMS mapping was used in an attempt to evaluate the mixing of A antigen and PEG silanes on glass microscope slides. ToF-SIMS has been used extensively in order to characterize biological molecule attachment to surfaces.(16,26,44,47,48) The ToF-SIMS mapping identified specific A antigen fragments, such as the NAc, confirming the presence of A antigens. No apparent spotting in the antigen fragments derived from the silane

mixtures identified by mapping of the functionalized glass substrates. As such, no segregation of the PEG and A antigen silane mixture on the microscale could be identified.

However, the functionalization of these glass substrates in an array of spots was performed with a microarray printer, but lead to issues associated with the sol-gel solution. The pins of the microarray printer became clogged and therefore inefficient spot functionalization was performed. Fine-tuning of the acidic sol-gel parameters was attempted, using alternative alcohol solvents such as butanol, more and less acidic solutions, different sources of water, and different curing times were examined. However, little improvement in the clogging of the pins was established.

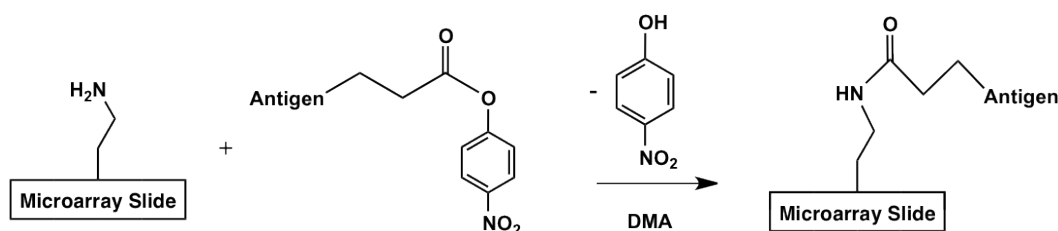


Figure 3.17. ABO antigen carbohydrate conjugation to amine-functionalized microarray slides.

Conjugation of all 18 ABO subtype antigens (6 subtypes of each A, B, and H antigens which are the carbohydrates present on A, B, and O blood type cells respectively) was successfully performed on amine-functionalized microarray slides using a microarray printer. The successful conjugation method for TS antigens is shown in Fig. 3.17. Each of the antigens was identified using the same ELISA used to detect A type II on silica-coated stainless steel. Microarrays were also incubated in samples of blood-typed human blood plasma to characterize the antibodies produced by the blood donors. Antibody detection was then performed to detect the antibodies – a slight variation on the ELISA assays used to detect the ABO antigens, outlined in the experimental section. These microarrays can allow for more extensive blood typing, which could enhance the determination of the

possible donor pool for those who require transplants of organs, tissue or blood. This could, in turn, reduce rejection of donor organs as this subtyping could reduce the chance of selecting organs to which a patient produces antibodies. Alternatively, this could also expand the donor pool to donor samples from additional blood types for which the patient produces no antibodies.

CONCLUSIONS

Silica coated ALD stainless steel was previously determined to be the ideal candidate for subsequent functionalization. These substrates were first functionalized with model biological molecules. Two synthesized monosaccharide (MS) silanes, N-acetyl glucosamine (GlcNAc) and galactose (Gal), were selected for the availability of appropriate lectins for their detection. The successful functionalization of silica with silanes was first performed on oxidized porous silicon and was characterized by transmission FTIR. The functionalization of ALD silica coated stainless steel was also characterized by low resolution XPS. The elemental analysis of nitrogen, sulfur and oxygen correlate well with corresponding solution mixtures of the PEG and MSs used to functionalize the uncoated and silica coated stainless steel coupons examined by XPS. The corresponding enzyme-linked lectin assays (ELLAs) successfully detect the biological availability of both GlcNAc and Gal. The results also indicate that the silica coating is useful in the prevention of non-specific protein binding.

Furthermore, the silica coated stainless steel substrates were found to be successfully functionalized with A antigens, as determined by elemental analysis through XPS evaluation. Additionally, ToF-SIMS mapping evaluation detected antigen-specific fragments in spots functionalized with antigen and across functionalized films. The biological availability of A antigens on the silica on stainless steel substrates was recognized by ELISA assays both with and without incubation in human blood plasma. Additionally, the synthetic A antigen used to functionalize these substrates appears to be effectively recognized by human anti-A antibody from O blood plasma. Synthetic antigens for all the ABO subtypes

were also conjugated onto substrates in microarrays, and antigens detected through assays. The microarrays were subsequently used to identify ABO antibodies present in the blood plasma of blood-typed donors.

EXPERIMENTAL

Materials.

Hydrofluoric acid, nitric acid and sulphuric acid were purchased from J. T. Baker and used as received. Hydrogen peroxide, methylene chloride and acetone were purchased from Fischer Scientific and used as received. Glacial acetic acid, sodium chloride (ACS grade), magnesium chloride hexahydrate (ACS grade), potassium chloride (ACS grade), calcium chloride (anhydrous), and sodium bicarbonate (ACS grade) were purchased from EMD and used as received. 100% ethanol was purchased from Commercial Alcohols and used as received. Tetraethyl orthosilicate (reagent grade, 98%), 3-mercaptopropyl trimethoxysilane (MPTMS), peroxidise conjugated lectins (WGA-L3892 and PNA-L7759), and potassium chloride (99.999%) were purchased from Aldrich and used as received. The *o*-phenylenediamine (OPD) indicator was purchased from Aldrich (SIGMAFAST OPD P9187) and prepared according to the manufacturer's instructions 2-[methoxy(polyethyleneoxy)propyl]-trimethoxysilane (PEG) was purchased from Gelest Inc. and used as received. 18 M Ω (Barnstead) water was freshly generated before use. 0.9 mm thick, annealed, mirror polished both sides stainless steel AISI 316L (Fe/Cr18/Ni10/Mo3) foil was purchased from Goodfellow Cambridge Limited. DAROCUR 1173 (2-hydroxy-2-methyl-1-phenyl- propan-1-one) was purchased from Ciba Speciality Chemicals. Superamine 2 (SMM2) microarray slides were purchased from Arrayit. Fluorochromes (Dylight 549TM or Dylight 649TM) conjugated goat anti-human IgM, IgG and IgA antibodies were purchased from Jackson ImmunoResearch Laboratories, Inc. The Anti-A mouse IgM was purchased from Virogen (Anti-A1, A2, A3 Cat# 133-A), whilst the secondary goat anti-mouse IgM HRP antibody was purchased from Southern Biotech (1021-05). 96-well hybridization cassette (AHC4x24) was purchased from Arrayit Corporation. Palmaz-Schatz PS204C

balloon expandable stainless steel stents were obtained from Johnson & Johnson (Miami, FL). The monosaccharides were prepared as described previously.(40)

Methods.

Preparation of oxidized porous silicon. Previously published conditions were used to etch 1 cm x 1 cm N-type Si(100) 0.01 – 0.02 $\Omega\cdot\text{cm}$ silicon wafers.(49) A Teflon cell was used to electrochemically etch 0.38 cm^2 . The required current (7.6 mA/cm^2 for 2 minutes, followed by 76 mA/cm^2 under white light illumination using a 300W tungsten filament ELH bulb) was applied using an EG & G Instruments Princeton Applied Research model 363 potentiostat. The reference electrode used was Ag/Ag^+ and platinum wire was used as the counter electrode. A heavy aluminum foil was used to make electrical contact the backside with the silicon wafer, which acted as the working electrode. The porous silicon was washed extensively with 100% ethanol and dried under nitrogen immediately following etching. To oxidize the surface, the porous silicon was dipped into piranha for 15 minutes (cooled for an hour before use). The piranha solution was prepared from a 1:3 mixture of concentrated sulfuric acid: 30% hydrogen peroxide. [WARNING: The preparation of piranha solution is highly exothermic, and the mixture extremely reactive toward organic solvents. Preparation and use of piranha should be performed with extreme caution!] The piranha-cleaned substrates were washed with copious amounts of 18 $\text{M}\Omega\cdot\text{cm}$ water to dilute the reactive piranha, and dried with nitrogen. The oxidation of the SiH_x surface to $\text{Si}(\text{OH})_x$ was confirmed by transmission FTIR spectroscopy. This freshly cleaned surface was immediately functionalized.

Porous silicon surface functionalization. The freshly cleaned porous silicon wafer was secured in a metal FTIR sample holder with a Viton o-ring. After being scanned with transmission FTIR spectroscopy, the porous silicon wafer was subsequently functionalized in tandem with 316L stainless steel or silica-coated stainless steel samples using the same solutions. The surface functionalization procedure was slightly modified in that 100 μL of the correct solution (100%

monosaccharide, 60% monosaccharide – 40% PEG silane, etc.) was placed into the well and onto the porous silicon wafer, and left there to react for two minutes. After the two minutes, the sample holder was tilted such that the solution ran out of the well, and the sample cured at 110°C for 15 min, followed by cooling for 15 min. Another scan with FTIR spectroscopy was performed before rinsing the sample and acquiring a third FTIR scan. As the porous silicon wafer was not removed from the sample holder, presumably the laser passed through the same portion of the porous silicon. The sample was then rinsed copiously with methanol, and dried under a stream of nitrogen, before being scanned a final time with transmission FTIR spectroscopy.

Surface Functionalization. The silica and stainless steel substrates were hydroxy terminated by cleaning with fresh piranha. The uncoated or silica-coated 316L stainless steel sample was immersed in piranha for 60 s. The piranha solution was prepared from a 1:3 mixture of concentrated sulfuric acid: 30% hydrogen peroxide. [*WARNING: The preparation of piranha solution is highly exothermic, and the mixture extremely reactive toward organic solvents. Preparation and use of piranha should be performed with extreme caution!*] The piranha-cleaned substrates were washed with copious amounts of 18 MΩ•cm water to dilute the reactive piranha, and dried with nitrogen. The freshly prepared sample was immersed directly in the silane solution as outlined below immediately after the generation of the hydroxylated surface.

100% saccharide surface functionalization. In a typical experiment, 5 mg of either the monosaccharide model compound (527 g/mol; 9.48×10^{-6} mol), or the TS silane (1038 g/mol; 4.81×10^{-6} mol), was dissolved in 0.25 mL of 95% ethanol with 1% acetic acid. This solution of silanes was allowed to stand for 15 minutes prior to use to allow for the hydrolysis of the trimethoxysilane groups to silanols. The sample was agitated in the trimethoxysilanes solution for 2 minutes, prior to dip rinsing in 100% EtOH, and curing for 15 minutes in an oven heated to 110°C.

After curing, a white residue composed of excess saccharide not bonded to the silica surface, is visible. Rinsing the sample with methanol dissolved the residue.

20% saccharide, 80% PEG surface functionalization of substrates. In a typical experiment, 5 mg of either the MS silane (527 g/mol; 9.48×10^{-6} mol), or the TS silane (1038 g/mol; 4.81×10^{-6} mol), was dissolved in 0.25 mL of 95% ethanol with 1% acetic acid. To this solution, 0.47 mL of a solution comprised of 44 μ L for MS (22 μ L for TS) 2-[methoxy(Polyethyleneoxy)propyl]-trimethoxysilane (47mg, average MW = 550g/mol, 8.54×10^{-5} mol for monosaccharide; or 24 mg, 4.33×10^{-5} mol for tetrasaccharide) 95% ethanol with 1% acetic acid was added. This solution of silanes was allowed to stand for 15 minutes prior to use to allow for the hydrolysis of the trimethoxysilane groups to silanols. The sample was aggitated in the trimethoxysilanes solution for 2 minutes, prior to dip rinsing in 100% EtOH, and curing for 15 minutes in an oven heated to 110°C.

10% saccharide, 90% PEG surface functionalization of substrates. In a typical experiment, 5 mg of either the MS silane (527 g/mol; 9.48×10^{-6} mol), or the TS silane (1038 g/mol; 4.81×10^{-6} mol), was dissolved in 0.25 mL of 95% ethanol with 1% acetic acid. To this solution, 1.06 mL of a solution comprised of 44 μ L for MS (22 μ L for TS) 2-[methoxy(Polyethyleneoxy)propyl]-trimethoxysilane (47mg, average MW = 550g/mol, 8.54×10^{-5} mol for monosaccharide; or 24 mg, 4.33×10^{-5} mol for tetrasaccharide) 95% ethanol with 1% acetic acid was added. This solution of silanes was allowed to stand for 15 minutes prior to use to allow for the hydrolysis of the trimethoxysilane groups to silanols. The sample was aggitated in the trimethoxysilanes solution for 2 minutes, prior to dip rinsing in 100% EtOH, and curing for 15 minutes in an oven heated to 110°C.

100% PEG surface functionalization of substrates. In a typical experiment, 22 μ L of 2-[methoxy(polyethyleneoxy)propyl]-trimethoxysilane (24 mg; 4.33×10^{-5} mol) was dissolved in 1.0 mL of 95% ethanol with 1% acetic acid. This silane solution was allowed to stand for 15 minutes prior to use to allow for the hydrolysis of the

trimethoxysilane groups to silanols. The sample was agitated in the trimethoxysilane solution for 2 minutes, prior to dip rinsing in 100% ethanol, and curing for 15 minutes in an oven heated to 110°C.

Conjugation of carbohydrate antigens to microarray slides. The p-nitrophenyl ester versions of the antigens were previously described.(41) The amine functionalized microarray slides were first prepared by dipping them into a solution of 3% triethylamine in *N,N*-dimethylacetamide (DMA), rinsed with methanol and dried under argon. In a typical experiment, 1.7 mg antigen was dissolved in 120 μ L DMA. This solution was printed on the array slides using a pin microarray device. Before use of the microarrays for antigen or antibody detection, the slides were dipped into water and methanol.

Characterization.

Preparation of phosphate buffer saline solution (PBST). For the biological assays, PBST at pH 7.4 was prepared, containing 0.1% Tween-20. Phosphate buffer saline consists of a solution of 137 mM NaCl, 2.7 mM KCl, 100 mM Na₂HPO₄, 2 mM KH₂PO₄ in deionized water.

Biological assay for determining monosaccharide attachment. Each 2 x 5 mm substrate was shaken in 2% BSA in PBST (100 μ L) for 14 h at 5°C. The substrate was then shaken at room temperature in a solution of the lectin (PNA or WGA) (0.01 mg/mL, 200 μ L) in 2% BSA PBST for 2 h. The substrate was washed copiously with PBST to remove unbound lectin. The substrate was then treated with 500 μ L OPD and left to react for 1 h. An aliquot of this solution (200 μ L) was then taken and the absorbance measure at 450 nm.

Biological assay for determining A type tetrasaccharide attachment. Each silica coated stainless steel stent surface was treated with a solution of 2% BSA in PBST (200 μ L) and shaken (14 h, 5°C). The surface was then removed and then incubated with mouse anti-A IgM antibodies (5 °C, 14 h, 0.023 mg/mL, 50 μ L).

The surface was then removed, thoroughly washed with PBST and then treated with a secondary HRP conjugated goat anti-mouse IgM antibody (21 °C, 3 h, 0.013 mg/mL, 50 µL). The surface was thoroughly washed with PBST to remove unbound antibody and then treated with a solution of SigmaFast OPD (200 µL, 1h). An aliquot of this solution (100 µL) was then taken and the absorbance measure at 450 nm.

Blood plasma stability studies of A type I antigen functionalized uncoated and silica-coated stainless steel. Several substrates bearing the A type I antigen were prepared, according to the general procedure defined above. Each of the samples was placed in one of two different types of human donor blood plasma (blood group O and blood group A plasma). The samples were agitated for a month in blood plasma at 37°C. The blood plasma was replaced every 2-3 days. After removal from blood plasma, the substrates were immersed in PBST for an hour before being stored in ethanol before further characterization. These incubated samples were also compared to samples that were left in air during this month rather than incubated in blood plasma as reference samples.

Detection of antibodies on microarray slides. The amine functionalized slides were loaded up to four slides at a time per 96-well cassette to allow simultaneous detection and processing of multiple microarrays. The microscope slides were washed with PBS/Tween-20 followed by an hour blocking with 3% normal goat serum/PBS at room temperature. Blood plasma was diluted 1:20 – 1:150 in blocking buffer and 50 µL was loaded into each well to react for 30 minutes at room temperature. Subsequently, the slides were washed with PBS/Tween-20. Bound human antibodies were detected with fluorochrome conjugated goat anti-human antibodies for which a Roche Nimblegen, Inc. Nimblegen™ MS200 microarray scanner, with 2-5 µm resolution, was used to scan the slides. Biodiscovery, Inc. Image™ software was used analyze the samples.

Other characterization. XPS (Kratos Analytical, Axis-Ultra) was performed under high vacuum ($<10^{-8}$ Torr) using monochromatic Al KR with a photon energy of 1486.6 eV, in the Alberta Centre for Surface Engineering and Science (ACES). The spectra were calibrated on the basis of the C 1s peak. FTIR (Fourier transform infrared) spectra were collected on a Nicolet Nexus 760 spectrometer. FTIR spectra for porous silicon samples were collected in transmission mode using a nitrogen purged sample chamber, a DTGS KBr detector, with 32 scans at 4 cm^{-1} resolution. Absorbance was measured at 450 nm on a Molecular Devices SPECTRAMax 340PC UV/Vis spectrophotometer. Fluorescence was measured on a Molecular Devices SpectraMax M2 microplate reader.

ACKNOWLEDGEMENTS

CIHR and NSERC for funding of this project. NSERC and AIF for scholarship funding. Dr. Vincent Wright for his substantial work on this project including much experimental functionalization of the monosaccharides and antigens and their subsequent characterization. Dr. Todd Lowary and Dr. Peter Meloncelli for their part in the experimental work, including the preparation of MS and TS silanes. Dr. Lori West and Dr. Jeyakanthan Mylvaganam for their work with the samples incubated in blood plasma. ACSES for XPS and ToF-SIMS data and evaluation.

REFERENCES

1. Balamurugan, S.; Soto-Cantu, E.; Cueto, R.; Russo, P., *Macromolecules* **2010**, *43* (1), 62-70.
2. Gann, J.; Yan, M., *Langmuir* **2008**, *24* (10), 5319-5323.
3. Banet, P.; Marcotte, N.; Lerner, D.; Brunel, D., *Langmuir* **2008**, *24* (16), 9030-9037.
4. Sharma, S.; Johnson, R.; Desai, T., *Biosens. and Bioelectron.* **2004**, *20* (2), 227-239.

5. Sinapi, F.; Naji, A.; Delhalle, J.; Mekhalif, Z., *Surf. Interface Anal.* **2004**, *36* (11), 1484-1490.
6. Lundberg, P.; Bruin, A.; Klijnstra, J.; Nystrom, A.; Johansson, M.; Malkoch, M.; Hult, A., *ACS Appl. Mater. Interfaces* **2010**, *2* (3), 903-912.
7. Yan, M.; Ren, J., *Chem. Mater.* **2004**, *16* (9), 1627-1632.
8. Li, G.; Lang, P.; Qin, W.; Maitz, M.; Zhou, S.; Huang, N., *Biomaterials* **2011**, *32* (21), 4691-4703.
9. Lin, Q.; Ding, X.; Qiu, F.; Song, X.; Fu, G.; Ji, J., *Biomaterials* **2010**, *31* (14), 4017-4025.
10. Lin, Q.; Yan, J.; Qiu, F.; Song, X.; Fu, G.; Ji, J., *J. Biomed. Mater. Res. A* **2011**, *96* (1), 132-141.
11. Nakamae, K.; Miyata, T.; Ootsuki, N., *Macromol. Chem. Phys.* **1994**, *195* (7), 2663-2675.
12. Park, S.; Lee, M.-R.; Shin, I., *Chem. Commun.* **2008**, *44* (37), 4389-4399.
13. Wang, X.; Ramstrom, O.; Yan, M., *J. Mater. Chem.* **2009**, *19* (47), 8944-8949.
14. Liu, L.-H.; Dietsch, H.; Schurtenberger, P.; Yan, M., *Bioconjugate Chem.* **2009**, *20* (7), 1349-1355.
15. Bahulekar, R.; Tokiwa, T.; Kano, J.; Matsumura, T.; Kojima, I.; Kodama, M., *Carbohydr. Polym.* **1998**, *37* (1), 71-78.
16. Leonard, D.; Chevolot, Y.; Bucher, O.; Haenni, W.; Sigrist, H.; Mathieu, H., *Surf. Interface Anal.* **1998**, *26* (11), 793-799.
17. Wang, X.; Ramstrom, O.; Yan, M., *Adv. Mater.* **2010**, *22* (17), 1946-1953.
18. Yagüe, C.; Moros, M.; Grazú, V.; Arruebo, M.; Santamaría, J., *Chem. Eng. J.* **2008**, *137* (1), 45-53.
19. Slater, J.; Frey, W., *J. Biomed. Mater. Res. A* **2007**, *87* (1), 176-195.
20. Maat, J.; Regeling, R.; Yang, M.; Mullings, M.; Bent, S.; Zuilhof, H., *Langmuir* **2009**, *25* (19), 11592-11597.
21. Kaufmann, C. R.; Mani, G.; Marton, D.; Johnson, D. M.; Agrawal, C. M., *Biomed. Mater.* **2010**, *5* (2), 1-10.
22. Shustak, G.; Domb, A.; Mandler, D., *Langmuir* **2004**, *20* (18), 7499-7506.

23. Raman, A.; Dubey, M.; Gouzman, I.; Gawalt, E., *Langmuir* **2006**, *22* (15), 6469-6472.
24. Raman, A.; Gawalt, E., *Langmuir* **2007**, *23* (5), 2284-2288.
25. Mahapatro, A.; Johnson, D. M.; Patel, D. N.; Feldman, M. D.; Ayon, A. A.; Agrawal, C. M., *Nanomed. Nanotechol. Biol. Med.* **2006**, *2* (3), 182-190.
26. Al-Bataineh, S.; Luginbuehl, R.; Textor, M.; Yan, M., *Langmuir* **2009**, *25* (13), 7432-7437.
27. Yoshioka, T.; Tsuru, K.; Hayakawa, S.; Osaka, A., *Biomaterials* **2003**, *24* (17), 2889-2894.
28. Okada, M.; Masuda, M.; Tanaka, R.; Miyatake, K.; Kuroda, D.; Furuzono, T., *J. Biomed. Mater. Res. A* **2007**, *86* (3), 589-596.
29. Ruan, C.-M.; Bayer, T.; Meth, S.; Sukenik, C. N., *Thin Solid Films* **2002**, *419* (1), 95-104.
30. Earhart, C.; Jana, N.; Erathodiyil, N.; Ying, J., *Langmuir* **2008**, *24* (12), 6215-6219.
31. Nakamura, M.; Ishimura, K., *Langmuir* **2008**, *24* (9), 5099-5108.
32. Pleul, D.; Frenzel, R.; Eschner, M.; Simon, F., *Anal. Bioanal. Chem.* **2003**, *375* (8), 1276-1281.
33. Hatano, K.; Yamazaki, T.; Yoshino, K.; Ohyama, N.; Koyama, T.; Matsuoka, K.; Terunuma, D., *Tetrahedron Lett.* **2008**, *49* (39), 5593-5596.
34. Lim, J. A.; Cho, J. H.; Jang, Y.; Han, J. T.; Cho, K., *Thin Solid Films* **2006**, *515* (4), 2079-2084.
35. Liu, L.; Engelhard, M.; Yan, M., *J. Am. Chem. Soc.* **2006**, *128* (43), 14067-14072.
36. Sundararajan, G.; Ooij, W. v., *Surf. Eng.* **2000**, *16* (4), 315-320.
37. Pitt, W. G.; Morris, R. N.; Mason, M. L.; Hall, M. W.; Luo, Y.; Prestwich, G. D., *J. Biomed. Mater. Res. A* **2004**, *68A* (1), 95-106.
38. Shirahata, N.; Yonezawa, T.; Miura, Y.; Kobayashi, K.; Koumoto, K., *Langmuir* **2003**, *19* (22), 9107-9109.
39. Anderson, A.; Ashurst, W., *Langmuir* **2009**, *25* (19), 11541-11548.

40. Slaney, A.; Wright, V.; Meloncelli, P.; Harris, K.; West, L.; Lowary, T.; Buriak, J., *ACS Appl. Mater. Interfaces* **2011**, 3 (5), 1601-1612.
41. Lowary, T.; Cairo, C.; West, L.; Buriak, J.; Jeyakanthan, M.; Slaney, A.; Meloncelli, P. Method and system for ABO compatible blood type matching. US61529082, 2011.
42. West, L.; Lowary, T.; Buriak, J.; Daly, B.; Mylvaganam, J.; Meloncelli, P.; Wright, V.; Cooper, A. Methods and Systems for Inducing Immunologic Tolerance to Non-Self Antigens. PCT Patent (PCT/CA2009/001814), December, 2009.
43. Sharma, V.; Dhayal, M.; Govind; Shivaprasad, S.; Jain, S., *Vacuum* **2007**, 81 (9), 1094-1100.
44. Davies, M.; Lynn, R.; Davis, S.; Hearn, J.; Watts, J.; Vickerman, J.; Paul, A., *Langmuir* **1993**, 9 (7), 1637-1645.
45. Allen, A. K.; Neuberger, A.; Sharon, N., *Biochem. J.* **1973**, 131 (1), 155-162.
46. Lotan, R.; Skutelsky, E.; Danon, D.; Sharon, N., *J. Biol. Chem.* **1975**, 250 (21), 8518-8523.
47. Shi, H.; Tsai, W.-B.; Garrison, M.; Ferrari, S.; Ratner, B., *Nature* **1999**, 398, 593-597.
48. Fritz, M.; Hahner, G.; Spencer, N., *Langmuir* **1996**, 12 (25), 6074-6082.
49. Wang, D.; Buriak, J., *Langmuir* **2006**, 22 (14), 6214-6221.

CHAPTER 4 – SYNTHESIS OF SILICA NANOPARTICLES AND MICROPARTICLES

INTRODUCTION

Nanotechnology has a lot of potential in biomedical applications including drug delivery and immunoassays since many biological processes occur on the nanoscale.(1-10) The size and surface composition of NPs are of particular interest for their displayed properties and ease of manipulation.(1,3,7,11,12) Multifunctional NPs incorporating ceramic, magnetic, fluorescent and biomolecule materials have become increasingly popular for nanobiotechnology applications.(2,9,12-20) Some examples of multifunctional nanoparticles and their applications are available in Fig. 4.1.

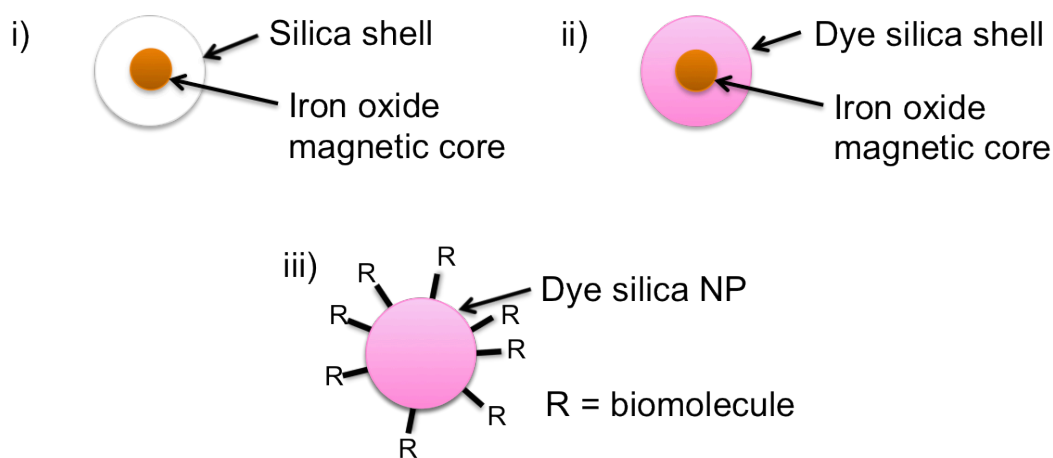


Figure 4.1. Multifunctional nanoparticles have numerous applications depending on their constituent materials. i) Iron oxide core-silica shell nanoparticles have applications in MRI contrast agents, targeted drug delivery, and magnetic separation.(13) ii) Iron oxide core-dye silica shell nanoparticles have applications in MRI contrast agents, targeted drug delivery, magnetic separation, cell labeling, and biosensing.(14,15,17,20) iii) Silica dye nanoparticles functionalized with biomolecules have applications in bioassays, imaging, drug delivery and liquid crystal displays (LCDs).(9,12)

Silica NPs, from simple to multifunctional, are inexpensive and easy to synthesize making them an ideal candidate for a number of different industrial applications.(9,21-27) Silica is a choice material for its biocompatibility and absence of toxicity even at reasonable quantities.(1,10,22,23,25-34) The mechanical, chemical and physical properties of silica are also beneficial, including its resistance to degradation in biological environments and environmentally friendliness.(1,22,23,28,35,36) The properties of incorporated NPs and molecules such as fluorophores are typically unaffected and protected by incorporation into silica.(3,20,28,35,37-39) Additionally, the hydroxylated surface of silica NPs allows for their functionalization with desired molecules such as silane derivatives of biomolecules.(1,3,9,12,20,25,26,28,35,40,41)

The Stöber synthesis is an ideal method for synthesizing silica NPs requiring only a silicon alkoxide, water, ammonia as the catalyst, and an alcohol solvent, shown in Fig. 4.2.(1,3,9,21,25,31,32,36,38,42-48) The Stöber synthesis does not require the more complicated strategy that the micro-emulsion requires involving large amounts of stabilizer and therefore a number of purification steps.(19,26,31,44) The Stöber synthesis is an effective and simple method to synthesize spherical monodisperse nanoparticles 10-2000 nm when experimental factors such as temperature are controlled.(21,31,32,43-46,49) Through a seeded or shell growth method, nanoparticles can be introduced into a reaction vessel and used as cores in the Stöber reaction for controlled increase in particle size up to the microparticle range.(21,42,44)

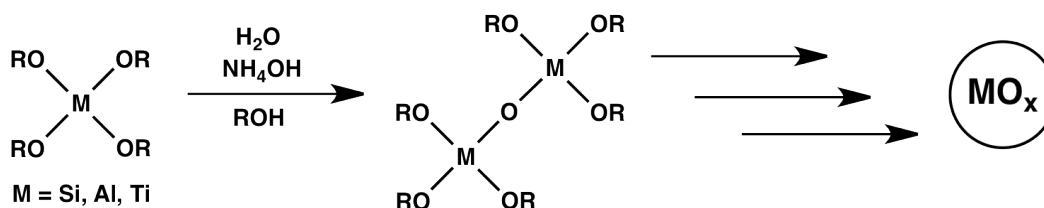


Figure 4.2. Stöber synthesis used to synthesize metal oxide nanoparticles such as silica.(1,3,21,38,45)

Magnetic qualities of NPs would be a powerful tool for their selective capture, MRI and magnetic manipulation of particles, of which iron oxide NPs offer tunability based on the synthesis technique.(1,2,13,14,17,28,33,35,39,41,50-56) One advantage is that iron oxide nanoparticle can be fabricated with superparamagnetic character so that the magnetic properties appear only when a magnetic field is applied, however, in order to prevent the aggregation of magnetic nanoparticles, they require surface modification.(13,14,28,51,52,54) Magnetic properties can be integrated into silica NPs through the incorporation of iron oxide core particles in a seeded growth synthesis.(1,2,23,51,54)

Fluorescent NPs are desirable for biomedical imaging applications, of which quantum dots have shown enormous promise for their bright and tunable fluorescence.(7,14,18,26,30,35,57-60) Although silica-coated quantum dots show promise for detection, the poor solubility, blinking and toxicity of quantum dots are still substantial issues for use in biological systems.(1,5,7,18,26,30,33,38,57-60) Organic dye incorporation in silica NPs is synthetically easy to integrate and allow for their efficient detection through fluorescence.(1,9,19,23,26,30,35,48,60,61) Decreased photobleaching has been noted for organic dye incorporated in silica in comparison to free dye in solution and covalent dye attachment incorporated in silica NPs has shown even further photostability.(1,4,5,9,14,19,20,25,26,28,30,31,35,36,48,49,55,58,61-63) The addition of silica on top of dye-doped silica has been shown to further protect the dye molecules from photobleaching from oxidation by oxygen, from interaction with solvent and from leaching of the dye molecules.(1,9,31,48,57,58,60,61)

The silica microparticles (MPs) and nanoparticles (NPs) synthesized herein were prepared via a modification of previously reported methods and different architectures were developed depending on their intended use.(43,64) Each intended use has different requirements including fluorescence, size, magnetism and functionalization and each of these factors is optimized for circulation in chicken embryo and detection by flow cytometry for immunoassays. Silica MPs

were characterized by fluorescence microscope imaging, scanning electron microscopy (SEM), and flow cytometry. Silica NPs 10-100 nm in diameter were characterized by SEM, dynamic light scattering (DLS), zeta potential measurements, two-photon excitation fluorescence correlation spectroscopy (TPE-ECS) and flow cytometry. Additionally, magnetic NPs were characterized by transmission electron microscopy (TEM).

RESULTS AND DISCUSSION

The Stöber method was used to synthesize silica nanoparticles 10-1000 nm in diameter as different sizes are required for different applications.(43-45) Nanoparticles (NPs) 10-200 nm in diameter are well suited for studies conducted in chicken embryos for effective tracking of the particles.(65) Alternatively, for single particle detection, microparticles (MPs) are better suited. In order to accurately determine the size of nanoparticles, scanning electron microscope (SEM) images were obtained of each sample. Representative SEM images of the different sizes synthesized for our purposes are shown in Fig. 4.3.

From the SEM images, the average NP diameter and standard deviation were calculated from a minimum of 75 NPs. Distribution plots for the 20 nm, 100 nm and 1000 nm NPs can be found in Fig. 4.4. From the data shown, the “20 nm” NPs are actually 21 ± 6 nm, the “100 nm” NPs are 100 ± 10 nm, and the “1000 nm” NPs (also referred to as microparticles, or “1 μm ” MPs) are 1.0 ± 0.1 μm .

Additionally, dynamic light scattering (DLS) was used to characterize the NPs and the results tend to agree with sizing obtained by SEM imaging for as-synthesized NPs. However, the DLS instrument used has a red laser and since many of the dyes used (discussed below) and iron oxide absorb or fluoresce in the red region, sizing of fluorescent and iron oxide NPs via DLS gave inaccurate results. For example, NPs with tetramethylrhodamine isothiocyanate (TRITC) dye incorporated tend to have increased size when characterized by DLS. NPs with a 30 nm TRITC dye-core, followed by a 100 nm Stöber synthesis were determined

to be 135 nm by DLS, whereas results from SEM indicate the size to be closer to 125 nm. Also, upon centrifugation, the DLS results tend to differ from results obtained from SEM images. For example, by DLS, a sample of 10 nm NPs has a Z-average size of 12 nm with polydispersity of 0.14. Following centrifugation for 20 min at 20k rpm, the Z-average size was 435 nm with a polydispersity of 0.52. In comparison, the size appears to lie closer to about 40 nm by the SEM image shown in Fig. 4.5.

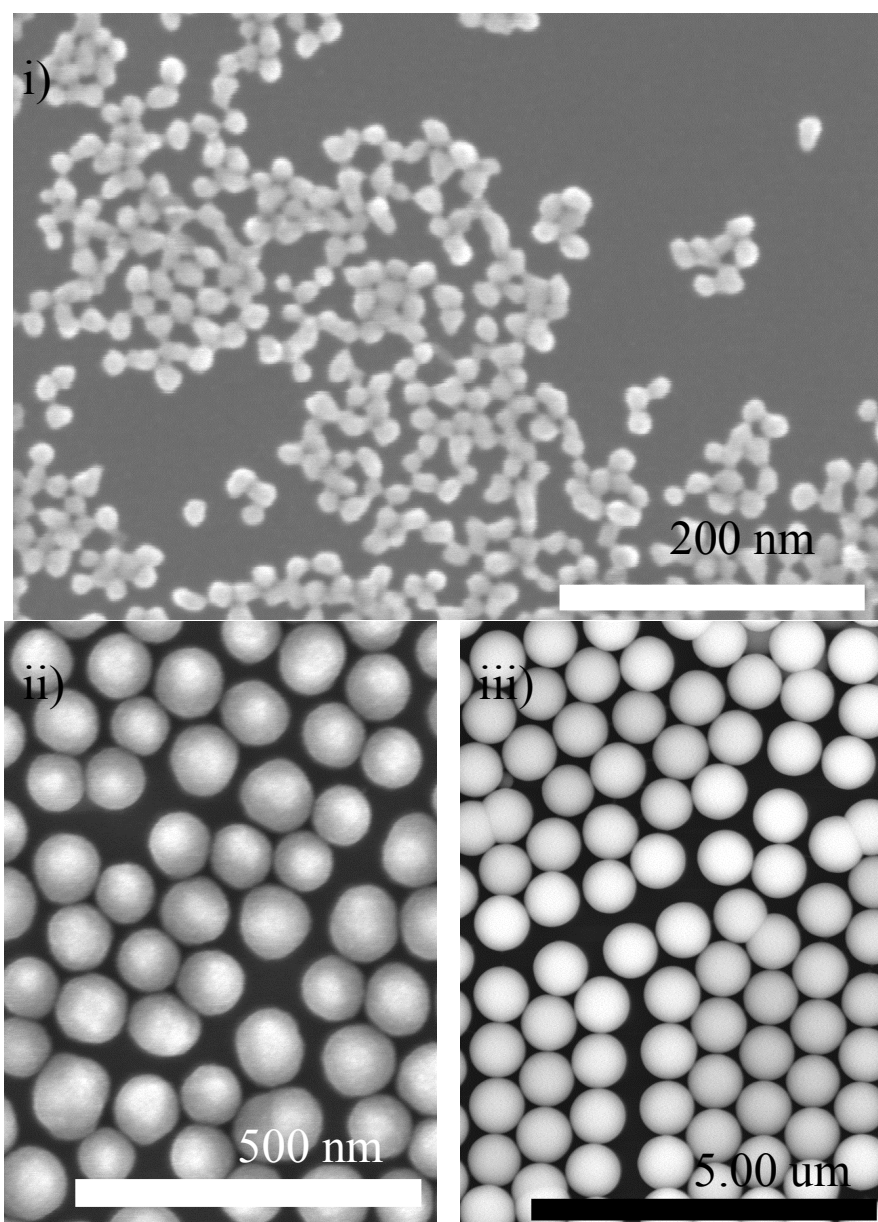


Figure 4.3. SEM images of i) 20 nm, ii) 100 nm and iii) 1 μm silica nanoparticles prepared by the Stöber method.

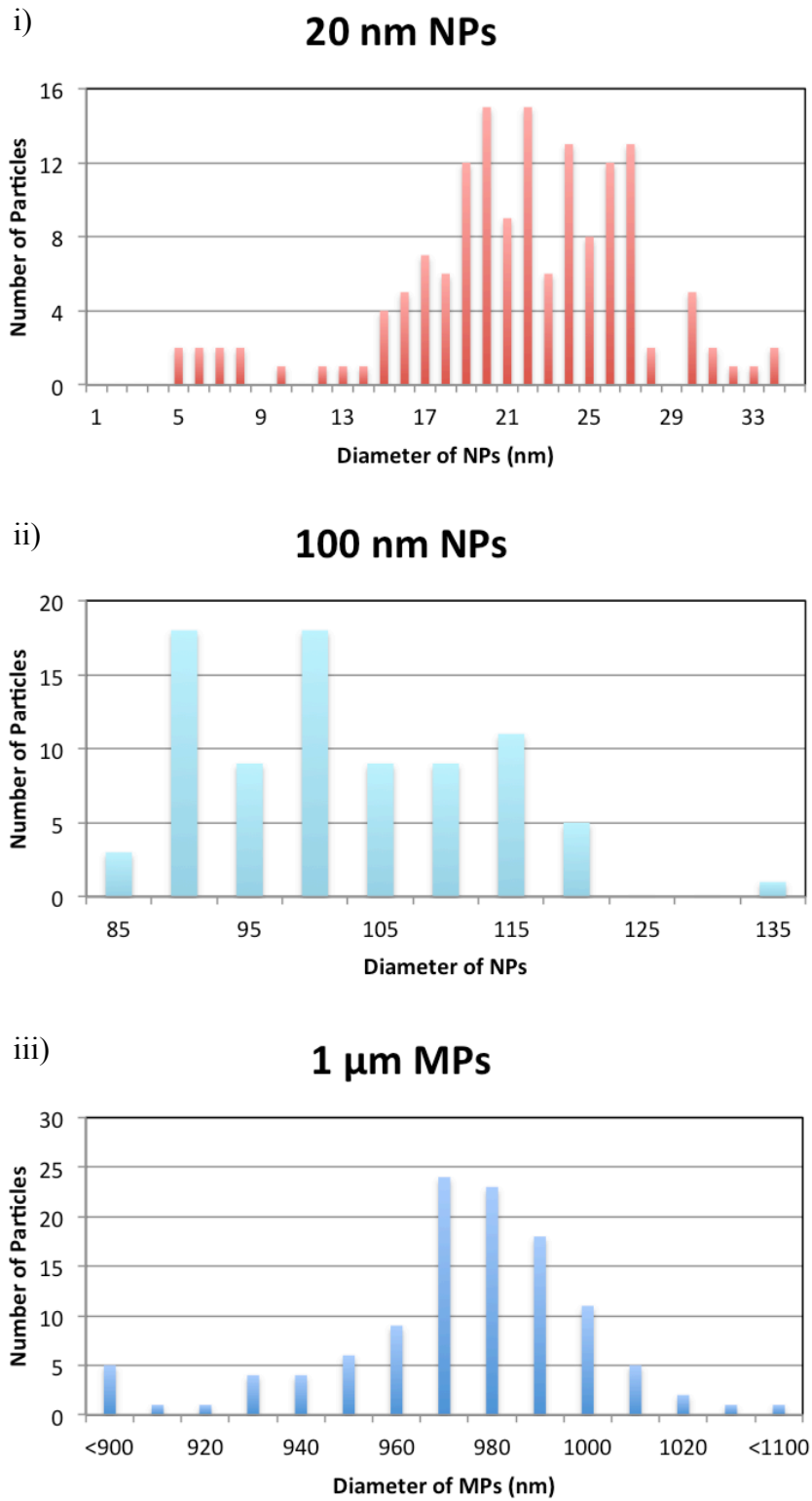


Figure 4.4. Distribution plot of sizes used to calculate the diameters of i) 20 nm, ii) 100 nm and iii) 1 μm silica particles.

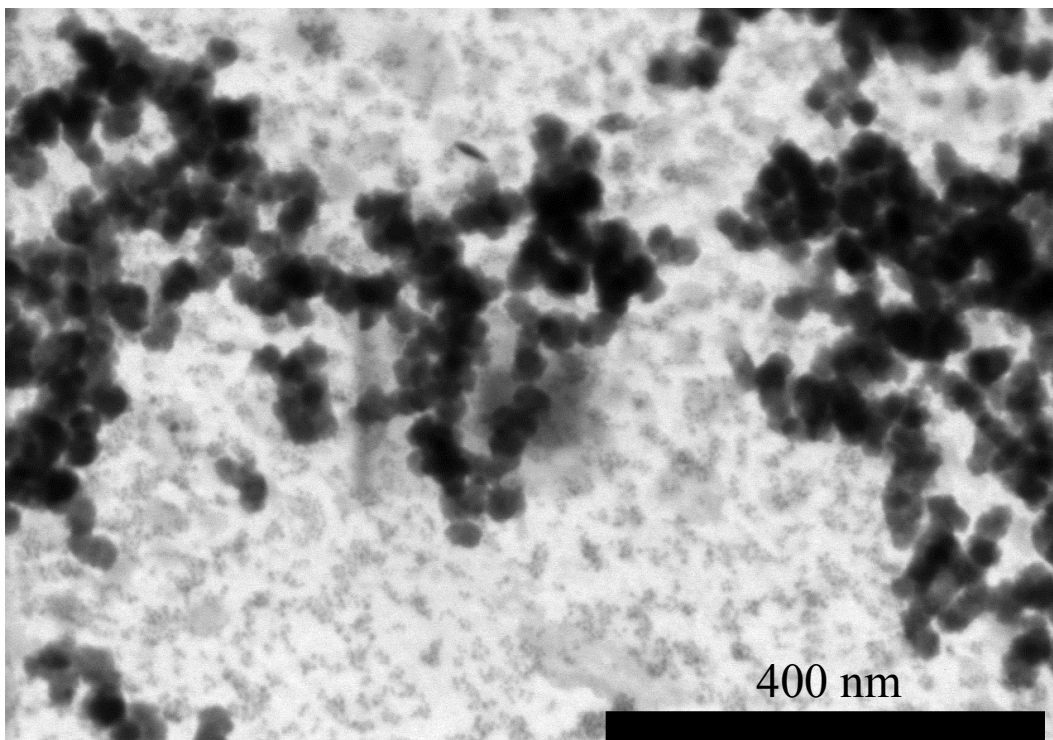


Figure 4.5. SEM image of 10 nm NPs after centrifugation.

One drawback of DLS is that it could not be used to size the MPs. For ideal DLS measurement, a concentration of about 1 g/mL should be used. However, this is difficult to control as the MPs are heavy, and settle out of solution within a couple of minutes. Since a DLS measurement takes about 5 min, the majority of the MPs will not stay in solution before the final measurement is taken.

Some functionalized NPs were characterized by DLS as well. For 100 nm Stöber NPs, the size increases from 100. to 105 nm upon functionalization with mercaptopropyltrimethoxysilane (MPTMS). On the other hand, 100 nm Stöber NPs with random R6G dye incorporation were ~140 nm when unfunctionalized and increase insignificantly by ~1 nm when functionalized with a poly(ethylene glycol) (PEG) trimethoxysilane containing 6 to 9 repeat units. Although the results may not be completely consistent with SEM data, some generalizations can be made. NPs with Rhodamine dye or iron oxide tend to appear larger by DLS with this tool, and the size of NPs increases upon functionalization.

The nanoparticles 100 nm or larger were cleaned through centrifuging, decanting and dispersing by sonication three times. However, this cleaning procedure becomes an issue with the smaller NPs since aggregation was noted experimentally in the cleaned NPs.(8,12). The centrifuged particles remained as a pellet unless sonicated for hours and even after vigorous sonication, large clumps fall out of solution rapidly. The aggregation of 10 nm NPs can be seen in Fig. 4.5 and from DLS, an increase in the size of the NPs following cleaning was observed. Similar results have been observed previously.(3)

In order to purify NPs in such cases, dialysis has proven successful.(5,8,32,58,63,66) Our results showed little success in reducing the aggregation during purification of the nanoparticles using dialysis centrifuge tubes. Some success was noted using a dialysis bag for purification, however, this is a time consuming process, taking more than a week to purify the small NPs. The zeta potential of these NPs was also obtained in an attempt to determine the cause of aggregation.

The zeta potential measurements indeed lead to a plausible explanation for the aggregation of smaller NPs. Measurements reveal that 10 nm silica NPs have a zeta potential of -17.6 ± 9.3 mV, whereas 30 nm silica NPs have a zeta potential of -43.1 ± 4.7 mV. From these results, the larger NPs have a higher negative charge, which causes the NPs to repel each other even when they are in close proximity to each other, which is required for purification of the NPs. NP dispersions less than 30 mV in magnitude are generally accepted as unstable, which our data supports.(11,47) The 10 nm NPs may be insufficiently charged to repel each other and therefore prone to a condensation reaction between them when in close proximity, causing potentially irreversible bonding between NPs. As small NPs also have a high surface energy, this aggregation is promoted in order to reduce the surface energy.(12)

Some functionalization of NPs was also assessed by zeta potential measurements. Upon functionalization with APTMS, the zeta potential increases up to 59.9 ± 7.4 mV, and in contrast, functionalization using PEG silane results in zeta potential reduced up to -52.8 ± 9.9 mV. Either functionalization results in zeta potentials larger in magnitude than that of the bare NPs, which indicates that the APTMS and PEG silane functionalizations may be an effective way to reduce the aggregation of NPs. Varying effects have been observed previously based on different surface functionalization, making it valuable to evaluate different functionalizations of NPs.(24)

A number of different NP architectures were developed depending on their purpose, as outlined in Fig. 4.6. For example, for the chicken embryo studies, random dye and covalent dye incorporation throughout the NP were strategies used to allow for effective detection by two-photon excitation fluorescence correlation spectroscopy. For effective circulation in chicken embryos, the fabricated NPs were ~ 100 nm in diameter or less. In contrast, for efficient single-particle detection by flow cytometry, particles of $1 \mu\text{m}$ or larger were synthesized with sufficient fluorescence. With these large particles, more effective incorporation of dye was established with covalent-dye incorporation within a silica shell to meet the fluorescence requirements. This architecture also proved a more effective fluorophore architecture for silica NPs with incorporated iron oxide NPs.

In order to detect the NPs, fluorophore incorporation in NP design was studied. One method of dye incorporation in NPs involves functionalization of the silica NP surface with functional silanes, to which the dye can be covalently linked.(15,19,28) Our first attempt at synthesizing fluorescent NPs involved functionalization with a thiol silane, followed by reacting with a maleimide pyrene dye. Although the fluorescence could be seen visually under UV illumination, the fluorescence decreased significantly over time. This has

previously been noted, and a number of different pathways, including interaction with the solvent could cause photobleaching of the dye.(49,59)

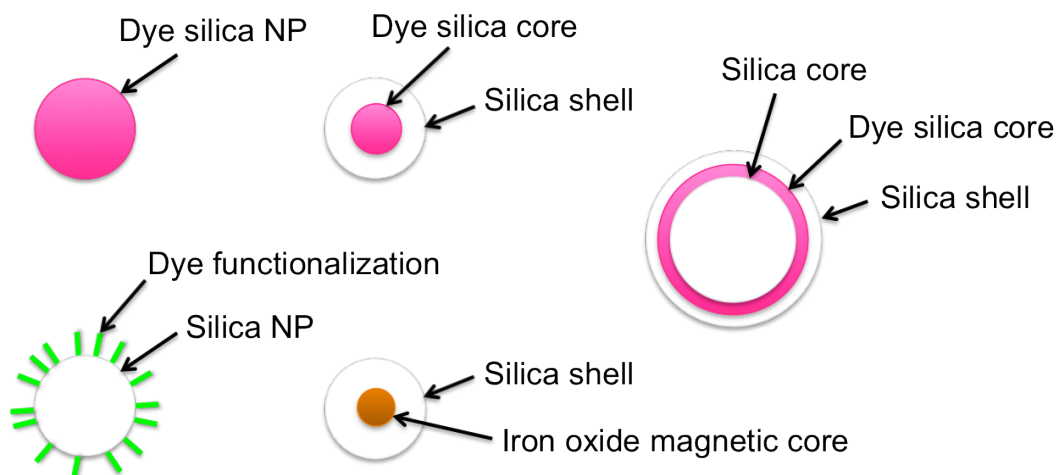


Figure 4.6. NP and MP architectures developed herein.

The dye-shell architecture displayed in Fig. 4.6 works well for MPs. It is well accepted that thin layers of sol-gel silica are transparent, however, they appear white due to their scattering of light.(5,28,35) Although not an issue when the NPs are small, the light scattering properties of silica NPs more than 100 nm in diameter becomes problematic for effective detection of incorporated dye.(12,61) Specifically, dye cores incorporated in MPs provide insufficient fluorescence for effective detection. For this reason, dye was incorporated into a shell, an effective method previously noted for dye incorporation.(14,15,33,49)

The Stöber method used to synthesize silica nanoparticles of varying diameter is easily modified in order to develop the different architectures. Although the Stöber method is an effective synthetic method, it is sensitive to experimental factors such as small changes in reagents and temperature which can vary the size of the NP product.(43,46) Even the stir rate was found to have an effect on the synthesis. For example, at a stir rate where there is a consistent dip just on the surface of the reaction solution for a 100 nm NP synthesis, the NP size was ~100 nm, however, when stirred with a large vortex, the NP size was ~120 nm. Under

the large vortex conditions, the solution splatters, leaving a white film on the side of the flask that was difficult to wash off. Stirring becomes even more critical when synthesizing MPs since the core NPs are heavy and settle out of solution if the stirring is insufficient, causing a large decrease in the monodispersity. For this reason, a 4-inch stirbar must be used in a 0.5 – 1 L vessel rather than the 2-inch stirbar used for the 300 mL vessel used in the 100 nm NP synthesis.

In refinement of the MPs, the best reproducibility and monodispersity results were obtained by larger particles grown through a shell methodology via a modification of a previously reported method.⁽⁶⁴⁾ In a typical reaction, silica core nanoparticles (~400 nm) are synthesized by the Stöber method using distilled tetraethoxysilane (TEOS), ethanol, ammonia and water.⁽⁴³⁾ The size is then increased to ~950 nm by additions of undistilled TEOS and water to the reaction mixture, creating shells of silica around the silica core nanoparticle.^(19,40,42,44,49) The distilled TEOS was found to improve the monodispersity of the synthesized core NPs, however made no significant difference in the monodispersity of the MPs when used for silica shell additions. The desired dye (an isothiocyanate derivative) is then reacted with an amine derivative of a silane, which is covalently incorporated into yet another shell.

Fluorescent dye incorporation into NPs has proven a challenge in preventing fluorophore leaching and photobleaching. A number of organic fluorescent dyes including tetramethylrhodamine isothiocyanate (TRITC), and isothiocyanate derivatives of Alexafluor 647 (AF647) and 488 (AF488) can be covalently bonded to the silica matrix of the growing silica matrix. The covalent incorporation of dyes often increases the photostability of the incorporated dye over that of the free molecule.^(61,64) Two outer silica shells, at minimum, were then added in order to further minimize photobleaching, an architecture which has proven successful under our conditions.⁽¹⁾ A fluorescence image of these microparticles can be seen in Fig. 4.7.

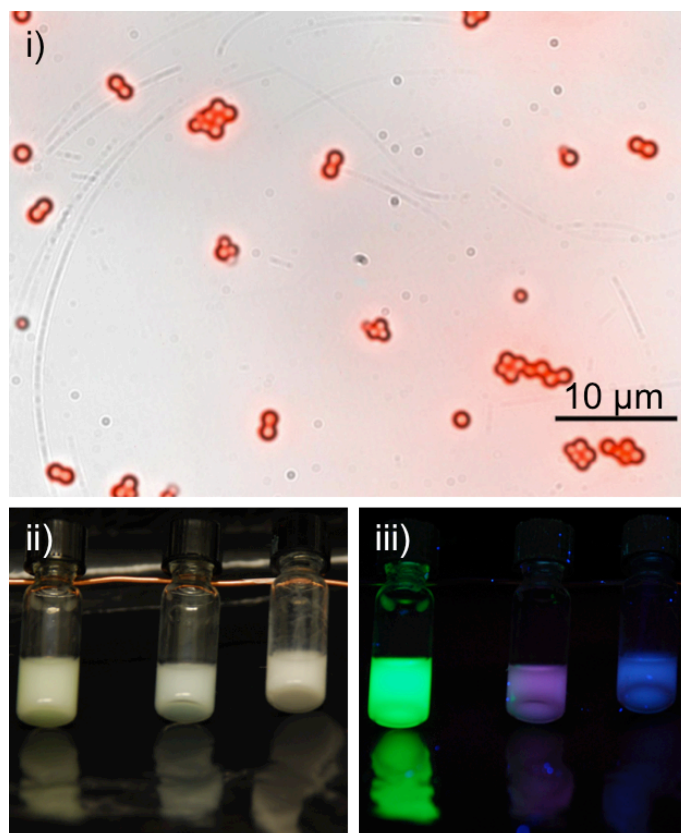


Figure 4.7. i) Silica MPs with an outer shell containing AF647 incorporated imaged using a fluorescence microscope overlay of bright field and fluorescence using a Cy5 filter. Images of MPs containing AF647, AF488, and no dye (left to right) under ii) white light and iii) UV light.

The detection of MPs with either AF647 or AF488 incorporation by flow cytometry were successful as demonstrated in Fig. 4.8. In comparison to MPs without incorporated fluorophores, greater than 99% of the fluorophore-containing MPs were detected by flow cytometry. This indicates that the incorporation of dye is effective, as well as the effective detection of these MPs by flow cytometry.

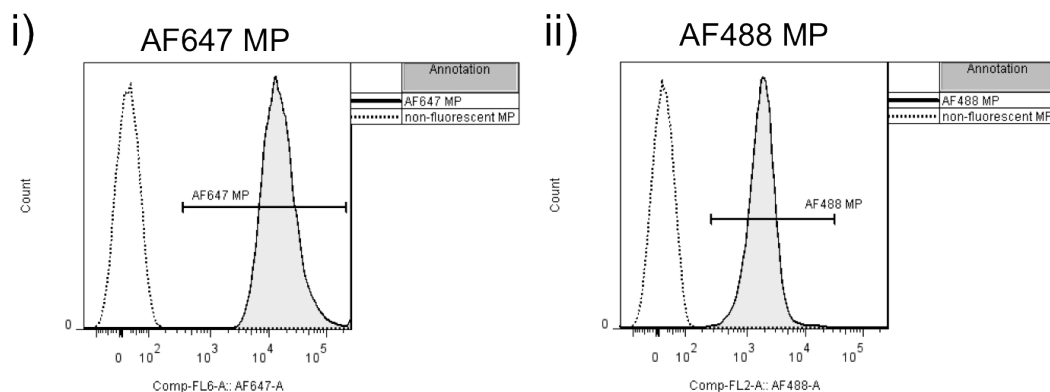


Figure 4.8. Effective detection of the fluorophores both i) AF647 and ii) AF488 incorporated in a shell of MPs in comparison to MPs without fluorophore incorporation by flow cytometry.

This dye shell was also performed using 100 nm NPs as core particles. Adding 4 shells to the 100 nm NPs results in an increase in size from 100 ± 10 nm to 120 ± 10 nm. Incorporated AF647 was also effectively detected, however it was not possible to detect single 100 nm NPs by flow cytometry.

In order to characterize the incorporated dye, excitation and emission spectra for both 100 nm and 1 μ m NPs were obtained. The absorption maximum and emission maximum reported for AF647 dye by the manufacturer are 650 nm and 668 nm respectively. The covalently-bound AF647 excitation maximum in both the NPs and MPs was about 653 nm and the emission maximum in both the NPs and MPs was about 665 nm. Although there was no deviation between the wavelengths obtained for both the NPs and MPs, the intensities were quite different. The emission intensity of the 100 nm NPs was 290 000 counts/s compared to the 35 000 counts/s for the 1 μ m MPs, a difference that arises from differences in syntheses.

The MPs were easily detected by flow cytometry, however, for detection *in vivo*, much greater fluorescence intensity is necessary. As such, the amount of fluorophore added was increased and, as demonstrated in Fig. 4.9, by increasing the amount of AF488 incorporated in the MPs, the fluorescence correspondingly

increases. No quenching of the dye was noted within the amounts of dye used and appropriate dye concentrations for further studies *in vivo* were identified. For flow cytometry detection, 500 μg AF647 per gram of MPs was determined optimal since the fluorescence is highest and stays within detection limits of our instrument at this concentration. In contrast, 800 μg AF488 per gram of MPs optimizes detection by our flow cytometry instrument.

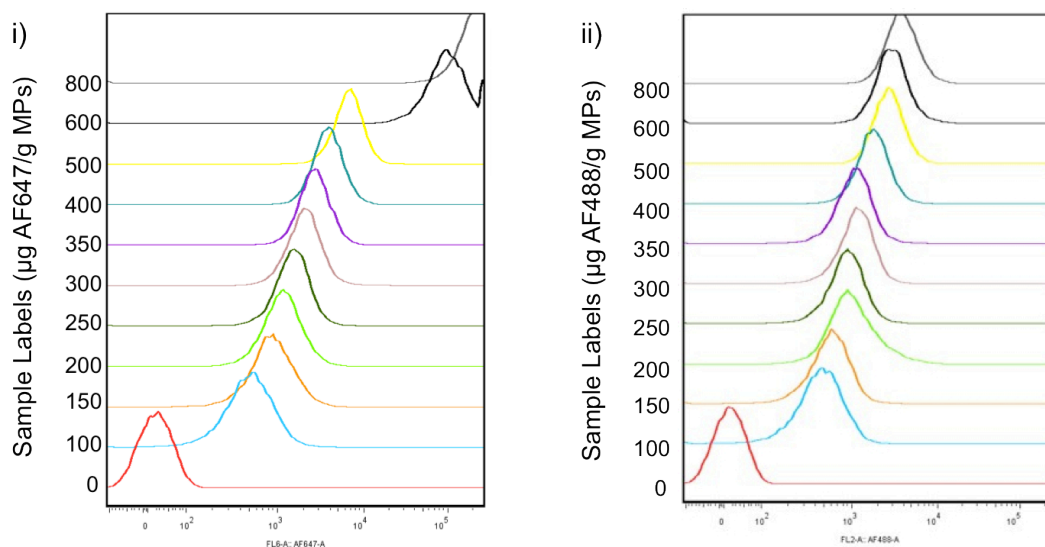


Figure 4.9. Detection of fluorescence of MPs by flow cytometry with varying amounts of incorporated i) AF647 and ii) AF488 dye.

The preparation of fluorescent core NPs was accomplished as previously reported.⁽⁶⁴⁾ The resulting NPs were approximately 30 nm in diameter and can be seen in Fig. 4.10. These particles are then added to the Stöber synthesis to give NPs of about 130 nm in diameter and the fluorescence was effective, however, their detection was ineffective by two-photon excitation fluorescence correlation spectroscopy (TPE-ECS). Instead, random dye incorporation of Rhodamine 6G (R6G) have provided a successful NP architecture for TPE-ECS characterization. In comparison to the Stöber NPs formed in the absence of dye, which have smoother, more circular shape, however, the NPs formed with incorporated dye have a rougher surface, as shown in Fig.4.3ii.

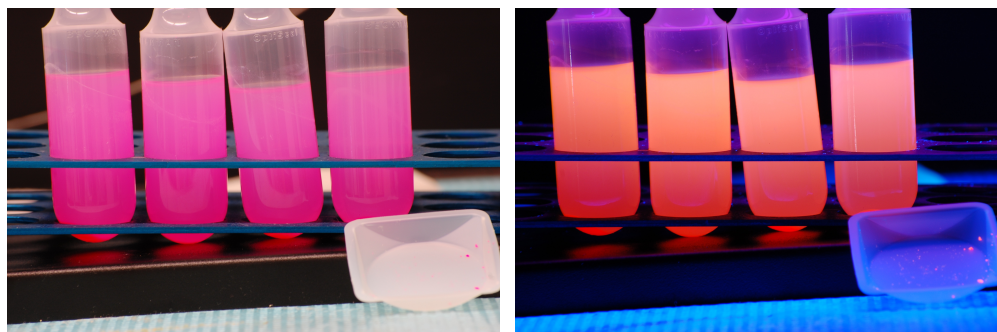


Figure 4.10. Images of 20 nm fluorescent core nanoparticles and TRITC dye under white light (left) and under UV light (right).

In a collaborative effort, the circulation behaviour and toxicity of PEGylated fluorescent silica nanoparticles of several sizes are being investigated in chicken embryos. Using TPE-ECS, the blood concentration of NPs can be measured in a living chicken embryo model. The NPs of 100 nm or less were found to stay in the vessel of chicken embryos rather than leaking, and no toxic effects were observed, and the NPs were found to circulate for up to an hour with minimal loss in fluorescence. These NPs in chicken embryos can be seen in Fig. 4.11. These results are promising in supporting the biological safety of these NPs, which is critical in their commercialization, however, any changes in the surface and size could result in vastly different results.

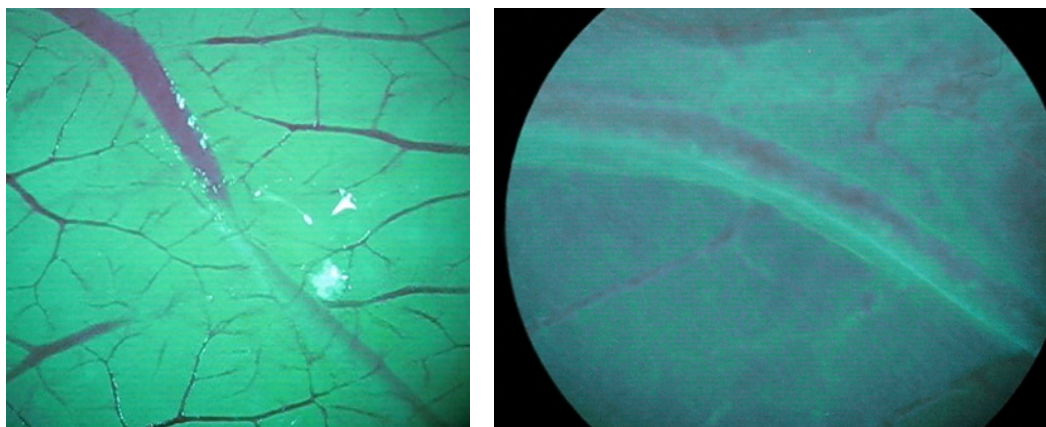


Figure 4.11. Images of nanoparticle solution injection (left), and vessel (right) in chicken embryo.

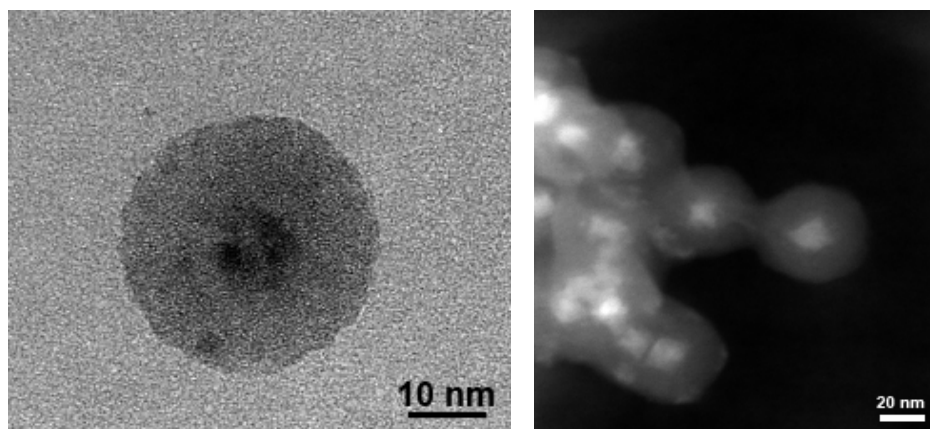


Figure 4.12. A bright field TEM image (left) and a high angle angular dark field TEM image (right) of the magnetite core nanoparticles.

Magnetite NPs are widely studied for their efficient removal from solution in the presence of a magnetic field.(2,14,39) The preparation of magnetite core nanoparticles was accomplished as previously reported.(67) The resulting nanoparticles were approximately 30 nm in diameter, shown in Fig. 4.12, which are then added to the Stöber synthesis to give nanoparticles of about 130 nm in diameter. Both the 30 nm and 130 nm NPs were effectively removed from solution using a NdFeB magnet, demonstrated in Fig. 4.13. This efficient removal occurs in about a minute and in less than a minute if the vial is placed against this magnet.

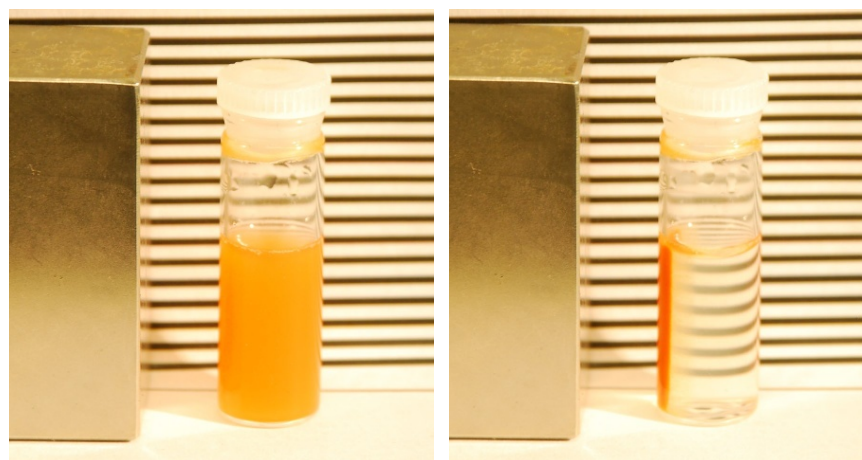


Figure 4.13. Magnetic nanoparticles in water within 5 seconds of mixing and exposure to a magnetic field (left), and their removal from solution after about a minute in a magnetic field (right).

Incorporation of dye with magnetic nanoparticles is known to be ineffective when in close proximity to iron oxide.(14,15) By incorporating dye into the silica shell directly surrounding the magnetite, no fluorescence could be detected and even by incorporating dye within the addition of the 100 nm Stöber silica layer, inefficient fluorescence was detected. However, by incorporating the magnetite cores in the MP synthesis, effective dye fluorescence was detected, but the MPs could not effectively be removed magnetically. Even at ~400 nm diameter, the NPs could not be effectively captured with a magnetic field, an effect that has previously been noted.(16) Further refinement was not conducted, however, incorporation in a MP shell has proven effective in other work.(33)

CONCLUSIONS

A variety of NPs in a range of sizes from 10-1000 nm have successfully been prepared. The sizes were confirmed by SEM images and DLS, however, DLS was ineffective for sizing MPs and many types of fluorescent NPs. Additionally, from DLS data, it was noted that smaller NPs aggregate upon centrifugation as a purification step. This aggregation was confirmed by SEM images, however, the sizes between DLS data and SEM images are inconsistent. These aggregation issues were observed for NPs less than 100 nm in diameter. From these results, the NPs less than 100 nm are insufficiently charged to effectively repel each other, necessary for the prevention of condensation reactions between NPs which would cause aggregation. Functionalization of NPs with PEG and amine silanes was also evaluated by zeta potential measurements and these functionalizations were found effective in increasing the magnitude of charge even for smaller NPs, which could effectively reduce their tendency to aggregate.

A number of different NP architectures were developed depending on their purpose, including magnetic core-shell NPs were developed in order to facilitate magnetic capture. Fluorescent NPs were also developed for effective detection, and both random dye and covalent attached dye incorporated architectures were

successfully developed. Dye incorporated into a NP shell was effective for NPs 100 nm or larger and adding silica shells to surround any incorporated dye protected the integrity of the dye. This was not performed for dye-functionalized on the surface of NPs and this architecture was found to have unsuitable photobleaching properties. The NPs with incorporated dye were successfully detected by fluorescence imaging, flow cytometry, and two-photon excitation fluorescence correlation spectroscopy (TPE-ECS). Increased dye concentration was used to achieve optimal detection by flow cytometry for potential *in vivo* and *in vitro* applications, such as the detection of antigens.

EXPERIMENTAL

Materials.

Unless otherwise indicated all materials were used as received. Glacial acetic acid, and potassium chloride (ACS grade) were purchase from EMD; 100% ethanol from Commercial Alcohols; and tetraethyl orthosilicate (TEOS) (reagent grade, 98%), (3-aminopropyl)trimethoxysilane (APTMS), sodium azide (99.5%), and sodium (99%) from Aldrich; Acetic anhydride (97%), pyridine (99%), acetonitrile (99.5%), piperidine (99%), and methanol (99.5%) from Caledon; Alexa Fluor® 488, 647 and 750 carboxylic acid, succinimidyl ester mixed isomers from invitrogen. 2-[methoxy(polyethyleneoxy)propyl]-trimethoxysilane (PEG) and 3-mercaptopropyl trimethoxysilane (MPTMS) were purchased from Gelest Inc. 18 M Ω ·cm (Barnstead) water was freshly generated before use.

NH₃, maleimide pyrene, iron oxide np reagents

Methods.

Preparation of 1 μ m Stöber microparticles (MPs). In a 500 mL Erlenmeyer flask, 340 mL of ethanol, 10.6 mL ammonia, and 38 mL 18 M Ω ·cm water were stirred magnetically with a 4-inch stirbar and the Erlenmeyer flask was covered with parafilm. At the same time, about 20 mL of distilled TEOS is obtained in a vial. Both the ethanol solution in the Erlenmeyer flask and TEOS in the vial are cooled in an icebath for a minimum of 1 h. When both are sufficiently cooled, 18.9 mL of

the distilled TEOS is added to the Erlenmeyer flask, and the flask is cooled for a minimum of an additional 4 hours, after which the flask is allowed to slowly warm to room temperature as all of the ice in the icebath melts. After the reaction is allowed to stir for a minimum of 10 hours after warming to room temperature, additions of water and TEOS are made. Each addition consists of 0.64 mL of 18 M Ω ·cm water followed by 4 mL TEOS (30 minutes after the addition of water). Each addition is added a minimum of 3.5 h following the previous addition. A total of about 22 additions are made until the size reaches over 900 nm in diameter as determined by SEM. This reaction can be stopped at any point, but the particles should be centrifuged and redispersed in the original solvent (ethanol, ammonia and water) if left more than two weeks. In the 23rd addition, 5 mg equivalent of dye from the covalent dye attachment procedure is added in order to synthesize fluorescent MPs. A minimum of two final additions are made in order to complete the synthesis of the microparticles for a grand total of 25 additions of TEOS in order to achieve the 1 μ m size. These last 3 additions must be performed within 2 days in order to preserve the integrity of the dye.

Preparation of 100 nm Stöber NPs. In a 300 mL Erlenmeyer flask, 200 mL of ethanol, 12.4 mL of ammonium hydroxide and 0.84 mL of 18 M Ω ·cm water was covered with parafilm and stirred magnetically for 30 minutes with a 2-inch stirbar at room temperature. If dye cores or random dye incorporation are being prepared, the dye cores or Rhodamine dye is added and stirred for the 30 minutes as well. Then 7.12 mL of distilled TEOS was added quickly while stirring vigorously. For covalent dye attachment NPs, the equivalent to 2 mg of isothiocyanate dye derivative is added along with 0.70 mL TEOS 30 minutes after the addition of 0.055 mL water. At minimum, one more addition of 0.70 mL TEOS and 0.055 mL water was added in order to protect the dye. These two additions (including the dye) must be performed within 2 days in order to preserve the integrity of the dye. The stirring was reduced until a consistent vortex dip in the surface of the solution is just visible. The solution was allowed to react for at

least 12 hours. The nanoparticles are cleaned through centrifuging, decanting and dispersing by sonication three times.

Preparation of 30 nm dye core NPs. This is a modification of a previously reported procedure.(64) In a 500 mL rbf, 373 mL ethanol, 5.4 mL 28 % ammonia and 6.2 mL water was stirred for 30 min. An equivalent to 1 mg of TRITC from a covalent dye incorporation synthesis and 4.5 mL TEOS are simultaneously added to the rbf. The reaction vessel was then wrapped in aluminum foil and capped with a septum. The solution is allowed to react overnight. The following day, 0.5 mL aliquots of TEOS are added every 10 min for a total of 9.5 mL TEOS, or a total of 19 times.

Preparation of 10, 20 and 30 nm Stöber NPs. This synthesis follows the general procedure outlined in the 100 nm Stöber NP. For the preparation of 10 nm NPs, 40 mL ethanol, 0.052 mL water, 0.80 mL ammonia and 1.38 mL TEOS was used. For the preparation of 20 nm NPs, 100 mL ethanol, 0.16 mL water, 2.4 mL ammonia and 3.9 mL TEOS was used. For the preparation of 30 nm NPs, 200 mL ethanol, 1.2 mL water, 6.4 mL ammonia and 4.8 mL TEOS was used.

Preparation of Fe₃O₄ core NPs. This preparation was a variation of a previous synthesis.(67) In a 100 mL 3-neck round bottom flask, 3.5 g sodium dodecylbenzene sulfanate was sonicated in 30 mL o-xylene for 15 min. In a 50 mL beaker, 0.83 g Fe(II)SO₄•7H₂O and 2.42 g Fe(III)(NO₃)₃•9H₂O were sonicated in 2.4 mL water for 15 min. The xylene mixture was then vigorously stirred using a mechanical stirrer as the iron solution was added dropwise to the round bottom flask. The solution was stirred overnight at 1060 rpm after being purged with nitrogen. The solution was then heated to 90°C and 2 mL 35% H₂N-NH₂ in water was added dropwise. Nitrogen was flowed through the system, and using an oil bubbler, the rate was about 1 bubble/s. The solution was allowed to age for 3 hours. The mixture was then cooled to 40°C and 2.0 mL TEOS was added dropwise. It was allowed to react for 16 hours. The mixture is a deep brown

colour. The NPs were centrifuged and redispersed in ethanol twice. Commonly, 5-10 mL of these final solutions are used as cores for a preparation of 100 nm silica NPs (using 100 mL of ethanol).

Covalent dye incorporation. This is a modification of a previously reported procedure.⁽⁶⁴⁾ In a glovebox, a container of 5 mg of an isothiocyanate derivative of an Alexa Fluor or TRITC dye is dissolved in 4 pipettefuls of dry ethanol and emptied into a vial wrapped in aluminum foil. The dye is allowed to stir for a minimum of 45 min before 20 μ L of distilled APTMS. The ethanol solution is allowed to react for a minimum of 10 h. The vial of dye is then added to the Erlenmeyer flask along with an addition during the addition of TEOS, whether during the addition for a shell or a core particle. This solution stays in the glovebox until immediately before use in a Stöber reaction and must be used within a week of preparation. Upon addition of this solution to a Stöber reaction, the reaction flask must be covered in aluminum foil. A minimum of two final additions of TEOS is made to protect the complete the synthesis of the microparticles.

Random dye incorporation. To a 100 mL NP batch, 0.100 g R6G was added to 100 mL ethanol. The solution is stirred until it is pink and most of the solid is dissolved. When only a grain or two of dye is left in the bottom, about 15 min of magnetic stirring, the ammonia and water are added, and stirred as per the NP synthesis procedure.

Dye surface attachment. To a 30 mL portion of 100 nm NPs functionalized with 20% MPTMS, 0.050 g of maleimide pyrene dye is added. As well, 0.12 mL 28% ammonia is added in order to ensure basicity of the solution. The solution was stirred overnight. When the solution was centrifuged in order to purify the NPs, the pellet had a distinct yellow tint in comparison to NPs without dye.

Surface functionalization with silanes. Using the average size determined from SEM images and the volume of TEOS used, the number of moles of silane to functionalize the NPs or MPs was calculated with a spreadsheet. The assumptions incorporated into the spreadsheet are as follows: the density of silica is 2.0 g/mL, each silane molecules functionalized on the surface of a NP covers 2 nm² of the surface area and the TEOS is 100% converted into silica. The spreadsheet calculates the surface area, volume and weight per particle, the number of particles in the mixture and the total NP surface area in solution. From this, the number of moles of silane required to functionalize the NPs is calculated. Using the molecular weight of the silane, the volume of silane can then be calculated. For example, 100 mL of a 100 nm NP synthesis preparation solution with a particle size of 100 nm and a silane 179 g/mol gives a volume of 1.42 μ L silane required to functionalize the NPs.

Characterization.

Dynamic Light Scattering (DLS) data was obtained using a Malvern Zetasizer Nano-S. SEM was carried out using a Hitachi S-4880 FE-SEM operating at 5-15 kV. TEM images were obtained using an Hitachi HF-3300.

ACKNOWLEDGEMENTS

CIHR and NSERC for funding of this project. NSERC and AIF for scholarship funding. Dr. Vincent Wright for his substantial work on this project including the refinement of fluorophore inclusion in the nanoparticles. Dr. Lori West, Dr. Jeyakanthan Mylvaganam and Dr. Esme Dijke for obtaining the flow cytometry results. Amy Tekrony for the zetapotential measurements and images of nanoparticles in chicken embryos. Dr. Sean McClure for the TEM imaging. Jeffrey Murphy for the pictures of magnetic NPs. The University of Alberta Chemistry Department's Analytical and Instrumentation Laboratory for fluorescence spectra.

REFERENCES

1. Tan, W.; Wang, K.; He, X.; Zhao, X.; Drake, T.; Wang, L.; Bagwe, R., *Med. Res. Rev.* **2004**, *24* (5), 621-638.
2. Gao, J.; Gu, H.; Xu, B., *Accounts Chem. Res.* **2009**, *42* (8), 1097-1107.
3. Jana, N.; Earhart, C.; Ying, J., *Chem. Mater.* **2007**, *19* (21), 5074-5082.
4. Bagwe, R.; Hilliard, L.; Tan, W., *Langmuir* **2006**, *22* (9), 4357-4362.
5. Kumar, R.; Roy, I.; Ohulchanskyy, T.; Vathy, L.; Bergey, E.; Sajjad, M.; Prasad, P., *ACS Nano* **2010**, *4* (2), 699-708.
6. Montet, X.; Montet-Abou, K.; Reynolds, F.; Weissleder, R.; Josephson, L., *Neoplasia* **2006**, *8* (3), 214-222.
7. Chang, E.; Thekkekk, N.; Yu, W.; Colvin, V.; Drezek, R., *Small* **2006**, *2* (12), 1412-1417.
8. Urata, C.; Aoyama, Y.; Tonegawa, A.; Yamauchi, Y.; Kuroda, K., *Chem. Commun.* **2009**, *2009* (34), 5094-5096.
9. Nakamura, M.; Ishimura, K., *Langmuir* **2008**, *24* (9), 5099-5108.
10. Mumin, A.; Barrett, J. W.; Dekaban, G. A.; Zhang, J., *J. Colloid Interface Sci.* **2011**, *353* (1), 156-162.
11. Mohanraj, V.; Chen, Y., *Trop. J. Pharm. Res.* **2006**, *5* (1), 561-573.
12. Kim, Y.-J.; Ha, S.-W.; Jeon, S.-M.; Yoo, D.; Chun, S.-H.; Sohn, B.-H.; Lee, J.-K., *Langmuir* **2010**, *26* (10), 7555-7560.
13. Vogt, C.; Toprak, M.; Shi, J.; Torres, N.; Fadeel, B.; Laurent, S.; Bridot, J.-L.; Muller, R.; Muhammed, M., *Mater. Res. Soc. Symp. Proc.* **2009**, *1140*, 209-214.
14. Ma, D.; Guan, J.; Normandin, F.; Denomme, S.; Enright, G.; Veres, T.; Simard, B., *Chem. Mater.* **2006**, *18* (7), 1920-1927.
15. Nagao, D.; Yokoyama, M.; Saeki, S.; Kobayashi, Y.; Konno, M., *Colloid Polym. Sci.* **2008**, *286* (8-9), 959-964.
16. Lin, Y.-S.; Haynes, C., *Chem. Mater.* **2009**, *21* (17), 3979-3986.
17. Kim, J.; Yoon, T.-J.; Yu, K.; Kim, B.; Park, S.; Kim, H.; Lee, K.; Park, S.; Lee, J.-K.; Cho, M., *Toxicol. Sci.* **2006**, *89* (1), 338-347.

18. Choi, J.; Kim, J.; Lee, Y.; Kim, I.; Park, Y.; Hur, N., *Chem. Commun.* **2007**, *2007* (16), 1644-1646.
19. Ren, C.; Li, J.; Liu, Q.; Ren, J.; Chen, X.; Hu, Z.; Hue, D., *Nanoscale Res. Lett.* **2008**, *3* (12), 496-501.
20. Zhang, J.; Li, J.; Razavi, F. S.; Mumin, A. M., *J. Nanopart. Res.* **2011**, *13*, 1909-1916.
21. Rao, K.; El-Hami, K.; Kodaki, T.; Matsushige, K.; Makino, K., *J. Colloid Interface Sci.* **2005**, *289* (1), 125-131.
22. Shin, J.; Metzger, S.; Schoenfish, M., *J. Am. Chem. Soc.* **2007**, *129* (15), 4612-4619.
23. Lu, C.-W.; Hung, Y.; Hsiao, J. K.; Yao, M.; Chung, T.-H.; Lin, Y.-S.; Wu, S.-H.; Hsu, S.-C.; Liu, H.-M.; Mou, C.-Y.; Yang, C.-S.; Huang, D.-M.; Chen, Y.-C., *Nano Letters* **2007**, *7* (1), 149-154.
24. He, X.; Nie, H.; Wang, K.; Tan, W.; Wu, X.; Zhang, P., *Anal. Chem.* **2008**, *80* (24), 9597-9603.
25. Ha, S.-W.; Camalier, C.; Jr., G. B.; Lee, J.-K., *Chem. Commun.* **2009**, (20), 2881-2883.
26. Ma, D.; Kell, A.; Tan, S.; Jakubek, Z.; Simard, B., *J. Phys. Chem. C* **2009**, *113* (36), 15974-15981.
27. Du, X.; He, J., *Langmuir* **2010**, *26* (12), 10057-10062.
28. He, R.; You, X.; Shao, J.; Gao, F.; Pan, B.; Cui, D., *Nanotechnology* **2007**, *18* (31), 315601.
29. Barnes, C.; Elsaesser, A.; Arkusz, J.; Smok, A.; Palus, J.; Lesniak, A.; Salvati, A.; Hanrahan, J.; Jong, W. d.; Dziubaltowska, E.; Stepnik, M.; Rydzynski, K.; McKerr, G.; Lynch, I.; Dawson, K.; Howard, C., *Nano Lett.* **2008**, *8* (9), 3069-3074.
30. Choi, J.; Burns, A.; Williams, R.; Zhou, Z.; Flasken-Nikitin, A.; Zipfel, W.; Wiesner, U.; Nikitin, A., *J. Biomed. Opt.* **2007**, *12* (6), 064007-1 - 064007-11.
31. Burns, A.; Ow, H.; Wiesner, U., *Chem. Soc. Rev.* **2006**, *35* (11), 1028-1042.

32. Thomassen, L.; Aerts, A.; Rabolli, V.; Lison, D.; Gonzalez, L.; Kirsch-Volders, M.; Napierska, D.; Hoet, P.; Kirschhock, C.; Martens, J., *Langmuir* **2010**, *26* (1), 328-335.
33. Insin, N.; Tracy, J.; Lee, H.; Zimmer, J.; Westervelt, R.; Bawendi, M., *ACS Nano* **2008**, *2* (2), 197-202.
34. Bareiss, B.; Ghorbani, M.; Li, F.; Blake, J. A.; Scaiano, J. C.; Zhang, J.; Deng, C.; Merrett, K.; Harden, J. L.; Diaz-Mitoma, F.; Griffith, M., *TOTERMJ* **2010**, *3*, 10-17.
35. Tallury, P.; Malhotra, A.; Byrne, L.; Santra, S., *Adv. Drug Delivery Rev.* **2010**, *62* (4-5), 424-437.
36. Gupta, R.; Kumar, A., *Biomed. Mater.* **2008**, *3* (3), 034005.
37. Liu, S.; Zhang, H.-L.; Liu, T.-C.; Liu, B.; Cao, Y.-C.; Huang, Z.-L.; Zhao, Y.-D., *J. Biomed. Mater. Res. A* **2007**, *80* (3), 752-757.
38. Nann, T.; Mulvaney, P., *Angew. Chem. Int. Ed.* **2004**, *43* (40), 5393-5396.
39. Chen, L.; Zhang, J., *Sci. Adv. Mater.* **2012**, *4* (8), 859-862.
40. Blaaderen, A. V.; Vrij, A., *J. Colloid Interface Sci.* **1993**, *156* (1), 1-18.
41. Liong, M.; Lu, J.; Kovochich, M.; Xia, T.; Ruehm, S.; Nel, A.; Tamanoi, F.; Zink, J., *ACS Nano* **2008**, *2* (5), 889-896.
42. Nakabayashi, H.; Yamada, A.; Noba, M.; Kobayashi, Y.; Konno, M.; Nagao, D., *Langmuir* **2010**, *26* (10), 7512-7515.
43. Stöber, W.; Fink, A.; Bohn, E., *J. Colloid Interface Sci.* **1968**, *26* (1), 62-69.
44. Wang, X.-D.; Shen, Z.-X.; Sang, T.; Cheng, X.-B.; Li, M.-F.; Chen, L.-Y.; Wang, Z.-S., *J. Colloid Interface Sci.* **2010**, *341* (1), 23-29.
45. Blaaderen, A. V.; Geest, J. V.; Vrij, A., *J. Colloid Interface Sci.* **1992**, *154* (2), 481-501.
46. Bogush, G.; Tracy, M.; IV, C. Z., *J. Non-Cryst. Solids* **1988**, *104* (1), 95-106.
47. Yokoi, T.; Wakabayashi, J.; Otsuka, Y.; Fan, W.; Iwama, M.; Watanabe, R.; Aramaki, K.; Shimojima, A.; Tatsumi, T.; Okubo, T., *Chem. Mater.* **2009**, *21* (15), 3719-3729.

48. Zhang, D.; Wu, Z.; Xu, J.; Liang, J.; Li, J.; Yang, W., *Langmuir* **2010**, *26* (9), 6657-6662.
49. Ow, H.; Larson, D.; Srivastava, M.; Baird, B.; Webb, W.; Wiesner, U., *Nano Lett.* **2005**, *5* (1), 113-117.
50. Ge, J.; Hu, Y.; Biasini, M.; Dong, C.; Guo, J.; Beyermann, W.; Yin, Y., *Chem. Eur. J.* **2007**, *13* (25), 7153-7161.
51. Matsumoto, H.; Nagao, D.; Konno, M., *Langmuir* **2010**, *226* (6), 4207-4211.
52. Zhang, J.; Srivastava, R.; Misra, R., *Langmuir* **2007**, *23* (11), 6342-6351.
53. Yu, W.; Falkner, J.; Yavuz, C.; Colvin, V., *Chem. Commun.* **2004**, (20), 2306-2307.
54. Yang, D.; Hu, J.; Fu, S., *J. Phys. Chem. C* **2009**, *113* (18), 7646-7651.
55. Zhang, J.; Hodge, W.; Hutnick, C.; Wang, X., *J. Diabetes Sci. Technol.* **2011**, *5* (1), 166-172.
56. Zhang, J.; Lan, C. Q.; Post, M.; Simard, B.; Deslandes, Y.; Hsieh, T. H., *Cancer Genomics Proteomics* **2006**, *3* (3-4), 147-158.
57. Nakamura, M.; Shono, M.; Ishimura, K., *Anal. Chem.* **2007**, *79* (17), 6507-6514.
58. Burns, A.; Vider, J.; Ow, H.; Herz, E.; Penate-Medina, O.; Baumgart, M.; Larson, S.; Wiesner, U.; Bradbury, M., *Nano Lett.* **2009**, *9* (1), 442-448.
59. Yu, W.; Chang, E.; Drezek, R.; Colvin, V., *Biochem. Biophys. Res. Commun.* **2006**, *348* (3), 781-786.
60. Senarath-Yapa, M.; Phimphivong, S.; Coym, J.; Wirth, M.; Aspinwall, C.; Saavedra, S., *Langmuir* **2007**, *23* (25), 12624-12633.
61. Alberto, G.; Miletto, I.; Viscardi, G.; Caputo, G.; Latterini, L.; Coluccia, S.; Martra, G., *J. Phys. Chem. C* **2009**, *113* (50), 21048-21053.
62. Palma, A.; Tasiar, M.; Frimannsson, D.; Vu, T.; Meallet-Renault, R.; O'Shea, D., *Org. Lett.* **2009**, *11* (16), 3638-3641.
63. Herz, E.; Burns, A.; Bonner, D.; Wiesner, U., *Macromol. Rapid Commun.* **2009**, *30* (22), 1907-1910.

64. Larson, D. R.; Ow, H.; Vishwasrao, H. D.; Heikal, A. A.; Wiesner, U.; Webb, W. W., *Chem. Mater.* **2008**, *20* (8), 2677-2684.
65. Fauchner, L.; Guay-Begin, A. A.; Lagueux, J.; Cote, M. F.; Petitclerc, E.; Fortin, M. A., *Contrast Media Mol. I.* **2011**, *6* (4), 209-218.
66. Roy, I.; Ohulchansyy, T.; Pudavar, H.; Bergey, E.; Oseroff, A.; Morgan, J.; Dougherty, T.; Prasad, P., *J. Am. Chem. Soc.* **2003**, *125* (26), 7860-7865.
67. Lee, J.; Lee, Y.; Youn, J.; Na, H.; Yu, T.; Kim, H.; Lee, S.-M.; Koo, Y.-M.; Kwak, J.; Park, H.; Chang, H.; Hwang, M.; Park, J.-G.; Kim, J.; Hyeon, T., *Small* **2008**, *4* (1), 143-152.

CHAPTER 5 – FUNCTIONALIZATION OF SILICA NANOPARTICLES AND MICROPARTICLES

INTRODUCTION

Composite materials are extremely attractive for the opportunity of tailoring and incorporating a variety of properties that may otherwise be impossible to achieve.(1-5) For example, most nanobiotechnologies, from diagnostics to pharmaceuticals, can benefit from advances in composite materials.(2,5-11) Composite materials containing biomolecules, such as carbohydrates, are particularly interesting for the possibility of creating biomimetic surfaces, but for such endeavours, the surface composition is critically important.(12-15) Carbohydrates are involved in a number of different biological processes and their effective and efficient immobilization on surfaces is necessary in order to fabricate successful composite materials.(10-14,16-22)

Nanoparticles (NPs) and microparticles (MPs) show great promise in biomedical applications.(10,11) They have shown benefits such as high surface area, enhanced chemical stability, and enhanced reactivity of surface moieties that can be utilized for the purpose of immunoassays.(1,6,7,10,20) In order to utilize the properties of NPs, surface modification of the NPs is necessary.(1,2,6,9) The most common type of nanomaterial used for biomolecule attachment is gold NPs.(10,17) Gold is attractive for its biocompatibility and the surface plasmon resonance of gold NPs allows their use as probes, or fluorophores can also be immobilized on them.(6,12,23-26) In particular, gold NPs have shown enormous promise in biomolecule immobilization, of which thiol attachment has widely been used and are of particular interest for biodiagnostics.(4,6,8,10,23,27-31) This functionalization of gold NPs is demonstrated in Fig. 5.1i). However, ligand stability is crucial for nanoparticle stability and thiol monolayers on gold are unstable under certain conditions, however, silica allows for more stable functionalizations.(3,32)

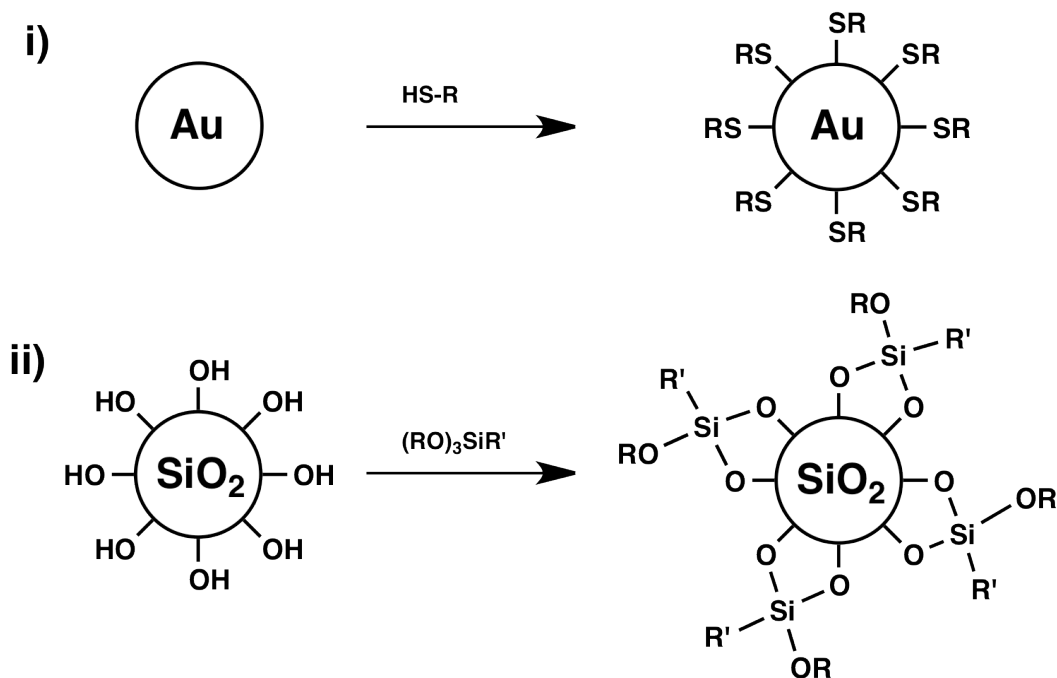


Figure 5.1. i) Functionalization of a variety of molecules, including fluorophores and biomolecules, have proven successful using thiol derivatives.(10,23,27,31) ii) Trialkoxysilanes derivatives of molecules, from polymers to biomolecules, have successfully functionalized silica nanoparticles.(1,4,19,33,34)

Silica nanoparticles are particularly appealing for their biocompatibility, and ease of synthesis and functionalization.(3,8,19,32,35-37) By incorporating dyes, these nanoparticles integrate detection capabilities necessary for immunoassays.(6,8,19,32,38,39) Direct surface modification of silica NPs with a number of different molecules, including biomolecules and polymer, has been effective using silanes, as demonstrated in Fig. 5.1ii.(1,4,6,8,15,19,33,34,40-43) Silane-functionalized surfaces are notable for the stability of the immobilized molecules.(18,32,43-46) In order to conserve the integrity of the biomaterials in biological environments, prevention of nonspecific protein binding is essential, an area where poly(ethylene glycol) (PEG) has shown promise.(7,23-25,47-50) Using PEG as a linker molecule for further functionalization has also previously been demonstrated offering covalent bonding of PEG and additional molecules.(13,21,23,51-53)

Immobilization of biomolecules requires both physical and chemical stability, as well as specific orientation of the biomolecule in order to preserve its selectivity and sensitivity for detection.(8,10,17,54,55) Chemical conjugation using linkers is an attractive method that fits these criteria, efficiently forming covalent bonds to specific sites under controlled conditions.(5,8,18,21,23,42,43,54-56) The immobilization of molecules, including biomolecules and polymers has proven successful on silica substrates, and amino-terminated thin films on silica have previously been used to immobilize biomolecules such as carbohydrates or proteins, as depicted in Fig. 5.2i.(5,8,18,20,21,54,56,57) Using *N*-hydroxysuccinimide (NHS) ester (Fig. 5.2ii) or *p*-nitrophenyl (PnP) derivatives (Fig. 5.2iii), biomolecules can efficiently be immobilized on amino-terminated substrates, while maintaining biological activity and stability.(10,12,17,18,23,51,54) Specifically, the reaction between PnP derivatives and amine functional groups forms a stable carbamate bond.(51)

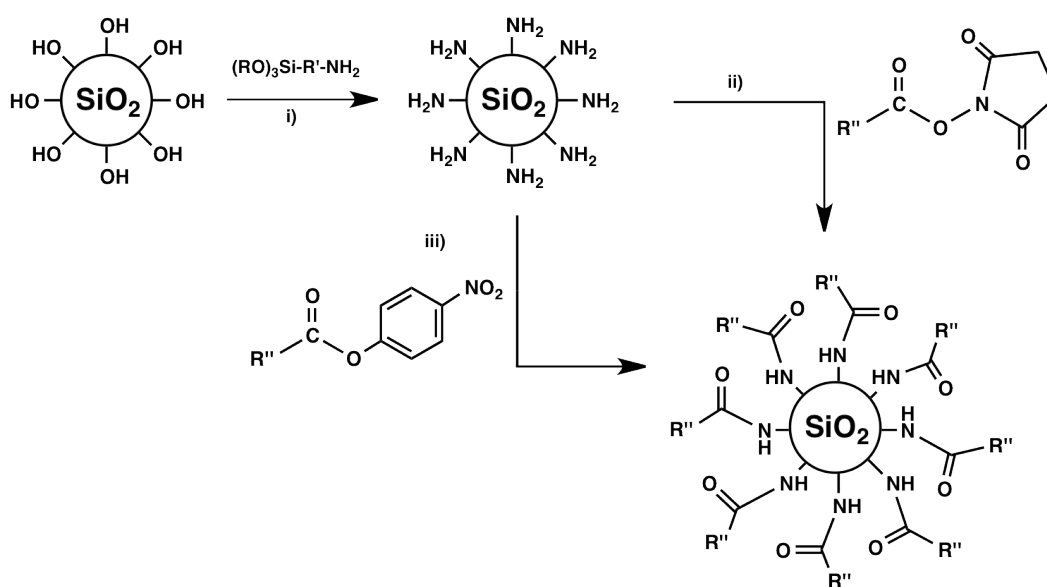


Figure 5.2. i) Amine-terminated silica nanoparticles can be synthesized using functional silanes.(5,12,20,54) These amine-terminated nanoparticles can subsequently be functionalized with desired biomolecules using i) NHS ester derivatives,(20,23,51,54) and ii) PnP derivatives.(51)

Immunoassays using fluorescent antibodies are widely used from research to clinical settings.(10,13,21,24,58) The specificity and affinity of antibodies toward biomolecules is highly desirable to produce sensitive, reliable and cost-effective immunoassays.(2,8,17,18,23,35,47) They have found use in determining biomolecule immobilization, which is of great interest for immunoassay diagnostics.(2,54)

Herein, silica NPs and MPs were functionalized with monosaccharides (MSs) and trisaccharides and tetrasaccharides (collectively TSs). Silane derivatives of saccharides and of PEG, and silane linker molecules were used to directly functionalize the NPs and MPs. Additionally, functionalization of PEG linker molecules was successfully performed using amine-terminated NPs and MPs. The PEG linker molecules were subsequently functionalized with TSs. These functionalizations were confirmed by fluorescent lectin and antibody detection.

RESULTS & DISCUSSION

A number of different architectures of nanoparticles (NPs) were selected for further functionalization. Three different syntheses were first used to functionalize the silica NPs with the monosaccharide (MS), shown in Fig. 5.3, along with PEG silane to reduce nonspecific protein binding. In the PnP synthesis, the NPs are first functionalized with a mixture of aminopropyltrimethoxy silane (APTMS) and poly(ethylene glycol) (PEG) trimethoxysilane. The amine functional groups on the NP are then reacted with the activated ester MS derivative in order to couple the MS to the NP. Alternatively, in the AS synthesis, the NPs are functionalized with a MS silane, similar to the method described in Chapter 3. Thiol-ene coupling was used to couple alkene derivatives of the MS to NPs functionalized with mercaptopropyltrimethoxysilane (MPTMS).

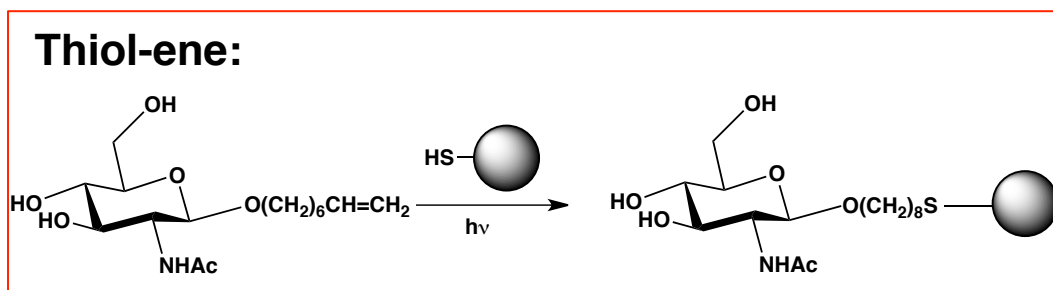
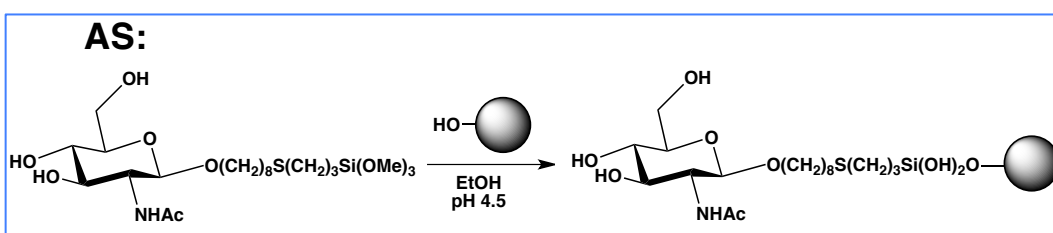
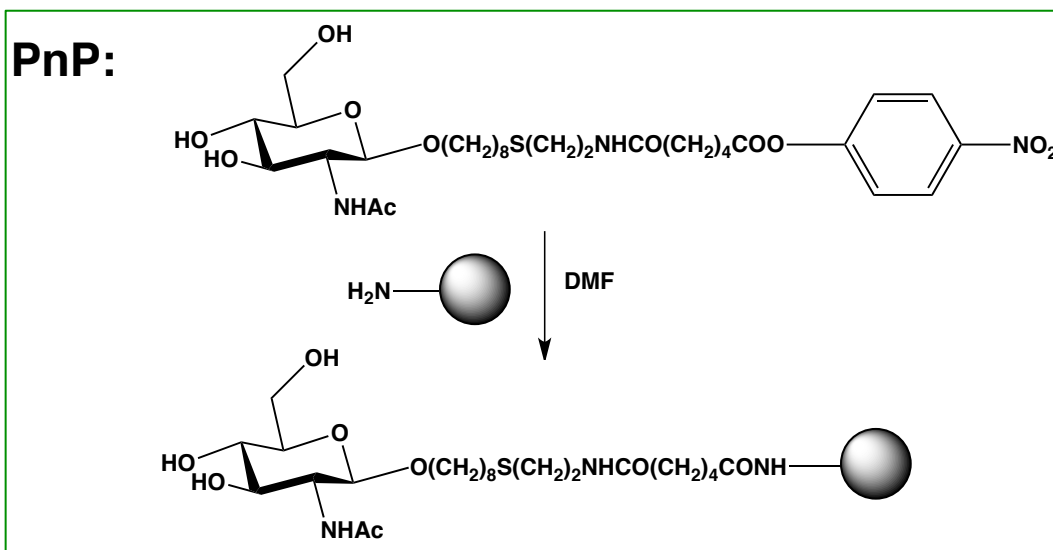


Figure 5.3. The synthesis of silica NPs functionalized with monosaccharide. The PnP synthesis involves the coupling of an activated ester to amine-functionalized NPs. The AS synthesis involves the alkoxy silane coupling to silica NPs. The Thiol-ene synthesis involves coupling an alkene derivative to thiol-functionalized NPs.

The MS used in these experiments is N-acetylglucosamine (GlcNAc) and using two fluorescein isothiocyanate (FITC) labelled lectins, it is possible to identify that there is monosaccharide attachment. Similar to the ELLA described previously, a wheat germ agglutinin (WGA), which specifically binds to GlcNAc, and a peanut agglutinin (PNA), which binds specifically to β -galactose, were used.⁽⁵⁹⁾ This detection method is outlined in Fig. 5.4

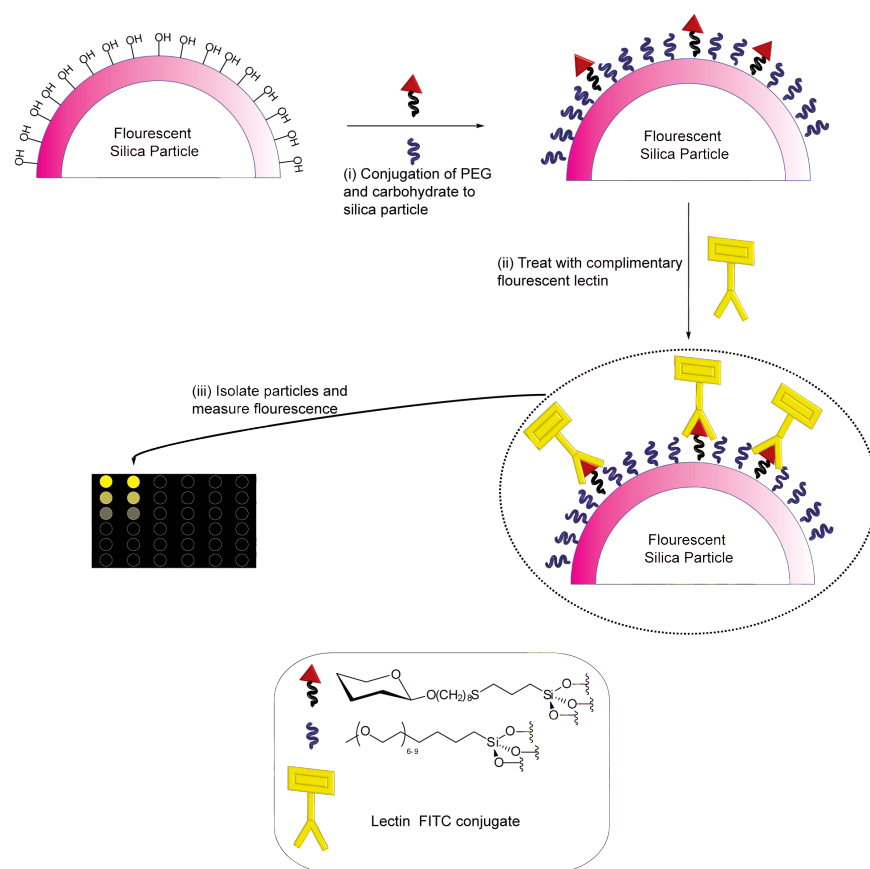


Figure 5.4. Schematic of silica NP surface functionalization via thiol-ene chemistry and detection of GlcNAc.

Of these fluorescent lectins, binding of WGA is selective for GlcNAc, whereas PNA is not. In these experiments, the silica NPs are not fluorescent. As expected, the WGA lectin fluorescence was detected in the silica NPs functionalized with GlcNAc in both the alkoxy silane (AS) and the activated ester (PnP) syntheses. This confirms the presence of the MS attachment from both syntheses, shown in Fig. 5.5. The PNA showed no recognition of the GlcNAc, indicating that there is no nonspecific binding of the PNA lectin to GlcNAc. Additionally, neither of the 100% PEG functionalized NPs displayed a fluorescence signal. This indicates that there is no nonspecific binding of either the WGA or PNA lectins to PEG.

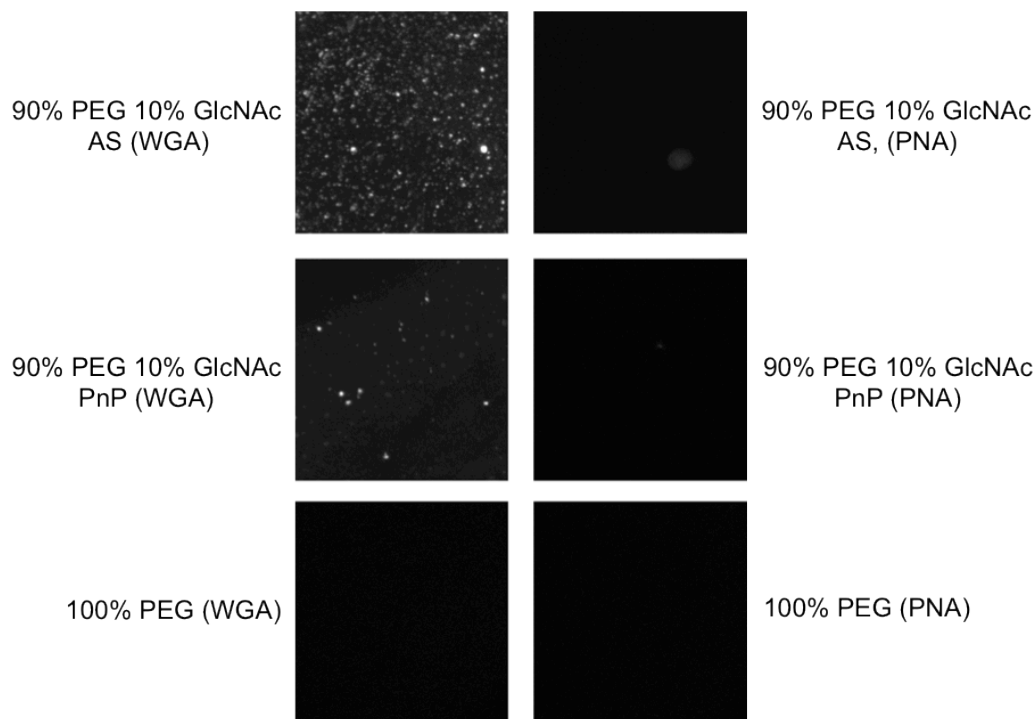


Figure 5.5. The fluorescence microscopy images of FITC labelled wheat germ agglutinin (WGA) and peanut agglutinin (PNA) binding to silica NPs functionalized with GlcNAc through PnP and AS syntheses.

Although GlcNAc attachment was confirmed in both the AS and PnP syntheses, the efficiency of MS attachment cannot be assessed using this method. The fluorescence signal from the AS attachment over PnP attachment of GlcNAc appears stronger in the images displayed in Fig. 5.5, which is confirmed by the fluorescence intensity displayed in Fig. 5.6. Many factors may have contributed to this increased fluorescence, however, it can be surmised that the fluorescence from both samples with GlcNAc treated with WGA was significantly above baseline fluorescence.

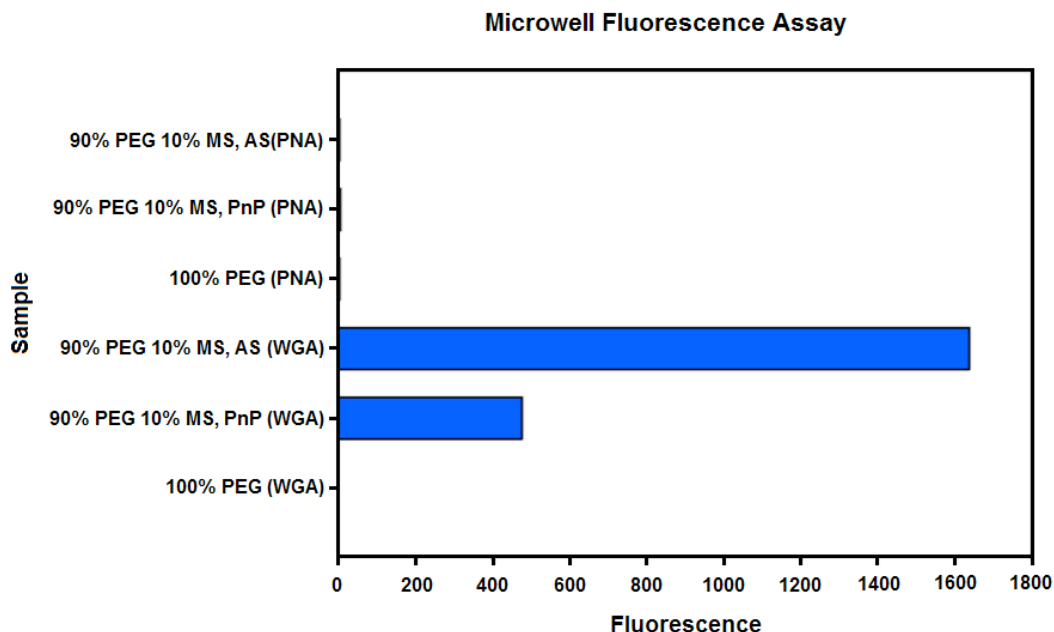


Figure 5.6. Fluorescence intensity obtained of fluorescent wheat germ agglutinin (WGA) and peanut agglutinin (PNA) binding to silica NPs functionalized with GlcNAc through PnP and AS syntheses.

In order to assess the silane functionalization of NPs, solution mixtures of PEG silane and mercaptopropyltrimethoxysilane (MPTMS) were used to functionalize 100 nm silica NPs. These mixed-silane NPs were characterized by high resolution XPS, shown in Fig. 5.7. From the C1s spectra, three peaks can be seen, at about 287.5, 285 and 283.5 eV. The peak at 283.5 eV is typical for carbon derived from C-C and C-H bonds and the higher binding energy peaks of carbon are associated with carbon bound to more electronegative elements such as the peak at 285 eV, associated with C-O. From Fig. 5.7(i), it can be seen that higher carbon content is associated with C-C and C-H in functionalization mixtures with higher concentrations of MPTMS. In contrast, higher concentrations of PEG silane contribute to a higher carbon content associated with C-O. These results are expected from the increased number of C-O bonds in PEG silane as opposed to MPTMS.

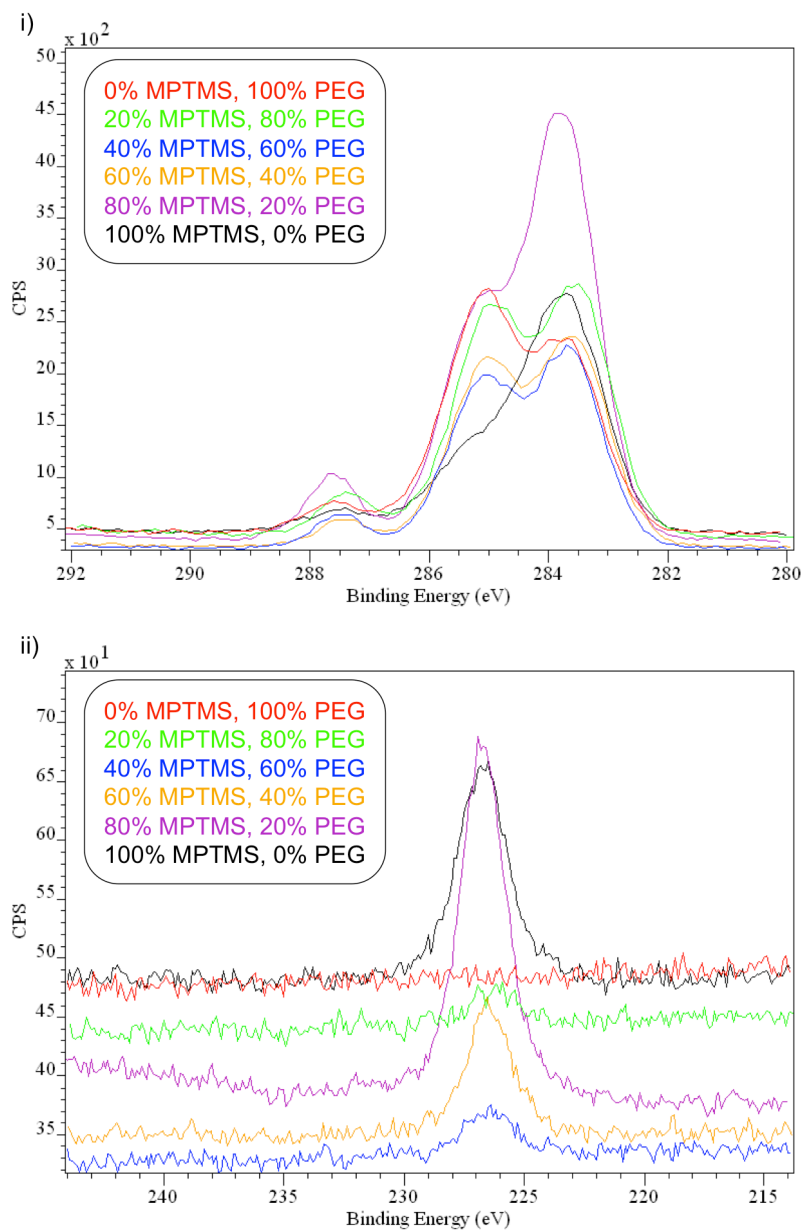


Figure 5.7. High resolution XPS of i) C1s and ii) S2s peaks for silica NPs functionalized with mixtures of MPTMS and PEG silane.

From the S2s spectra shown in Fig. 5.7ii), it is apparent that the sulfur content increases as the concentration of MPTMS in the silane mixtures increases. Since the PEG silane contains no sulfur, the only sulfur content should be derived from MPTMS, which indicates that as the MPTMS concentration is increased in solution, the MPTMS content on the functionalized NPs also increases. This is a

good indication that the silane mixture in solution roughly correlates to the silane mixture functionalized on the surface of the NPs.

It is well known that alkoxy silanes tend to form more branched clusters than layers under base conditions, and these NPs are prepared in basic conditions and subsequently functionalized in the same solution.(60). As such, it can be surmised that some of the saccharide silanes will react with each other over the silica NP surface, and therefore the silane may be inefficiently functionalize the surface. This is not a substantial concern in dealing with the MS, however is a much more significant concern when we move to functionalization of NPs with the TSs.

An additional method was attempted in order to reduce the amount of saccharide used in the AS synthesis. In this alternative procedure, the NPs were first functionalized with mixtures of MPTMS and PEG silane. Then, the GlcNAc alkene was added to the NP solution and the solution was irradiated, a variation on the method used in our stainless steel work outlined in previously Fig. 3.6. Although this variation on the procedure was possible for NP functionalization, this is impractical in the case of our stainless steel work. Since the NPs are in solution, they may move in solution such that all sides of each NP may be irradiated. However, with stainless steel stents, it is difficult to irradiate the interior of the stent, which is the preferable surface to functionalize. Unfortunately, this variation to the procedure had limited success as the GlcNAc was detected, however, the signal from fluorescent lectin binding was not as high as obtained from the AS synthesis depicted in Fig. 5.3. For more efficient and consistent attachment of silanes, the PnP synthesis was selected for both the TS and PEG functionalization of NPs.

The methodology for PnP attachment of molecules onto 1 μm fluorescent silica MPs is outlined in Fig. 5.8. The silica MPs were first amine-functionalized using APTMS followed by conjugation of PEG using an NHS ester derivative. The fluorenylmethoxycarbonyl (Fmoc) protecting group shown in Fig. 5.8 on the PEG

was then removed to provide a particle with a secondary free amine residue. The antigen can then be covalently attached, using an A type I antigen with an activated p-nitrophenyl (PnP) ester. It is widely accepted that trialkoxysilanes typically do not form pristine monolayers, but rather a networked siloxane layer.(61,62) To ensure that the APTMS functionalization is optimized, a semi-quantitative method is used by performing the reactions described in Fig. 5.8i-iii on MPs without incorporation of fluorophores, and by detection of the amount of Fmoc removed by UV-Vis spectroscopy.

Increased Fmoc detection was deemed the semi-quantitative benchmark to improving experimental factors since assays of the number of reactive amino-groups have proven useful in quantification for the immobilization biomolecules.(20,23) In order to standardize the functionalization, the MPs were centrifuged, and the solution was decanted, and replaced with fresh basic solution (referred to as B in Fig. 5.9, the same solution used for the reaction, without TEOS). This showed only minor increases in Fmoc over the original reaction solution, but gave more reproducible results. Additionally, doubling the amount of base in solution (referred to as DB in Fig. 5.9i), using an acidic instead of basic solution, and curing of samples offered no further increases in Fmoc detection. In the histograms of Fig. 5.9, the absorbance is relative, as it has been corrected for the weight of microparticles used.

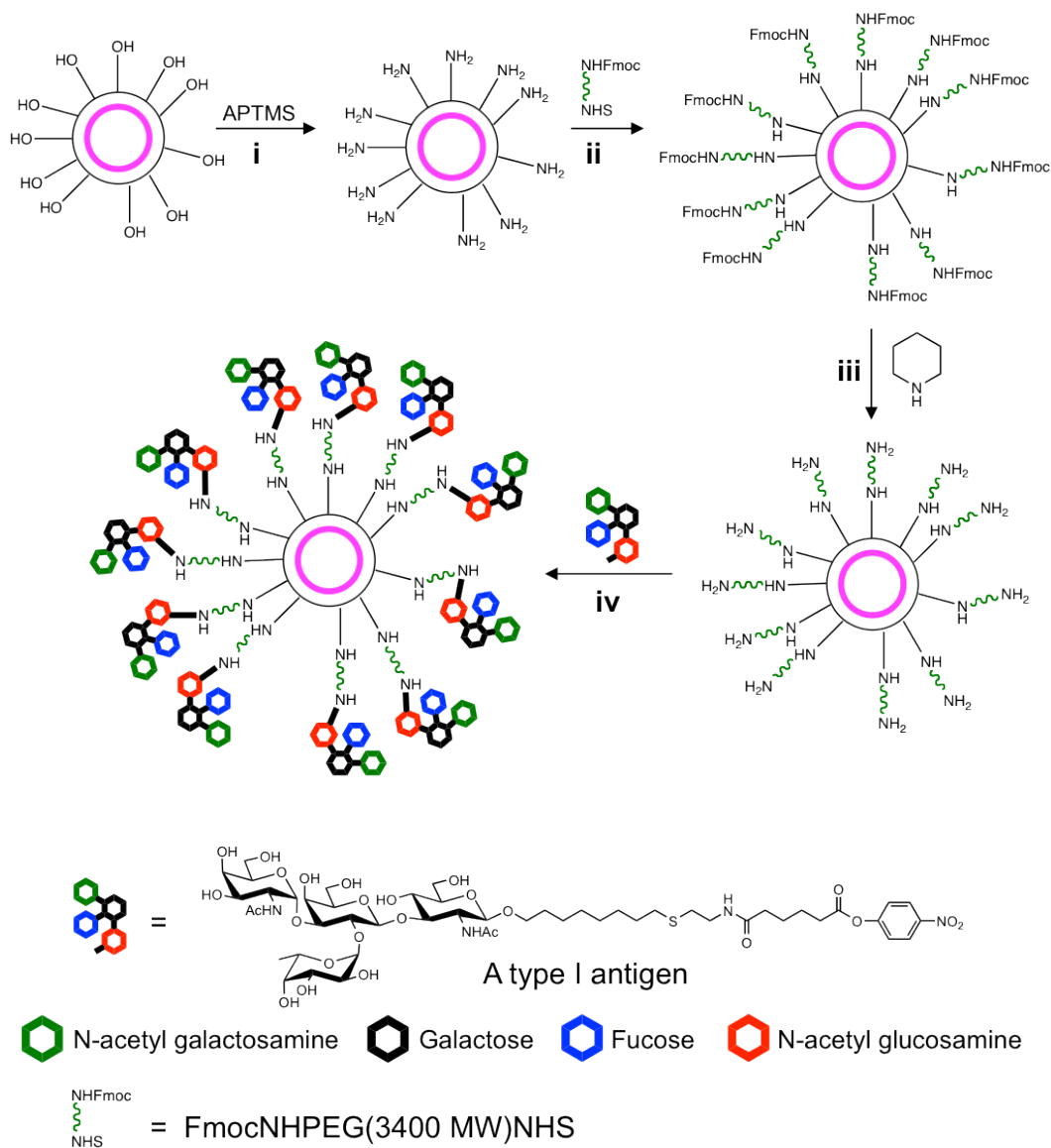
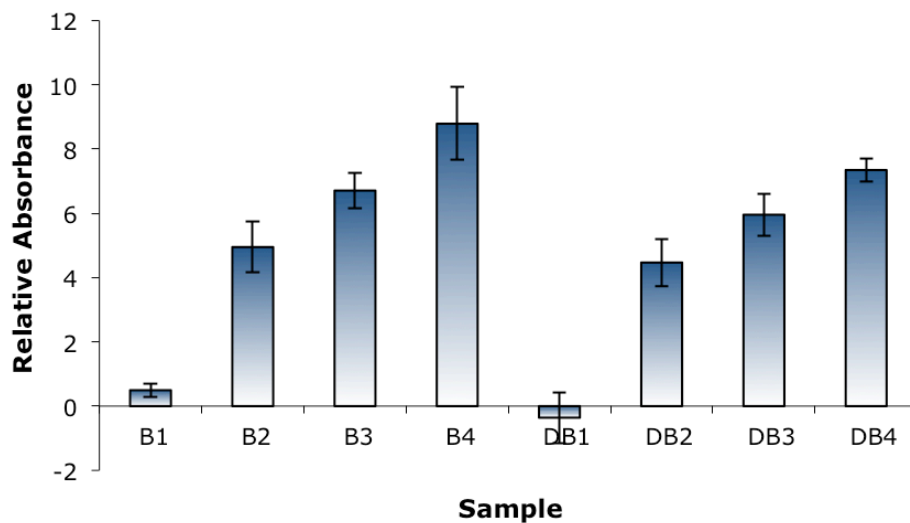


Figure 5.8. The MPs are i) amine functionalized, followed by ii) functionalization with PEG. iii) The Fmoc protecting group must be removed from the PEG before the iv) PnP derivative of the A type antigen can be bound to the MPs.

i) Semi-quantitative Analysis of APTMS Functionalization



ii) Semi-quantitative Analysis of APTMS Functionalization

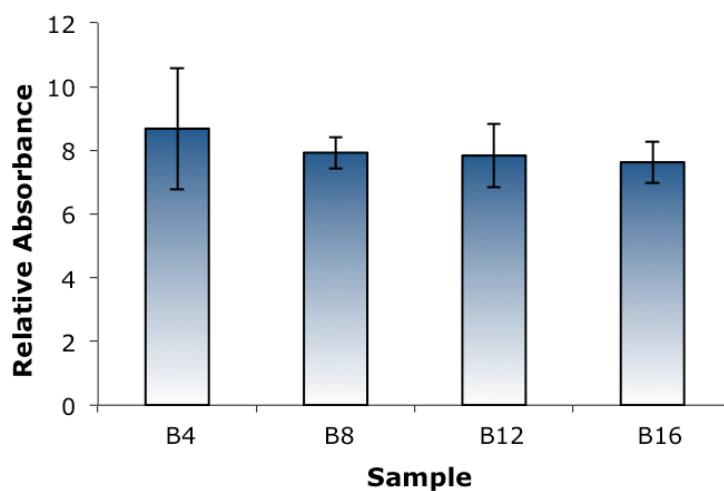


Figure 5.9. The results of the semi-quantitative detection of Fmoc obtained in order to maximize functionalization using different concentrations of APTMS and base.

The standard “1” APTMS functionalization of silica NPs was calculated using a spreadsheet with a number of assumptions incorporated. These assumptions include 100% conversion of TEOS to silica, a density of 2 g/mL of the produced silica NPs and the surface area of 2 nm² occupied by an attached silane. Although these assumptions may be naive, it offers a reasonable starting point. However,

increasing the APTMS 4-fold increases the amount of Fmoc detected as demonstrated in Figure 5.9ii. By increasing the amount of APTMS further (up to 16-fold), no more improvement was achieved, with the 16-fold increase yielding results within experimental error. The microparticle solutions were stirred during synthesis and continually in a round-bottom flask covered in parafilm until functionalization, which reduces evaporation of solvent, but does not eliminate this evaporation. As such, the 16-fold increase in APTMS was used as the convention in order to circumvent any issues of increased MP concentration in solution.

To confirm the A type I antigen expression on the MPs, the antibody detection outlined in Fig. 5.10 was used. The MPs were first treated with mouse anti-human A antigen IgM. These were then treated with goat anti-mouse IgM with an attached phycoerythrin (PE) fluorophore. This type of antigen detection can be performed for a number of different antigens with corresponding antibodies. The fluorophores attached to the antibody can then be detected using flow cytometry.

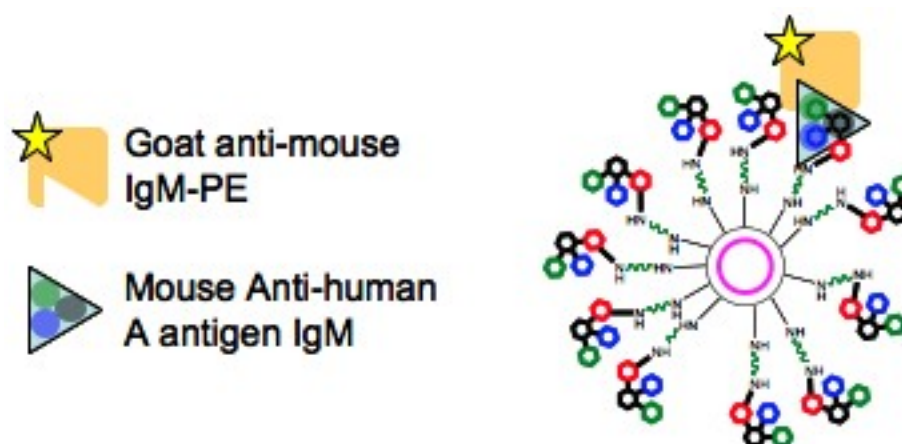


Figure 5.10. The detection of A antigen on MPs using antibodies.

Silica microparticles functionalized with PEG and the A, B, or H (the carbohydrate which represents O blood type) antigens were prepared and flow cytometry results obtained for A and B antigen-functionalized MPs (Fig. 5.11) confirm that the MPs were >99% positive for A and B antigens respectively. In

particular, the A type antigen has proven stable for up to one month - the >99% antigen detection has been confirmed for samples within one week and one month after functionalization. Additionally, the nonspecific binding of anti-B antibodies to A antigens was assessed and from the flow-cytometry results (Fig. 5.11i), it is evident that there is no nonspecific binding of anti-B antibodies to MPs functionalized with A antigens. From Fig. 5.11ii), however, a minor amount of nonspecific binding anti-A antibody was detected on MPs functionalized with B antigens. No nonspecific binding of the goat anti-mouse IgM antibody to either A or B antigen functionalized MPs was detected as the black dashed line in both Fig. 5.11i) and ii) is centred around zero.

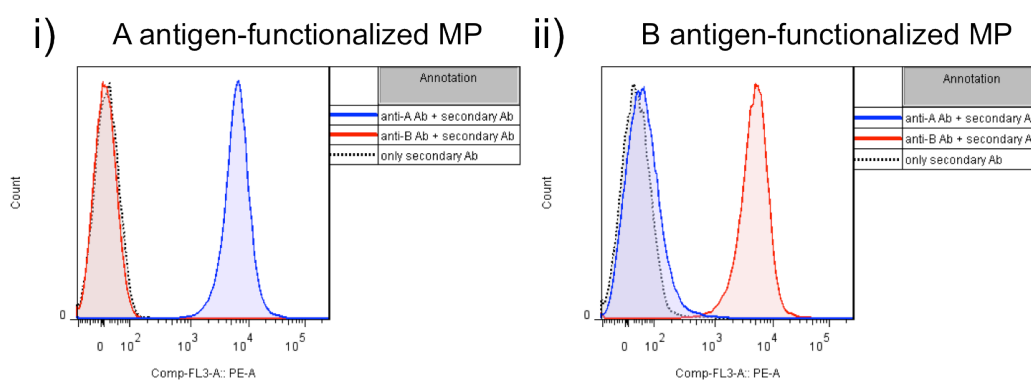


Figure 5.11. Flow cytometry detection of antibodies bound to i) A antigen and ii) B antigen.

In order to further assess the selectivity of the antibody detection, an antibody with an attached Alexa Fluor® 488 dye was used. The MPs tested had Alexa Fluor® 647 dye incorporated in a silica shell. In this way, both the MP and the antibody can be detected simultaneously. In Fig. 5.12, the fluorescence of the MPs appears on x-axis, and the fluorescence of the antibody y-axis. From the results obtained by flow cytometry, clearly different populations of functionalized MPs were isolated. Specifically, 100% acetylated (NHAc) as opposed to 100% A type functionalizations could be identified. This means that if the PEG functionalized MPs are acetylated instead of further functionalized with A type antigen, the

antibody will not bind to them. This confirms little nonspecific binding of anti-A antibodies to acetylated PEG functionalized MPs.

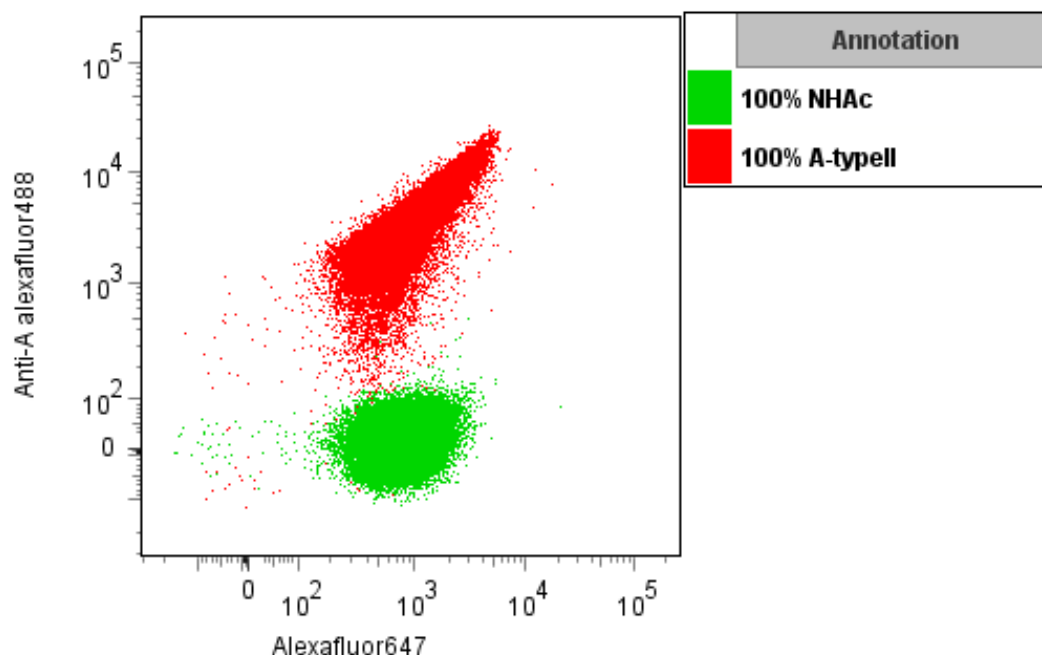


Figure 5.12. Flow cytometry results for A type II surface functionalization. The difference between A type II functionalized surface versus acetylated (NHAc) surface to the anti-A antibody can be clearly observed.

In order to assess the detection of A type antigen at different concentrations, the amine-terminated PEG was functionalized with mixtures of PEG and A type II derivatives. Again using an anti-A antibody with an attached Alexa Fluor® 488 dye, the A antigen can be detected when attached MPs, as shown in Fig 5.13. From this data, it is apparent that effective A type antigen detection can be accomplished even at a concentration of 10%. The signal does increase for the detection of 40% A type antigen, but levels off at higher concentrations. Interestingly, there appears to be less nonspecific binding of the anti-A antibody to the MPs when 10% of the linker PEG is acetylated (NHAc) instead of 100% PEGylated. This is apparent from the tail of the brown spectra for the 100% PEG sample from Fig. 5.13.

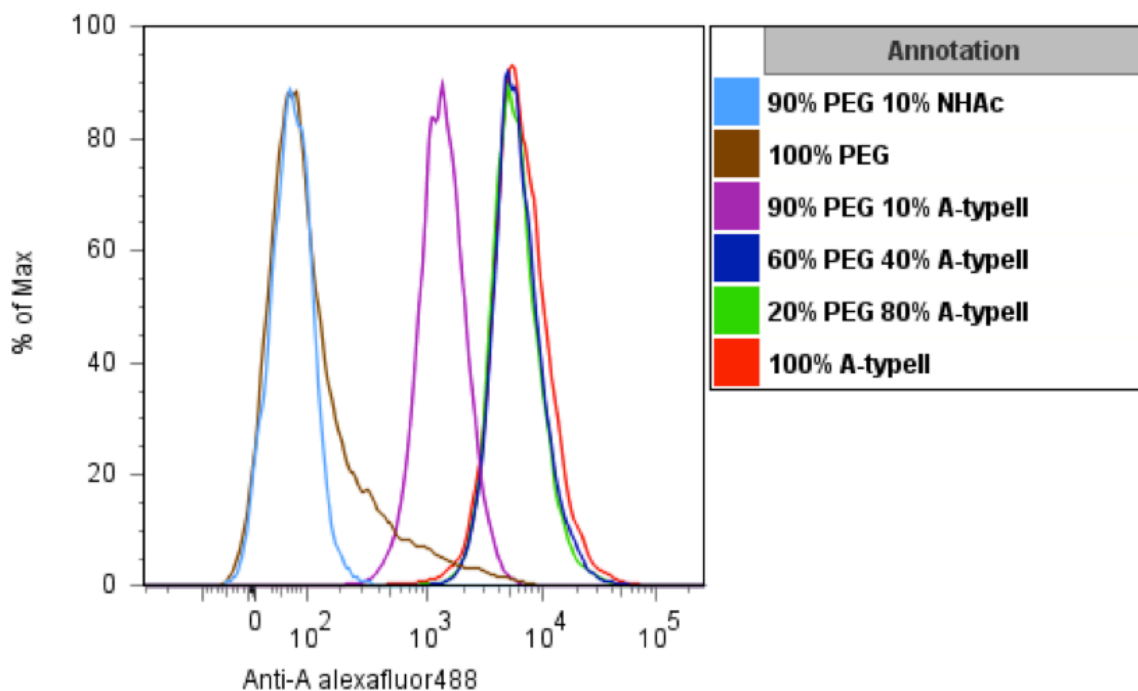


Figure 5.13. Flow cytometry results for A type II surface functionalization. Anti-A antibody was used labeled with Alexa Fluor® 488 dye. Again, these MPs had Alexa Fluor® 647 dye incorporated in them.

One key advantage to this work with the PnP linker, previously mentioned, is the ability to functionalize MPs and NPs conservatively with TSs. Specifically, the amine functionalized MPs used for testing in Fig. 5.13 required 1.2 mg A type II antigen, whereas 10 or more mg would be required in the functionalization of MPs with silanes. This demonstrates the more efficient use of the expensive TS with PnP attachment while Fig. 5.15 confirms its effective functionalization and the biological availability even at 10% A type II functionalization of the MPs.

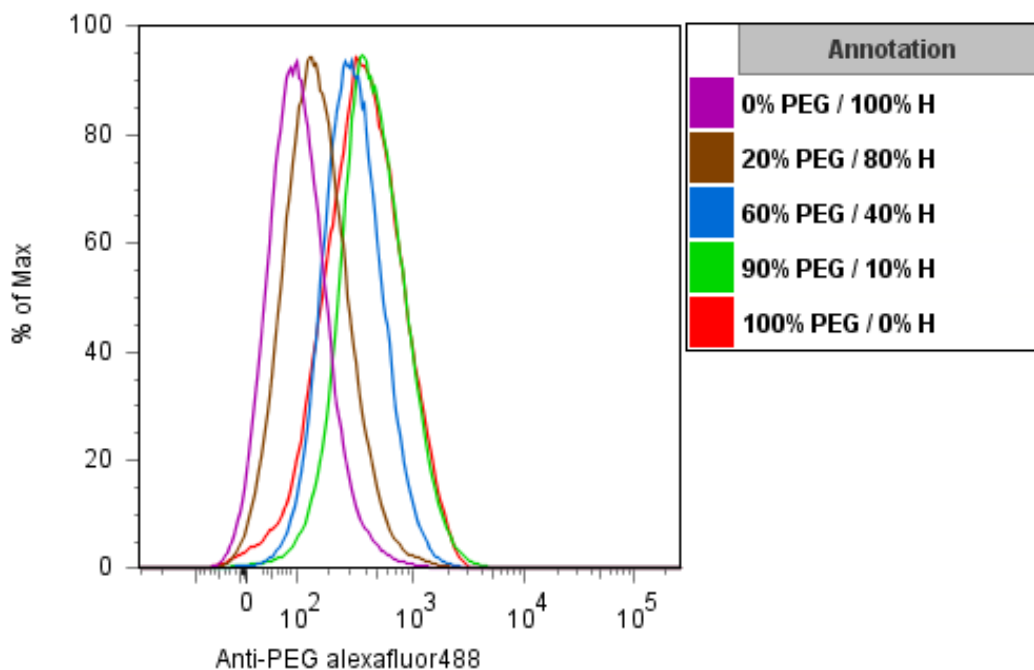


Figure 5.14. Flow cytometry results of fluorescent anti-PEG antibody.

To supplement the results obtained by the anti-A antigen detection, an anti-PEG antibody was used to detect the PEG. The flow cytometry results using the anti-PEG antibody with an attached Alexa Fluor® 488 dye are shown in Fig. 5.14. Here, the MPs are functionalized with mixtures of PEG and H antigens (the carbohydrate presented by O blood type cells). In this test, the increasing concentration of PEG from 0 to 100% complements increasing fluorescence. In this case, the fluorescence does not appear to level off above a particular concentration, as was the case with anti-A antibodies in Fig. 5.13.

CONCLUSIONS

Silanes were used to functionalize silica NPs and MPs. Specifically, monosaccharides (MSs) such as *N*-acetyl glucosamine (GlcNAc) were used to functionalize NPs as a model for more expensive tetrasaccharides (TSs), for which three different functionalization methods were developed. First, alkoxy silane derivatives of the MS were used to functionalize NPs. Second, mercaptopropyltrimethoxysilane (MPTMS) functionalized NPs were used to further functionalize with an alkene derivative of the MS under photoinitiation.

Third, aminopropyltrimethoxysilane (APTMS) was used as a linker molecule for further functionalization of a PnP derivative of the MS. Although all functionalizations were successful, as determined using a fluorescent lectin, the amine-PnP functionalization was selected for further study for its minimal loss of saccharide in the process.

MPs were functionalized first using an APTMS linker molecule and this functionalization was assessed and optimized for subsequent functionalization. These aminated MPs were then functionalized with a PEG linker molecule with an amine terminal group to then functionalized with TSs, as outlined in Fig 5.8. The presentation of TSs on fluorescent MP surface was characterized using fluorescent antibodies, and dual detection was confirmed by flow cytometry.

EXPERIMENTAL

Materials.

Acetic acid was purchased from EMD and used as received. 3-mercaptopropyl trimethoxysilane (MPTMS), and the FITC conjugated lectins (WGA-L4895 and PNA-L7381) were purchased from Aldrich and used without modification. 2-[methoxy(Polyethyleneoxy)propyl]-trimethoxysilane, and potassium chloride (99.999%) were purchased from Gelest Inc. (Morrisville, PA, U.S.A.) and used as received. 18 M Ω (Barnstead) water was freshly generated before use. Acetone was purchased from Fischer Scientific and used as received. Glacial acetic acid, sodium chloride (ACS grade), magnesium chloride hexahydrate (ACS grade), potassium chloride (ACS grade), calcium chloride (anhydrous), and sodium bicarbonate (ACS grade) were purchased from EMD and used as received. 100% ethanol was purchased from Commercial Alcohols and used as received. DAROCUR 1173 (2-hydroxy-2-methyl-1-phenyl- propan-1-one) was purchased from Ciba Speciality Chemicals.

Methods.

Preparation of phosphate buffer saline solution (PBS). For the biological assays, PBS at pH 7.4 was prepared. Phosphate buffer saline consists of a solution of 137 mM NaCl, 2.7 mM KCl, 100 mM Na₂HPO₄, 2 mM KH₂PO₄ in deionized water.

Alkoxysilane (AS) functionalization of NPs. Here, 10% MS, 90% PEG functionalization is described for simplicity. This procedure is similar to that used to functionalize stainless steel with MS silane. In a typical experiment, 2 mg of the MS silane (527 g/mol; 3.79×10^{-6} mol) was dissolved in 0.25 mL of 100% ethanol. To this solution, 17 μ L 2-[methoxy(polyethyleneoxy)propyl]-trimethoxysilane (19 mg, average MW = 550g/mol, 3.42×10^{-5}) was added. This solution of silanes was added to 35 mL of a \sim 100 mL 100 nm NP synthesis solution (prior to cleaning of the NPs, when the solution is still basic). The solution was allowed to react overnight. The NPs were cleaned by centrifuging and redispersing in 100% ethanol twice, followed by water twice, and one final time in PBS.

Thiol-ene coupling of MS to NPs. Here, 20% MPTMS, 80% PEG functionalization is described for simplicity. To \sim 100 mL 100 nm NP synthesis solution (prior to cleaning of the NPs, when the solution is still basic), 0.313 mL PEG and 31.5 μ L MPTMS is added. The solution was allowed to react overnight. The NPs were cleaned by centrifuging and redispersing in 100% ethanol three times, followed by redispersing in methanol. To this, 5 mg of the MS alkene derivative and 2 μ L DAROCUR 1173 was added. The solution was irradiated at 254 nm and 1200 W (16×75 W lamps) for 30 min. The solution was then centrifuged and redispersed in methanol twice, followed by 100% ethanol twice.

Functionalization of particles with APTMS. If the functionalization of particles followed the final addition in their synthesis by less than a week, then the functionalization is done directly. Otherwise, the particles are centrifuged, decanted and redispersed in their original solvent, their original solvent with

double the amount of ammonium hydroxide, or acidic solvent of ethanol, 18 M Ω -cm water and acetic acid in the proportions 90 : 5 : 5 mL. For example, a centrifuged sample microparticles are redispersed in the original solvent was redispersed in a solution of ethanol, ammonium hydroxide and 18 M Ω -cm water in the proportions of 340 : 10.6 : 38 mL. The size of the particles is obtained by averaging the size of a minimum of 150 particles as determined by SEM. From the average size, the surface area is calculated, and the amount of APTMS required is calculated. For smaller sample sizes, the APTMS is diluted in anhydrous ethanol in a glovebox. For example, to a 1.5 mL sample of microparticles with an average particle size of 935 nm, 84.8 μ L from a mixture of 10 μ L APTMS in 1 mL anhydrous ethanol after stirring for a minimum of 10 min. Following the addition of APTMS to the mixture of microparticles, the mixture is stirred overnight before cleaning up the particles through centrifugation. The cleaning typically involves centrifugation and resuspension in ethanol twice followed by twice in water.

Functionalization of particles with FmocPEGSVA. Each experiment was conducted in triplicate plus an additional sample was acetylated for comparison. For each sample, about 10-15 mg of freeze-dried 100 nm NPs or about 50-60 mg of freeze-dried MPs were weighed into 1.5 mL or 2 mL eppendorf tubes. The acetylated samples were suspended in 0.5 mL pyridine and 50 μ L of acetic anhydride, followed by rotation of the samples for 20 minutes and centrifugation and redispersion in DMA four times. All centrifugations are followed by removal of supernatant using a pipette. All samples were suspended in 0.5 mL DMA, and 100 μ L of 100 mg/mL FmocPEGSVA, and the samples were rotated overnight. All samples were centrifuged and resuspended twice in DMA followed by centrifugation and resuspension in acetonitrile twice.

Semi-quantitative determination of APTMS functionalization. To the particles functionalized with FmocPEGSVA suspended in DMA, 300 μ L of 20% piperidine in acetonitrile was added. The samples were left for 10 min for the

Fmoc to be removed from the PEG. The samples were then centrifuged, and the supernatant was removed by pipette and analyzed by UV-Vis. Particles were redispersed in 2 mM sodium azide, followed by centrifugation and redispersion once more in 2 mM sodium azide.

Functionalization of PEG linker on MPs with antigen. The FmocPEGsVA functionalized MPs (up to 65 mg dry weight) resuspended in acetonitrile are first centrifuged and resuspended in 500 μ L of 30% piperidine in acetonitrile and rotated for 10 minutes. All centrifugations are followed by removal of supernatant using a pipette. The particles were then centrifuged and resuspended in 1 mL acetonitrile twice. This centrifugation and resuspension was repeated twice with resuspension in 1 mL PBS, followed by a final resuspension in 0.5 mL PBS. To this, 1 mg PnP antigen in 100 mg DMA was added and mixed well. The MP solution was rotated for at least 24 hours. The particles were then centrifuged and resuspended in 1 mL DMA twice. The MP solution was then centrifuged and resuspended in 2 mM sodium azide in water twice and stored in the sodium azide until use, when it is centrifuged and resuspended in PBS directly before use.

Detection of antigens on functionalized fluorescent microparticles. 1 μ l of microparticles was mixed with 1 μ l of anti-A1, A2, A3 blood antigen antibody (cat# 133-A, Virogen), anti-B blood group antigen antibody (cat# 140-A, Virogen) or anti-H blood antigen antibody (cat#142-A, Virogen) in 100 μ l FACS staining buffer (FSB, PBS supplemented with 2% FBS (fetal bovine serum) and 0.1% sodium azide) and incubated at 4°C. After 30 min, the microparticles were centrifuged at 300 g for 2 min and supernatant was discarded. Microparticles were resuspended in 90 μ l FSB, mixed with 10 μ l goat anti-mouse IgM (μ) R-PE (1:8 dilution, cat# M31504, Invitrogen) and incubated for another 30 min at 4°C. After incubation, the microparticles were centrifuged at 300 g for 2 min and supernatant was discarded. The microparticles were washed with 200 μ l FSB and resuspended in 100 μ l FSB. Flow cytometric analysis was performed on the MACSQuant

Analyzer 10 (Miltenyi Biotec) and data analysis was done with FlowJo Software (version 7.6.5, Tree Star Inc.).

Characterization.

Nanoparticles characterized by XPS (Kratos Analytical, Axis-Ultra) were performed under high-vacuum conditions ($<10^{-8}$ Torr) using monochromatic Al KR with a photon energy of 1486.6 eV, in the Alberta Centre for Surface Engineering and Science (ACSES). The instrument was calibrated on the basis of the C 1s peak.

ACKNOWLEDGEMENTS

CIHR and NSERC for funding of this project. NSERC and AIF for scholarship funding. Dr. Lori Wesr, Dr. Jeyakanthan Mylvaganam and Dr. Esme Dijke for obtaining the flow cytometry results. Dr. Todd Lowary and Dr. Peter Meloncelli for their help with the functionalization studies, synthesis of the carbohydrates used and developing of the assays. Dr. Vincent Wright for his help with the MS functionalization studies. Dr. Christopher Cairo for obtaining fluorescence data obtained for the assays using GlcNAc functionalized NPs.

REFERENCES

1. Kim, Y.-J.; Ha, S.-W.; Jeon, S.-M.; Yoo, D.; Chun, S.-H.; Sohn, B.-H.; Lee, J.-K., *Langmuir* **2010**, *26* (10), 7555-7560.
2. Gao, J.; Gu, H.; Xu, B., *Accounts Chem. Res.* **2009**, *42* (8), 1097-1107.
3. Balamurugan, S.; Soto-Cantu, E.; Cueto, R.; Russo, P., *Macromolecules* **2010**, *43* (1), 62-70.
4. Gann, J.; Yan, M., *Langmuir* **2008**, *24* (10), 5319-5323.
5. Banet, P.; Marcotte, N.; Lerner, D.; Brunel, D., *Langmuir* **2008**, *24* (16), 9030-9037.
6. Tan, W.; Wang, K.; He, X.; Zhao, X.; Drake, T.; Wang, L.; Bagwe, R., *Med. Res. Rev.* **2004**, *24* (5), 621-638.
7. Mohanraj, V.; Chen, Y., *Trop. J. Pharm. Res.* **2006**, *5* (1), 561-573.

8. Tallury, P.; Malhotra, A.; Byrne, L.; Santra, S., *Adv. Drug Delivery Rev.* **2010**, *62* (4-5), 424-437.
9. Huang, X.; Zhuang, J.; Chen, D.; Liu, H.; Tang, F.; Yan, X.; Meng, X.; Zhang, L.; Ren, J., *Langmuir* **2009**, *25* (19), 11657-11663.
10. Wang, X.; Ramstrom, O.; Yan, M., *Adv. Mater.* **2010**, *22* (17), 1946-1953.
11. Shirahata, N.; Yonezawa, T.; Miura, Y.; Kobayashi, K.; Koumoto, K., *Langmuir* **2003**, *19* (22), 9107-9109.
12. Thygesen, M.; Sauer, J.; Jensen, K., *Chem. Eur. J.* **2009**, *15* (7), 1649-1660.
13. Pei, Y.; Yu, H.; Theurer, M.; Ammer, C.; Andre, S.; Gabius, H.-J.; Yan, M.; Ramstrom, O., *Anal. Chem.* **2007**, *79* (18), 6897-6902.
14. Leonard, D.; Chevolut, Y.; Bucher, O.; Haenni, W.; Sigrist, H.; Mathieu, H., *Surf. Interface Anal.* **1998**, *26* (11), 793-799.
15. Yan, M.; Ren, J., *Chem. Mater.* **2004**, *16* (9), 1627-1632.
16. Nakamae, K.; Miyata, T.; Ootsuki, N., *Macromol. Chem. Phys.* **1994**, *195* (7), 2663-2675.
17. Wang, X.; Ramstrom, O.; Yan, M., *J. Mater. Chem.* **2009**, *19* (47), 8944-8949.
18. Liu, L.-H.; Dietsch, H.; Schurtenberger, P.; Yan, M., *Bioconjugate Chem.* **2009**, *20* (7), 1349-1355.
19. Hatano, K.; Yamazaki, T.; Yoshino, K.; Ohyama, N.; Koyama, T.; Matsuoka, K.; Terunuma, D., *Tetrahedron Lett.* **2008**, *49* (39), 5593-5596.
20. Earhart, C.; Jana, N.; Erathodiyil, N.; Ying, J., *Langmuir* **2008**, *24* (12), 6215-6219.
21. Park, S.; Lee, M.-R.; Shin, I., *Chem. Commun.* **2008**, *44* (37), 4389-4399.
22. Davies, M.; Lynn, R.; Davis, S.; Hearn, J.; Watts, J.; Vickerman, J.; Paul, A., *Langmuir* **1993**, *9* (7), 1637-1645.
23. Maus, L.; Spatz, J.; Fiammengo, R., *Langmuir* **2009**, *25* (14), 7910-7917.
24. Xie, J.; Xu, C.; Kohler, N.; Hou, Y.; Sun, S., *Adv. Mater.* **2007**, *19* (20), 3163-3166.

25. Nel, A.; Madler, L.; Velegol, D.; Xia, T.; Hoek, E.; Somasundaran, P.; Klaessig, F.; Castranova, V.; Thompson, M., *Nat. Mater.* **2009**, *8* (7), 543-557.
26. Xie, C.; Xu, F.; Huang, X.; Dong, C.; Ren, J., *J. Am. Chem. Soc.* **2009**, *131* (35), 12763-12770.
27. Mahapatro, A.; Johnson, D. M.; Patel, D. N.; Feldman, M. D.; Ayon, A. A.; Agrawal, C. M., *Curr. Top. Med. Chem.* **2008**, *8* (4), 281-289.
28. Mahapatro, A.; Johnson, D. M.; Patel, D. N.; Feldman, M. D.; Ayon, A. A.; Agrawal, C. M., *Nanomed. Nanotechol. Biol. Med.* **2006**, *2* (3), 182-190.
29. Liong, M.; Lu, J.; Kovochich, M.; Xia, T.; Ruehm, S.; Nel, A.; Tamanoi, F.; Zink, J., *ACS Nano* **2008**, *2* (5), 889-896.
30. Fritz, M.; Hahner, G.; Spencer, N., *Langmuir* **1996**, *12* (25), 6074-6082.
31. Zhang, J.; Lan, C. Q.; Post, M.; Simard, B.; Deslandes, Y.; Hsieh, T. H., *Cancer Genomics Proteomics* **2006**, *3* (3-4), 147-158.
32. He, R.; You, X.; Shao, J.; Gao, F.; Pan, B.; Cui, D., *Nanotechnology* **2007**, *18* (31), 315601.
33. Larson, E.; Nielsen, T.; Wittenborn, T.; Birkedal, H.; Vorup-Jensen, T.; Howard, K.; Kjems, J., *ACS Nano* **2009**, *3* (7), 1947-1951.
34. Garcia, N.; Benito, E.; Guzman, J.; Francisco, R. d.; Tiemblo, P., *Langmuir* **2010**, *26* (8), 5499-5506.
35. Wang, Y.; Liu, B., *Langmuir* **2009**, *25* (21), 12787-12793.
36. Peng, J.; He, X.; Wang, K.; Tan, W.; Li, H.; Xing, X.; Wang, Y., *Nanomed. Nanotechol. Biol. Med.* **2006**, *2* (2), 113-120.
37. Mumin, A.; Barrett, J. W.; Dekaban, G. A.; Zhang, J., *J. Colloid Interface Sci.* **2011**, *353* (1), 156-162.
38. Nakamura, M.; Ishimura, K., *Langmuir* **2008**, *24* (9), 5099-5108.
39. Maat, J.; Regeling, R.; Yang, M.; Mullings, M.; Bent, S.; Zuilhof, H., *Langmuir* **2009**, *25* (19), 11592-11597.
40. Domingo, C.; Loste, E.; Fraile, J., *J. Supercrit. Fluids* **2006**, *37* (1), 72-86.
41. Kumar, R.; Roy, I.; Ohulchanskyy, T.; Vathy, L.; Bergey, E.; Sajjad, M.; Prasad, P., *ACS Nano* **2010**, *4* (2), 699-708.

42. Liu, L.; Engelhard, M.; Yan, M., *J. Am. Chem. Soc.* **2006**, *128* (43), 14067-14072.
43. Pleul, D.; Frenzel, R.; Eschner, M.; Simon, F., *Anal. Bioanal. Chem.* **2003**, *375* (8), 1276-1281.
44. Sinapi, F.; Naji, A.; Delhalle, J.; Mekhalif, Z., *Surf. Interface Anal.* **2004**, *36* (11), 1484-1490.
45. Kaufmann, C. R.; Mani, G.; Marton, D.; Johnson, D. M.; Agrawal, C. M., *Biomed. Mater.* **2010**, *5* (2), 1-10.
46. Sundararajan, G.; Ooij, W. v., *Surf. Eng.* **2000**, *16* (4), 315-320.
47. Hoshino, Y.; Koide, H.; Urakami, T.; Kanazawa, H.; Kodama, T.; Oku, N.; Shea, K., *J. Am. Chem. Soc.* **2010**, *132* (19), 6644-6645.
48. Lundberg, P.; Bruin, A.; Klijnstra, J.; Nystrom, A.; Johansson, M.; Malkoch, M.; Hult, A., *ACS Appl. Mater. Interfaces* **2010**, *2* (3), 903-912.
49. *Engineering Materials for Biomedical Applications*. 1st ed.; World Scientific Publishing Co. Pte. Ltd.: Singapore, 2004; Vol. 1, p 352.
50. Sharma, V.; Dhayal, M.; Govind; Shivaprasad, S.; Jain, S., *Vacuum* **2007**, *81* (9), 1094-1100.
51. Shi, M.; Lu, J.; Shoichet, M., *J. Mater. Chem.* **2009**, *19* (31), 5485-5498.
52. Sharma, S.; Johnson, R.; Desai, T., *Biosens. and Bioelectron.* **2004**, *20* (2), 227-239.
53. Brough, B.; Christman, K.; Wong, T.; Kolodzuej, C.; Forbes, J.; Wang, K.; Maynard, H.; Ho, C.-M., *Soft Matter* **2007**, *3* (5), 541-546.
54. Kim, J.; Cho, J.; Seidler, P.; Kurland, N.; Yadavalli, V., *Langmuir* **2010**, *26* (4), 2599-2608.
55. Huang, L.; Dolai, S.; Raja, K.; Kruk, M., *Langmuir* **2010**, *26* (4), 2688-2693.
56. Al-Bataineh, S.; Luginbuehl, R.; Textor, M.; Yan, M., *Langmuir* **2009**, *25* (13), 7432-7437.
57. Pitt, W. G.; Morris, R. N.; Mason, M. L.; Hall, M. W.; Luo, Y.; Prestwich, G. D., *J. Biomed. Mater. Res. A* **2004**, *68A* (1), 95-106.

58. Ji, T.; Muenker, C.; Papineni, R.; Harder, J.; Vizard, D.; Mclaughlin, W., *Bioconjugate Chem.* **2010**, *21* (3), 427-535.
59. Slaney, A.; Wright, V.; Meloncelli, P.; Harris, K.; West, L.; Lowary, T.; Buriak, J., *ACS Appl. Mater. Interfaces* **2011**, *3* (5), 1601-1612.
60. Fahlmen, B. D., *Materials Chemistry*. Springer-Verlag: New York, 2008; Vol. 2nd edition, p 468.
61. Matinlinna, J. P.; Ozcan, M.; Lassila, L. V. J.; Vallittu, P. K., *Dent. Mater.* **2004**, *20* (9), 804-813.
62. van Ooij, W. J.; Zhu, D.; Stacy, M.; Seth, A.; Mugada, T.; Gandhi, J.; Puomi, P., *Tsinghua Sci. Technol.* **2005**, *10* (6), 639-664.

CHAPTER 6 – CONCLUSIONS

Organ transplant is the necessary treatment for many lethal conditions including congenital cardiac malformations and cardiomyopathies in infants. Waitlists for these life-saving surgeries are long, availability of compatible donor organs is variable, and patients on them may be very ill, all of which can lead to the death of patients before successful organ transplants can be performed. Even after transplant surgery, patients must take immunosuppressive drugs with life-threatening side effects.

In organ transplant, ABO incompatibility, derived from the ABO polysaccharide antigens presented on tissue surfaces, seems an insurmountable barrier.(1-3) The antibodies present in human blood plasma can lead to hyperacute rejection of organs and patient death if ABO compatibility guidelines are not followed.(4,5) However, ABO incompatible transplants have been performed in kidney transplantation, where dialysis can prolong patient survival in the event of renal failure.(6-10) In contrast, ABO incompatible heart transplants have been the result of errors, and without alternative therapy options, in the event of cardiac failure, have proven lethal.(11)

The immune system of an infant has not yet fully developed, and thus, the antibodies that cause hyperacute rejection are not present in their blood. This ABO blood barrier has been successfully surmounted with heart transplants in infants.(12) More than 100 successful ABO incompatible heart transplants have been performed using the same protocol, and although not all heart transplants using this protocol were successful, unsuccessful cases were unrelated to hyperacute rejection. This protocol expands the donor pool, dramatically decreases the waiting list mortality rate, and minimizes the need for immunosuppression drugs and their side effects, but is limited to infant patients.

Immunologic tolerance, the absence of developing immunity to the donor blood type, has been noted in patients following the ABO incompatible organ transplant protocol.(13) Although not well understood, this tolerance can be induced when foreign antigens are introduced to an immature immune system, and is thought to arise from the same process as self-tolerance.(14-17) The tolerance to the donor ABO blood type develops spontaneously, and persists years after organ transplant.

In developing a tolerogen, a device that results in tolerance in patients, ABO incompatible organ transplants could be performed even after maturation of the immune system. This could result in increasing the donor pool for patients, increasing the efficiency in the use of available organs, reducing the waitlist times, and decreasing the mortality rate of patients. The development of an ABO blood type tolerogen is the ultimate goal of this project.(18)

A porcine model has been used for primary testing, since they express both A and O blood types. Piglets, similar to infants, do not produce antibodies immediately after birth. Although this antibody production may begin at about 12 months in infants, ABO antibody production in piglets begins after about 5 weeks. If implantation of the devices was performed when piglets were 2 or 3 weeks old, the absence of anti-A and anti-B antibodies in piglets beyond 5 weeks old could indicate success of the fabricated tolerogens.

Natural ABO blood type saccharides each exist in 6 different subtypes, which are expressed on different tissues.(19-21) These different subtypes and the different concentration of presented antigens could result in mistyping, and lead to incompatible transfusions and transplants.(22) In the traditional method for determining ABO compatibility, the ABO subtype is not determined, even though serious complications can arise from transfusions and transplants between different subtypes of the same blood type.(23,24) Particularly in emergencies, additional steps to determine blood type may not be performed, resulting in subtype mismatch.(25) This method also gives no indication of the immune

response to individual incompatible subtypes. The incompatibilities toward specific ABO subtypes could be evaluated through assessment of the presence of ABO subtype antibodies.(26)

A more extensive and quantitative evaluation of ABO subtype incompatibility could lead to more informed clinical decisions and additional successful ABO incompatible transplants. Although other ABO antigen subtyping assessments have been developed, no quantitative means to evaluate all ABO antigen subtypes simultaneously have ever previously been available.(27-29) Additionally, since the development of immunologic tolerance is still not well understood, it would be beneficial to develop a method to isolate and study ABO antigen-specific B cells. All of these applications can be addressed by the fabrication of devices presenting synthetic ABO antigens.

The preparation of tolerogens requires the exposure of antigens in the blood stream long term, for which nanoparticles and stents could provide ideal candidates. Nanoparticles could be injected, and stents could be inserted through outpatient surgery into patients with an immature immune system in order to fabricate both circulating and stationary implants. Both of these possibilities must be optimized for ideal performance.

Silica nanoparticles were chosen for tolerogen synthesis for their biocompatibility, resistance to degradation in biological environments and ease of functionalization.(30-38) Silica nanoparticles also offer simple synthetic strategies to incorporate magnetic or fluorescent properties, for efficient capture or detection respectively.(39-43) Additionally, variation in size and functionalization of silica nanoparticles are easily controlled synthetically, both of which can effect performance in biological systems.(32,33,35,36,43-47)

The covalent attachment of antigen is critical for biomolecule stability and sustained presentation while in circulation.(32,36,37,39,48,49) However, protein

adsorption would likely inhibit the intended applications of the nanoparticles and lead to removal from the blood stream.(35,50) Increasing the half-life in blood circulation offers prolonged presentation of antigen, and decreases in the need for additional injections, for which poly(ethylene glycol) (PEG) functionalization has shown promise.(36,45,51-55) PEG can also act to dilute the expensive antigens and to act as a spacer molecule for a biomimetic concentration of antigen to be achieved. Silane functionalization of silica nanoparticles has proven successful for both antigens and PEG, both by direct attachment of silane derivatives of these molecules or by functionalizing first with a linker molecule for further functionalization.(32,36,38,43,46,48,49,56,57)

For the stationary implant, stents constructed from stainless steel were selected for their corrosion resistance, biocompatibility, strength and low cost.(58-61) However, coating of these stents is necessary to prevent the release of harmful ions *in vivo* and to prevent one-electron reduction of proteins onto the surface (which would cause failure of the tolerogen).(62-67) Thin coatings of silica, alumina and titania provide biocompatible, electrically insulating, and flexible platforms for functionalization with silanes, just as silica nanoparticles may be functionalized.(67-75)

With access to the 18 ABO blood antigen subtypes, a superior method for ABO blood type matching can be developed for more effective and accurate determination of compatible and incompatible ABO subtypes.(26) Additionally, a glycan microarray device with the antigen subtypes immobilized in an ordered arrangement could provide a simple test for the attachment of all subtype antibodies simultaneously to assess for rejection in organ transplant patients and to determine if intervention is necessary. Fluorescent antibody detection could then allow for quantitative analysis of ABO antibodies. As an extension of the other aspects of this work, the functionalization of glass slides was performed to create such microarrays. Arrays can be created using a commercial microarray printer and blood serum then assessed for ABO incompatibilities.

Antigen-specific B cells could also be detected using antigen-functionalized microparticles. Fluorescent microparticles designed with PEG to reduce non-specific protein binding were developed for effective identification of the rare cell populations. This identification could allow for the isolation of antigen specific B cells as a means to study the mechanism for the development of tolerance, and its role in ABO incompatible organ transplants.

The objectives of this work involved a collaborative project for the fabrication and application of ABO antigen functionalized stents, nanoparticles and microarray slides. The synthesis of ABO blood type antigens and their functionalization, in cooperation with the Buriak group, was the work of the Lowary group. The Lowary group also characterized the functionalized surfaces using enzyme-linked lectin assays (ELLAs) for monosaccharide model compounds and Fmoc detection to assess amine functionalization of nanoparticles and microparticles. The surface coatings of stents, the preparation of nanoparticles and microparticles and their functionalization is the work described herein, as the work of the Buriak group. The animal implantation and testing, and the isolation of B cells, was the work of the West group. Specifically, the West group performed the porcine model testing, antibody and cell detection, and device incubation allowing for device refinement. The Cramb group performed the imaging, tracking, and toxicological assessment of nanoparticles in an animal model. The characterizing of nanoparticle circulation in chicken embryos was the work of the Cramb group. The interaction of nanoparticles with cell receptors and the fluorescence imaging of an ELLA of functionalized nanoparticles was performed by the Cairo group.

COATING OF STAINLESS STEEL

Solgel dip-coating, electrodeposition, and atomic layer deposition (ALD) were each used in an attempt to coat stainless steel with effective electrically insulating layers of silica. The different coatings were evaluated for the portion that is

ineffectively electrically insulated, or the electroactive area by cyclic voltammetry (CV) and by electrochemical impedance spectroscopy (EIS). The silica films deposited by ALD outperformed those deposited by dip coating or electrodeposition of solgel in CV and EIS evaluation. The film quality was evaluated by scanning electron microscopy (SEM) and atomic force microscopy (AFM) and their thicknesses were evaluated by variable angle spectroscopy ellipsometry. From these measurements, again, the silica ALD films outperformed other films, giving rise to thinner, more conformal coatings. The coatings were also evaluated by FTIR, x-ray photoelectron spectroscopy (XPS), and Auger electron spectroscopy (AES). These results corroborated the utility of the silica ALD film.

Subsequently, additional films of silica and titania deposited by ALD were stressed by three-point bending. The stressing of these films served to evaluate the film performance upon stressing because these films will be used to coat stents that will be expanded in arteries. These films deposited by ALD were reevaluated by CV in order to assess changes in electroactive area as a probe to indicate changes in film quality. Silica ALD thin films also moderately outperformed the titania ALD thin films on stainless steel under the stress conditions used. Additionally, different surface pretreatments prior to depositing ALD metal oxide coatings were performed, and under these same testing conditions of three-point bending and CV evaluation, none appeared to greatly affect the quality of the films. ALD silica coated stainless steel was thus used for subsequent functionalization.

FUNCTIONALIZATION OF SILICA-COATED STAINLESS STEEL

Silica ALD thin films were initially functionalized using monosaccharides (MS) as model compounds prior to evaluation of the expensive trisaccharide and tetrasaccharide (TS) antigens. In addition, the samples were functionalized with poly(ethylene glycol) to prevent nonspecific protein binding. To evaluate mixtures of monosaccharide and PEG silanes, oxidized porous silicon substrates

were used for evaluation by transmission FTIR. The MSs selected were N-acetyl glucosamine (GlcNAc) and galactose (Gal) because they can be effectively detected by commercially available lectins. Successful functionalization of porous silicon was demonstrated by the increase in characteristic peak intensity with corresponding changes in PEG to MS ratios. Subsequently, MS and PEG silane functionalized silica-coated stainless steel were analyzed by XPS and UV-Vis following enzyme-linked lectin assays (ELLAs). By XPS, changes to elemental concentrations of nitrogen, sulfur and oxygen corresponded to changes in solution mixtures of MS and PEG silanes used to functionalize stainless steel samples both uncoated and coated with silica deposited by ALD. Effective biological availability of the MSs and the success of silica coatings in preventing nonspecific protein binding were determined by their successful detection using ELLAs.

Following the results of MS functionalization, TS and PEG silane functionalization of silica-coated stainless steel were analyzed by XPS and UV-Vis following enzyme-linked immunosorbent assays (ELISAs). Similar to the results found for mixtures of MS and PEG silanes, changes to elemental concentrations of nitrogen, sulfur and oxygen as found by XPS corresponded to changes in solution mixtures of TS and PEG silanes. A blood type antigens were determined successfully functionalized by the increase in signal in the UV-Vis spectra compared to the silica-coated stainless steel samples functionalized solely with PEG silane. To evaluate the functionalization under biological conditions, silica-coated stainless steel samples functionalized with TS and PEG silanes were evaluated by ELISA as detected by UV-Vis before and after incubation in blood plasma. The results indicate the biological availability of A blood type antigens both before and after incubation in blood plasma. These blood plasma results also indicate that the synthetic A antigens are recognized by human anti-A antibody from the samples incubated in O blood plasma.

Additionally, silanes were used to functionalize spots on microscope slides in order to develop microarrays. These microscope slides were characterized by

ToF-SIMS and ELISA. ToF-SIMS mapping detected antigen-specific fragments in spots functionalized with antigen and consistently across functionalized films. They were also used to detect antibodies in human blood plasma in order to identify incompatible blood types based on ABO antibodies present in blood-typed donor blood samples.

SYNTHESIS OF SILICA NANOPARTICLES AND MICROPARTICLES

Silica nanoparticles (NPs) and microparticles (MPs) ranging in size from 10-100 nm were successfully prepared by the sol-gel or Stöber synthesis. Particle size was evaluated by SEM and dynamic light scattering (DLS). Unfortunately, the sizing of MPs was ineffective by DLS because of their tendency to fall out of solution. Additionally, the laser wavelength interfered with the characterization of nanoparticles with incorporated fluorophores that fluoresce in the same region. The DLS data was useful, however, in indicating an increase in size, or the aggregation of NPs less than 100 nm in diameter upon centrifugation. This aggregation was confirmed by SEM imaging, although the increase in size determined by the two methods does not match. The surface charge of particles, both unfunctionalized and functionalized with small silane molecules was determined by zeta potential measurements. The zeta potential measurements gave rise to an explanation for the aggregation of unfunctionalized NPs less than 100 nm in diameter. The NPs less than 100 nm are insufficiently charged to repel each other and prevent binding reactions between NPs. Functionalization of these small NPs proved effective in increasing the magnitude of charge on them through zeta potential measurements, which could reduce NP aggregation.

A variety of architectures were developed for nanoparticles depending on their intended purpose. Examples of such architectures include core-shell NPs incorporating fluorophores, exhibiting effective detection, and the incorporation of magnetic NPs, exhibiting effective NP capture. The fluorescence of fabricated particles was evaluated by fluorescence imaging, flow cytometry and two-photon excitation fluorescence correlation spectroscopy (TPE-FCS). Fluorescence

imaging and flow cytometry allowed effective detection of architectures with covalently attached dye. Covalent attachment of dye incorporated into a NP shell was found to demonstrate stronger fluorescence than if the dye was incorporated throughout the core NP. This architecture was used in MPs and the optimal dye concentration was determined by flow cytometry for *in vivo* and *in vitro* applications. Effective detection of small NPs with random dye incorporation was performed by TPE-FCS. Silica shells surrounding dyes incorporated all of the aforementioned silica particle architectures have proven effective in reducing photobleaching and leaching of dye. Magnetic iron oxide nanoparticles were characterized by transmission electron microscopy and through magnetic testing.

FUNCTIONALIZATION OF SILICA NANOPARTICLES AND MICROPARTICLES

Different functionalization methods for NPs and MPs were assessed. Again, MSs were used for initial studies rather than the more expensive TSs. Three different functionalization methods were developed. First, silane functionalization was developed, in which mixtures of MS and PEG silanes were used to functionalize silica particles and were detected successfully using fluorescent lectins specific for the MSs. In the second method, mercaptopropyltrimethoxysilane was used to synthesize thiol-terminated nanoparticles. Mixtures of simple PEG and thiol silanes were used to functionalize NPs and oxygen and sulfur content determined by XPS corresponded to the silane ratios used. The thiol-terminated nanoparticles were subsequently functionalized using photoinitiation of an alkene derivative of MS. The third functionalization method involved amine termination of the silica surfaces using aminopropyltrimethoxysilane (APTMS). Using a semi-quantitative fluorenylmethyloxycarbonyl assay and UV-Vis for detection, the amine functionalization using APTMS was optimized and a PEG linker molecule was used to covalently bind to the amine-terminated MPs for subsequent functionalization of MS using a PnP derivative.

All three methods were each successful, as determined by ELLA and flow cytometry. However, the amine-PnP functionalization resulted in more efficient use and minimal loss of saccharides, an important result for functionalization of expensive TSs. Functionalization of the amine-terminated microparticles with PnP derivatives of TS was effectively characterized using flow cytometry for dual detection. This dual detection involved detection of both incorporated fluorophore and fluorophores for ELISA at different wavelengths of ABO antigen-functionalized fluorescent microparticles. These TS-functionalized MPs were also found useful in detecting human blood-type antibodies. PEG functionalization of microparticles was also successfully detected using PEG antibodies with flow cytometry.

FUTURE WORK

The results obtained from the silica ALD coated stainless steel indicate their use in preventing nonspecific protein binding. The testing of the silica ALD coated stainless steel stents for their ability to prevent nonspecific protein binding *in vivo* upon expansion has not yet been completed. Additionally, the testing of PEG-functionalized silica ALD coated stainless steel stents could prove useful *in vivo*. Both of these studies could provide results for useful stents for clinical use. The testing of the A blood type antigen and PEG functionalized silica ALD coated stainless steel stents in porcine model for tolerance induction must also still be completed. This testing must also include the optimization of the A antigen to PEG ratio to reduce nonspecific protein binding for prolonged lifetime of the tolerogen. Subsequent tolerogen testing could then be expanded to include stents functionalized with any variety of ABO blood type antigens.

Further *in ovo* and toxicity testing of functionalized NPs must still be completed to further optimize architecture and functionalization. More information about the toxicity of these particles must also be obtained before their use *in vivo*. The use of an animal model to characterize the circulation time, dosing parameters, and determine the injection schedule could provide useful data for *in vivo* applications

of the tolerogens. The use of NPs as tolerogens must also be determined, for which a porcine model could be used. The utility of the ABO blood type antigen-functionalized MPs for identification and isolation of antigen-specific B cells must be tested as well. By using two different sets of MPs, with a different incorporated dye in each, functionalized with the same antigen, dual staining of the antigen specific B cells may be possible and increase the recognition sensitivity. The use of these MPs to test for ABO blood type antibodies may also be tested. As well, the use of ABO-subtype functionalized microarray slides could be used to identify all ABO subtype antibody, and the clinical use of the microarray must be studied.

In the future, the tolerogens developed through this project could allow for a standard protocol to be established for infant tolerance induction. The tolerogen can be inserted through minimally invasive procedures, and need only be present in the infant's immune system for two years. Self-tolerance develops by this age in humans, and thus it would mean that the tolerogen presence would be unnecessary beyond this age. This tolerance induction protocol could be applied primarily for patients with identified ailments that would require organ transplant in the future. This could also be applied as a regularly scheduled protocol, similar to the immunization schedule for infants, to open the opportunity for ABO incompatible transplants if ever the need arose. This would make the transfer of tissues, such as blood transfusions, much simpler in the event of an emergency situation.

REFERENCES

1. Cartron, J.; Colin, Y., *Transfus. Clin. Biol.* **2001**, *8* (3), 163-199.
2. Mollicone, R.; Candelier, J.-J.; Mennesson, B.; Coullin, P.; Venot, A.; Oriol, R., *Carbohydr. Res.* **1992**, *228* (1), 265-276.
3. Oriol, R.; Mollicone, R.; Coullin, P.; Dalix, A.; Candelier, J., *APMIS Suppl.* **1992**, *27* (2), 28-38.

4. Starzl, T.; Ishikawa, M.; Putnam, C.; Porter, K.; Picache, R.; Husberg, B.; Halgrimson, C.; Schroter, G., *Transplant. Proc.* **1974**, *6* (4), 129-139.
5. Stock, P.; Sutherland, D.; Fryd, D.; Ascher, N.; Payne, W.; Simmons, R.; Najarian, J., *Transplant. Proc.* **1987**, *19* (1), 711-712.
6. Slapak, M.; Naik, R.; Lee, H., *Transplantation* **1981**, *31* (1), 4-7.
7. Bennett, A.; Bensinger, W.; Raja, R.; Baquero, A.; McAlack, R., *Transplantation* **1987**, *43* (6), 909-911.
8. Alexandre, G.; Squifflet, J.; Bruyere, M. D.; Latinne, D.; Reding, R.; Gianello, P.; Carlier, M.; Pirson, Y., *Transplant. Proc.* **1987**, *19* (6), 4538-4542.
9. Takahashi, K.; Yagisawa, T.; Sonda, K.; Kawaguchi, H.; Yamaguchi, Y.; Toma, H.; Agishi, T.; Ota, K., *Transplant. Proc.* **1993**, *25* (1), 271-273.
10. Gugenheim, J.; Samuel, D.; Bismuth, H.; Reynes, M., *Lancet* **1990**, *336* (8714), 519-523.
11. Cooper, D., *J. Heart Lung Transpl.* **1990**, *9*, 376-381.
12. West, L.; Pollock-Barziv, S.; Dipchand, A.; Lee, K.; Cardella, C.; Benson, L.; Rebeyka, I.; Coles, J., *New Engl. J. Med.* **2001**, *344* (11), 793-800.
13. Fan, X.; Ang, A.; Pollock-BarZiv, S.; Dipchand, A.; Ruiz, P.; Wilson, G.; Platt, J.; West, L., *Nat. Mater.* **2004**, *10* (11), 1227-1233.
14. Billingham, R.; Brent, L.; Medawar, P., *Nature* **1953**, *172* (4379), 603-606.
15. Owen, R., *Science* **1945**, *102* (2651), 400-401.
16. Streilein, J.; Klein, J., *J. Immunol.* **1977**, *119* (6), 2147-2150.
17. McCarthy, S.; Bach, F., *J. Immunol.* **1983**, *131* (4), 1676-1682.
18. West, L.; Lowary, T.; Buriak, J.; Daly, B.; Mylvaganam, J.; Meloncelli, P.; Wright, V.; Cooper, A. Methods and Systems for Inducing Immunologic Tolerance to Non-Self Antigens. PCT Patent (PCT/CA2009/001814), December, 2009.
19. Ravn, V.; Dabelsteen, E., *APMIS* **2000**, *108* (1), 1-28.
20. Oriol, R., *Transplant. Proc.* **1987**, *19* (6), 4416-4420.
21. Yamamoto, F., *Immunohematology* **2004**, *20* (1), 3-22.
22. Sapanara, N.; Swami, V.; Besa, E., *LabMedicine* **2004**, *35* (9), 538-541.

23. Contreras, M.; Hazlehurst, G.; Armitage, S., *Br. J. Haematol.* **1983**, *55* (4), 657-663.
24. Gorodzinsky, F.; Stechison, M.; Poon, A.; Arbus, G., *Can. Med. Assoc. J.* **1981**, *125* (8), 871-873.
25. Chaudhari, C.; Misra, R.; Nagpal, A., *MJAFI* **2008**, *64* (4), 371-372.
26. Lowary, T.; Cairo, C.; West, L.; Buriak, J.; Jeyakanthan, M.; Slaney, A.; Meloncelli, P. Method and system for ABO compatible blood type matching. US61529082, 2011.
27. Bochner, B.; Alvarez, R.; Mehta, P.; Bovin, N.; Blixt, O.; White, J.; Schnaar, R., *J. Biol. Chem.* **2005**, *280* (6), 4307-4312.
28. Blixt, O.; Head, S.; Mondala, T.; Scanlan, C.; Huflejt, M.; Alvarez, R.; Bryan, M.; Fazio, F.; Calarese, D.; Stevens, J.; Razi, N.; Stevens, D.; Skehel, J.; Die, I. v.; Burton, D.; Wilson, I.; Cummings, R.; Bovin, N.; Wong, C.-H.; Paulson, J., *PNAS* **2004**, *101* (49), 17033-17038.
29. Holgersson, J.; Liu, J.; Lindberg, L.; Grufman, P. Blood group antigens of different types for diagnostic and therapeutic applications 7897328, 2011.
30. Kumar, R.; Roy, I.; Ohulchanskyy, T.; Vathy, L.; Bergey, E.; Sajjad, M.; Prasad, P., *ACS Nano* **2010**, *4* (2), 699-708.
31. Ha, S.-W.; Camalier, C.; Jr., G. B.; Lee, J.-K., *Chem. Commun.* **2009**, (20), 2881-2883.
32. Burns, A.; Ow, H.; Wiesner, U., *Chem. Soc. Rev.* **2006**, *35* (11), 1028-1042.
33. Ma, D.; Guan, J.; Normandin, F.; Denomme, S.; Enright, G.; Veres, T.; Simard, B., *Chem. Mater.* **2006**, *18* (7), 1920-1927.
34. Insin, N.; Tracy, J.; Lee, H.; Zimmer, J.; Westervelt, R.; Bawendi, M., *ACS Nano* **2008**, *2* (2), 197-202.
35. Burns, A.; Vider, J.; Ow, H.; Herz, E.; Penate-Medina, O.; Baumgart, M.; Larson, S.; Wiesner, U.; Bradbury, M., *Nano Lett.* **2009**, *9* (1), 442-448.
36. He, X.; Nie, H.; Wang, K.; Tan, W.; Wu, X.; Zhang, P., *Anal. Chem.* **2008**, *80* (24), 9597-9603.
37. Wang, Y.; Liu, B., *Langmuir* **2009**, *25* (21), 12787-12793.

38. He, R.; You, X.; Shao, J.; Gao, F.; Pan, B.; Cui, D., *Nanotechnology* **2007**, *18* (31), 315601-315607.
39. Liu, S.; Zhang, H.-L.; Liu, T.-C.; Liu, B.; Cao, Y.-C.; Huang, Z.-L.; Zhao, Y.-D., *J. Biomed. Mater. Res. A* **2007**, *80* (3), 752-757.
40. Corsi, F.; Palma, C. D.; Colombo, M.; Allevi, R.; Nebuloni, M.; Ronchi, S.; Rizzi, G.; Tosoni, A.; Trabucchi, E.; Clementi, E.; Prosperi, D., *Small* **2009**, *5* (22), 2555-2564.
41. Lu, C.-W.; Hung, Y.; Hsiao, J.-K.; Yao, M.; Chung, T.-H.; Lin, Y.-S.; Wu, S.-H.; Hsu, S.-C.; Liu, H.-M.; Mou, C.-Y.; Yang, C.-S.; Huang, D.-M.; Chen, Y.-C., *Nano Lett.* **2007**, *7* (1), 149-154.
42. Gupta, R.; Kumar, A., *Biomed. Mater.* **2008**, *3* (3), 034005.
43. Tan, W.; Wang, K.; He, X.; Zhao, X.; Drake, T.; Wang, L.; Bagwe, R., *Med. Res. Rev.* **2004**, *24* (5), 621-638.
44. Warheit, D.; Webb, T.; Colvin, V.; Reed, K.; Sayes, C., *Toxicol. Sci.* **2007**, *95* (1), 270-280.
45. Nel, A.; Madler, L.; Velegol, D.; Xia, T.; Hoek, E.; Somasundaran, P.; Klaessig, F.; Castranova, V.; Thompson, M., *Nat. Mater.* **2009**, *8* (7), 543-557.
46. Jana, N.; Earhart, C.; Ying, J., *Chem. Mater.* **2007**, *19* (21), 5074-5082.
47. Ow, H.; Larson, D.; Srivastava, M.; Baird, B.; Webb, W.; Wiesner, U., *Nano Lett.* **2005**, *5* (1), 113-117.
48. Nakamura, M.; Shono, M.; Ishimura, K., *Anal. Chem.* **2007**, *79* (17), 6507-6514.
49. Gann, J.; Yan, M., *Langmuir* **2008**, *24* (10), 5319-5323.
50. Dobrokvolskaia, M.; McNeil, S., *Nat. Nanotechnol.* **2007**, *2* (8), 469-478.
51. Zillies, J.; Zwioerek, K.; Winter, G.; Coester, C., *Anal. Chem.* **2007**, *79* (12), 4574-4580.
52. Gref, R.; Luck, M.; Quellec, P.; Marchand, M.; Dellacherie, E.; Harnisch, S.; Blunk, T.; Muller, R., *Colloids Surf., B* **2000**, *18* (3-4), 301-313.
53. Lin, Y.-S.; Haynes, C., *Chem. Mater.* **2009**, *21* (17), 3979-3986.
54. Shi, M.; Lu, J.; Shoichet, M., *J. Mater. Chem.* **2009**, *19* (31), 5485-5498.
55. Mohanraj, V.; Chen, Y., *Trop. J. Pharm. Res.* **2006**, *5* (1), 561-573.

56. Kim, Y.-J.; Ha, S.-W.; Jeon, S.-M.; Yoo, D.; Chun, S.-H.; Sohn, B.-H.; Lee, J.-K., *Langmuir* **2010**, *26* (10), 7555-7560.
57. Banet, P.; Marcotte, N.; Lerner, D.; Brunel, D., *Langmuir* **2008**, *24* (16), 9030-9037.
58. Lim, I., *MURJ* **2004**, *11*, 33.
59. Shahryari, A.; Azari, F.; Vali, H.; Omanovic, S., *Acta Biomater.* **2010**, *6* (2), 695-701.
60. Raman, A.; Gawalt, E. S., *Mater. Sci. Eng., C* **2010**, *30* (8), 1157-1161.
61. Lo, K. H.; Shek, C. H.; Lai, J. K. L., *Mater. Sci. Eng., R* **2009**, *65* (4-6), 39-104.
62. Ekqvist, S.; Svedman, C.; Moeller, H.; Kehler, M.; Pripp, C. M.; Bjoerk, J.; Gruvberger, B.; Holmstroem, E.; Gustavsson, C. G.; Bruze, M., *Br. J. Dermatol.* **2007**, *157* (4), 730-738.
63. Touzin, M.; Chevallier, P.; Lewis, F.; Turgeon, S.; Holvoet, S.; Laroche, G.; Mantovani, D., *Surf. Coat. Technol.* **2008**, *202* (19), 4884-4891.
64. Bayram, C.; Mizrak, A. K.; Akturk, S.; Kursaklioglu, H.; Iyisoy, A.; Ifran, A.; Denkbaz, E. B., *Biomed. Mater.* **2010**, *5* (5), 055007/1-055007/8.
65. Liu, C. L.; Chu, P. K.; Lin, G. Q.; Qi, M., *Surf. Coat. Technol.* **2006**, *201* (6), 2802-2806.
66. Gallino, E.; Massey, S.; Tatoulian, M.; Mantovani, D., *Surf. Coat. Technol.* **2010**, *205* (7), 2461-2468.
67. Mikhalevska, L.; Chorna, N.; Lazarenko, O.; Haworth, P.; Sudre, A.; Mikhalevsky, S., *J. Biomed. Mater. Res. B* **2011**, *96B* (2), 333-341.
68. Wang, D.; Bierwagen, G., *Prog. Org. Coat.* **2009**, *64* (4), 327-338.
69. Gurappa, I., *Surf. Coat. Technol.* **2002**, *161* (1), 70-78.
70. Monsma, D.; Becker, J., *ECS Trans.* **2007**, *11* (7), 39-44.
71. Matero, R.; Ritala, M.; Leskela, M.; Salo, T.; Aromaa, J.; Forsen, O., *J. Phys. IV* **1999**, *09* (PR8), 493-499.
72. Meth, S.; Sukenik, C. N., *Thin Solid Films* **2003**, *425* (1-2), 49-58.
73. Hatano, K.; Yamazaki, T.; Yoshino, K.; Ohyama, N.; Koyama, T.; Matsuoka, K.; Terunuma, D., *Tetrahedron Lett.* **2008**, *49* (39), 5593-5596.

74. Maat, J.; Regeling, R.; Yang, M.; Mullings, M.; Bent, S.; Zuilhof, H., *Langmuir* **2009**, 25 (19), 11592-11597.
75. Anderson, A.; Ashurst, W., *Langmuir* **2009**, 25 (19), 11541-11548.